On the Design and Analysis of Micro-metric Resolution Arrays in Integrated Technology for Near-Field Dielectric Spectroscopy

Thippur Shivamurthy, Harshita

DOI
10.4233/uuid:cebc3c19-40b1-4b6d-8acd-e30cbd6f0fda

Publication date
2020

Document Version
Final published version

Citation (APA)
Thippur Shivamurthy, H. (2020). *On the Design and Analysis of Micro-metric Resolution Arrays in Integrated Technology for Near-Field Dielectric Spectroscopy*. [Dissertation (TU Delft), Delft University of Technology]. https://doi.org/10.4233/uuid:cebc3c19-40b1-4b6d-8acd-e30cbd6f0fda

Important note
To cite this publication, please use the final published version (if applicable).
Please check the document version above.

On the Design and Analysis of Micro-metric Resolution Arrays in Integrated Technology for Near-Field Dielectric Spectroscopy

DISSERTATION

for the purpose of obtaining the degree of doctor
at Delft University of Technology
by the authority of the Rector Magnificus, Prof. dr. ir. T.H.J.J van der Hagen,
chair of the board for Doctorates,
to be defended publicly on 20th February 2020 at 15:00 o'clock.

by

Harshitha THIPPUR SHIVAMURTHY

Master of Science in Electrical Engineering,
Delft University of Technology, The Netherlands,
born in Bangalore, India.

This dissertation has been approved by the promotors.
Composition of the doctoral committee:

Rector Magnificus	Chairman
Prof. dr. ir. A. Neto,	Delft University of Technology, promotor
Dr. ir. M. Spirito,	Delft University of Technology, promotor

Independent members:

Prof. dr. A. Freni,	University of Florence, Italy
Prof. dr. G. Vandenbosch,	Université catholique de Louvain, Belgium
Prof. dr. Z. Taylor,	Aalto University, Finland
Dr. W. H. Syed,	NXP Semiconductors, Netherlands
Prof. dr. ir. N. Llombart,	Delft University of Technology, Netherlands

Reserve member:

Prof. dr. ir. L.C.N. de Vreede,	Delft University of Technology, Netherlands

The work presented in this thesis has been performed at TU Delft and financed by the Dutch Technology Foundation STW, which is part of the Netherlands Organisation for Scientific Research (NWO).

Keywords: Capacitive Sensors, Coaxial Probes, Sensitivity, Pin-Patch elements, Method of Moments, Greens function, CMOS Technology.

Printed by: Ipskamp Printing, Enschede, Netherlands.

Cover design: Harshitha Thippur Shivamurthy.

An electronic version of this dissertation is available at: http://repository.tudelft.nl/

ISBN 978-94-6384-114-6

Contents

Chapter 1

Introduction

Dielectric spectroscopy is a technique that can be employed for the measurement of material/sample composition in various applications. The detection principle is based on the interaction of the electromagnetic fields with the dipole moments of the sample under study. Any inhomogeneous artifact caused by an impurity or a contaminant in the sample will cause a change in field distribution that can be sensed. Most detection techniques rely on the measurement of the reflection coefficient, Γ offered by the radiating probe, which represents the ratio of the propagating and the reflected-voltage wave. Since voltage can be related to the integral of an E-field, knowledge of this reflection coefficient, combined with information on the probe enables the derivation of the sample's dielectric properties [1].
In (bio)-medical applications these measurements can reveal the changes in the composition of a sample/tissue [2]. Since tumors in humans or cell disorders in agricultural products are known to have different dielectric properties, in principle these defects can be detected by dielectric spectroscopy methods [3, 4]. In comparison, conventional (bio)-medical techniques for detecting tumor cells rely on ultrasound, X-rays, magnetic resonance imaging (MRI), computed tomography (CT) and positron emission tomography(PET). These techniques sense the presence of cancer cells through a variation in density between neighboring skin/fat tissue; this provides low contrast when looking at tumors in dense tissues or skin samples [5]. Moreover, X-ray detection exposes healthy tissue to the harmful effects of ionizing radiation. Table. 1.1 presents the comparison between the various traditional medical imaging techniques that are popular but not competitive in skin cancer detection and quantification, [6, 7], based on their frequency of operation, detection capabilities, spatial resolution, cost, harmful effects etc. Using electromagnetic waves at microwave frequencies for medical diagnosis is emerging as a very efficient low-cost and less harmful alternative to the above outlined techniques.

Imaging Technique	**Ultrasound**	**CT**	**MRI**	**PET**
EM Spectrum	High frequency sound	X-rays	Radio waves	High-energy γ rays
Detection capability	Organ-Tissue	Organ-Tissue	Organ-Tissue	Tissue-Cellular-Molecular
Spatial Resolution	50≈ 500 μm	50≈200 μm	25≈100 μm	1≈2 mm
Advantages	Low cost and Real-time	High spatial resolution	Highest spatial resolution	High sensitivity and penetration depth
Disadvantages	Limited spatial resolution	Radiation	Cost and post-processing time	Expensive and radiation

Table 1.1: Traditional Medical Imaging Techniques.

1.1 The Need for Dielectric Spectroscopy

Dielectric spectroscopy can provide an in-depth knowledge on the biological composition of the superficial and sub-interface layer(s) of a sample. This data can provide key information in making crucial decisions for various applications ranging from medical diagnosis to quality control as outlined below.

- **Medical inspection:** In skin cancer sizing and in-vivo tumor assessment [8]. Currently, there is a lack of widespread real-time intraoperative imaging tools for skin tumor resection. Photonic technologies have shown significant promise by their clinical efficacy is uncertain. There are many widefield, photonic imaging technologies under research and some of them have progressed to the clinical trial phase. The most popular application is intraoperative imaging during Mohs micrograph surgery (MMS); the most commonly used surgical technique for skin cancer resection. Some technologies for MMS assistance include (1) fluorescence imaging [9–14], (2) confocal microscopy [15–18] and (3) Optical Coherence Tomography (OCT) [19–22]. Fluorescence imaging leverages the unique biomolecular signature of protein vs normal. OCT and confocal microscopy utilize specific morphological features. Tumor cells and their constituents demonstrate distinctly different shapes then normal cells and this can be visualized with illumination wavelengths proportional to cellular size (e.g. UV/VIS/NIR). It's difficult to compare/contrast with Biophotonics in the context of MMS as cell morphology and molecular signatures are contrast mechanisms not

directly accessed when quantifying changes in macroscopic microwave permittivity. That being said, photonic systems have very limited penetration (e.g. 100's of microns) due to significant scattering. However, dielectric spectroscopy has a great opportunity in, for example intraoperative planning. Skin cancers extend many millimeters beyond the visible surface border and the full extend cannot be mapped with photonic techniques. High spatial resolution permittivity measurement with the ability to account for a "top skin layer" may give surgeons a good idea about how broad the tumor extends literally. This information would be very valuable. Also, the penetration depth puts you close enough to the surface to avoid competition with Ultrasound/MRI/CT.

- **Food and flower quality inspection:** In prediction of storage disorders (core browning, skin spots) in fruits and optimization of floral induction [23, 24]. Today's food and flower quality-inspection tools are based on molecular diagnostics [25], or low tech physiological measurements and visual inspection. A high resolution dielectric sensor will provide a complementary technology using the non-invasive near-field inspection of biological samples to reveal their dielectric fingerprint. This additional/alternative source of information (e.g., based on the water content and cellular level degradation mechanism [26]) can significantly reduce errors in critical and economically important decision processes such as fresh produce storage and flower induction in ornamental crops. Minimizing food spoilage during storing and, early and correct identification of the transition to flowering, represent a considerable economic value due to the large volumes associated with agriculture and flower products.

- **Evaluation of drug penetration** through the skin, allowing to evaluate the hydration of the outer skin (stratum corneum), which is an important parameter when studying new drugs and their ability to be absorbed by the body [27, 28].

- **Non-destructive testing:** High spatial resolution in combination with a view up to a depth of a few millimeters provide new non-destructive testing/ inspection tools (e.g., in support surface analysis and paint / laminate inspection) [29].

- **Quality control for pharmaceuticals** (e.g., detecting contaminants and water content). Quality assurance monitoring is of great importance in the pharmaceutical industry. If contamination or water exposure occurs, the desired quality and bioavailability of the drug can be compromised [30, 31], also the effective expiry date of food products can be effectively determined.

1.2 Microwave-Based Spectroscopy: Limitations

Despite its basic capability to provide information regarding the physiological changes in a medium without employing ionizing radiation, dielectric spectroscopy has up to date only resulted in lab-level demonstrators. This can be attributed to the limitations outlined below in the two regimes of operation (i.e. far-field and near-field).

- **Far-field based dielectric spectroscopy**: [5] typically targets breast cancer detection like applications. Systems using these (radar like) concepts are typically limited by the Abbe diffraction limit [32] and require large antenna apertures to achieve high lateral resolution. Using higher frequencies (e.g., larger than 10 GHz) to enhance the lateral resolution for a given antenna aperture, is blocked by the very high attenuation of tissue for these frequencies, making (high-quality) signal detection impossible. Moreover, the depth resolution in this approach depends directly on the signal bandwidth, requiring wideband operation and high power levels to account for the signal attenuation from the skin/fat tissue, yielding again severe restrictions in practical situations. Furthermore, wideband solutions require complex techniques for compensating the dispersion effects of the frequency dependent permittivity of biological samples [33–35].

- **Near-field techniques**: are mostly focused on surface and sub-surface inspection. These techniques have been demonstrated to provide a resolution in the order of a 1000th of the wavelength (λ) at a few GHz [36, 37]. Nevertheless, the related sub-wavelength radiator (e.g., smaller than $\lambda/100$) provides a very high impedance mismatch. In current system implementations this mismatch is tuned out using a narrowband high-Q resonator, providing information only at a specific frequency. Moreover these systems implementations can measure only one spot at the time, i.e., they use a single antenna and make use of mechanical motors to scan the surface of the sample. For the radiating element typically non-planar probes (i.e., open-ended waveguides and open-ended coaxial lines [1]) are used. The resulting setups are bulky, expensive, slow, require a smooth pre-treated surface of the (bio)sample and are difficult to operate, making them suitable only for static laboratory (in-vitro) experiments.

All near- and far-field systems concepts proposed so far make use of commercial equipment for the signal generation and detection (i.e., network analyzers). These network analyzer based systems provide the highest sensitivity and dynamic range when measuring reflection coefficients in the order of their system impedance (i.e., 50 Ω). When measuring biological

samples, however, the feed impedance of the antenna/radiator loaded by the sample will be significantly different than 50 Ω, resulting in reflection coefficients close to one, which can only be measured with limited accuracy by the instrument.

1.3 Proposed Solution

To push dielectric spectroscopy techniques to useful real-life applications, in this project we propose the development of integrated high-resolution microwave spectroscopy system. These highly-integrated sensor systems will be optimized for real-time measurement and visualization of the dielectric constant fluctuations in organic tissues.

- **Near-field radiator/sensor matrix:** To enable capturing real-time high-resolution electromagnetic images, a novel near-field sensor matrix will be designed and implemented in advanced sub-micron CMOS (complementary metal-oxide semiconductor) technology. The extensive back-end of this technology and excellent active device performance will be employed to realize, compact high-frequency wideband (0.5 GHz to 3 GHz) radiators. Moreover, techniques will be developed to extract the complex permittivity of multi-layered material under test (MUT) from the Γ measurements. The information gained using this approach is very valuable in several applications e.g., when examining the water content of (bio)-samples or (small) airgaps in paint or laminate layers. Techniques based on evanescent waves (also known as near-field techniques) have been successfully exploited to provide high-resolution characterization of different materials in literature [36, 38, 39].

- **Detection bridges with reference impedance adjustment:** The signal generation and detection (i.e., the functionality of a vector network analyzer) needs to be implemented for each radiator on the integrated circuit (IC). By using the latest progress in silicon IC technology, very small but accurate detection bridges can be developed, which can be placed directly underneath the radiating elements. Such an approach will enable a fast readout directly in the digital domain. The addition of a calibration feature will allow us to measure also the absolute dielectric properties of the sample and not only the dielectric variations in dielectric constant, information that is relevant to many applications.

- **Real-time read-out and visualization:** Dedicated software for the control, calibration and data readout of the near-field matrix sensor, will be developed. Visual-

ization of this data will be supported for real-time operation and customized to the needs of the aimed end-users.

1.4 Research Objective

The goal of this thesis is to develop a lab-level system and an integrated solution with enhanced spatial resolution to evaluate the electrical properties (i.e., complex permittivity) of a sample by employing evanescent (i.e., exponentially decaying) electro-magnetic (EM) waves.

- **Lab-level System:** Electromagnetic imaging rely on the contrast in the permittivity between the host medium and the abberations introduced in the same due to a an abnormality or a defect. Knowledge about the relevant dielectric properties of the sample of interest is essential in the design and optimization of a imaging system. Thus it is essential to collect reference dielectric properties of various biological materials using low-cost and low-maintenance system. The most commonly used sensing element for non-invasive sensing applications in the microwave regime is an open-ended coaxial probe. A coaxial probe is widely used due to its broadband measurement capabilities and simple calibration procedure. Several inversion schemes, to translate the measured reflection coefficient to complex permittivity have been reported in literature [40–49]. However most of the techniques are based on the assumption that the MUT is either homogeneous or a two-layered. In this thesis a full wave model of the coaxial probe radiating in the presence of a stratified MUT will be derived and an equivalent circuit for the same will be deduced. Furthermore the model will then be used in characterizing bio-samples to collect reference data.

- **Integrated sensor matrix:** A new approach, based on the use of advanced integrated circuit (IC) technology is envisioned to yield a novel "near-field matrix sensor". Such a device, composed out of a large number of sub-wavelength radiators (i.e., D$< \lambda/100$) with typical radiator dimensions in the order of 100x100 μm2 (or even less) combined with dedicated high-sensitivity broadband detection circuitry, would be able to provide a wealth of new functionalities and therefore acts as enabler for many new applications. This novel integrated sensor would not require mechanical movement, so it can be used at any place, facilitating real-time high-resolution images of the complex dielectric constant fluctuations in any object/sample contacting the surface of the near-field array sensor. The above are features that are

of great importance to many applications in the medical (e.g., in-vivo tumor "cell" detection during surgery), bio-medical (e.g., characterization of dielectric properties of biological tissues) [4] and the food industry (e.g., screening methods to optimize storage planning [23]). To address the specific needs of these applications, in terms of: resolution and sensitivity, the following research ideas will be pursued:

- **Resolution:** In this project sub-wavelength radiators will be implemented with sub-micrometric precision using high-end IC technologies, providing high resolution. Note that the resolution limitation in near-field imaging is not dictated by the operating frequency (in contrast to far-field systems such as radar), but by the feature size of the radiating elements.
- **Sensitivity:** The evanescent wave radiators/detectors matrix will be combined with high-sensitivity detection circuitry placed on the same IC. The very-short distances between the antenna element and the detecting circuitry will allow compensation of the large impedance fluctuations of the radiators, due to the loading with different (bio-)samples, directly by the detection circuitry itself.

1.5 Scientific Contribution in this Thesis

This thesis deals with the theoretical analysis and the design of coaxial/coaxial based dielectric sensors. The analysis of such structures is based on a spectral Green's function method, which not only gives an insight into the physics of the sensor, but also leads to analytical expressions to design the sensors. The formalism is then exploited to extract complex permittivity of the unknown MUT. The key novel aspects addressed in this thesis are summarized as follows:

- *Analysis of open-ended coaxial apertures*: the extraction of the high spectral components of the admittance spectrum results in expressing the input admittance as a sum of two contributions. This spectral separation allows to evaluate the dependency of the sensors sensitivity to the dielectric perturbation in a given layer in a multi-layered MUT based on the sensors and MUT's dimensions.
- *Sensitivity analysis:* the read-out circuitry implemented in an integrated solution is most often a wheatstone bridge which offers a quantification of impedance variation relative to a baseline value. The sensitivity of the sensor to the variations in the permittivity of a given layer in a multilayered stack depends firstly on the sensors dimensions and secondly on the layers thicknesses.

- *Analysis of single-ended coax fed permittivity sensor*: the detection depth of a coaxial sensor can be further enhanced, while still resorting to planar technology, by loading the coaxial by a patch, which in terms of electric currents can be viewed as a larger coax. The input admittance evaluated using the integral equations is used in generating calibration planes for complex permittivity extraction using the sensor.

- *Derivation of Equivalent circuit of a patch loaded coax based sensor:* a rigorous equivalent circuit is derived and can be used in evaluating the input admittance of the patch loaded coaxial sensor. The exploitation of the equivalent circuit and the spectral Green's function allows to evaluate the permittivity of the MUT.

1.6 Outline of the Thesis

The thesis is organized in seven chapters, which address several aspects of the analysis, design and experimental validation of dielectric sensors. A brief summary about the contents of each chapter is as following:

- In **Chapter 2**[1], a magnetic field integral equation (MFIE) is imposed across the coaxial aperture etched on the ground plane to study the radiation behavior of the element. Input admittance of a coaxial aperture is derived resorting to Galerkin's method of moments to solve the integral equation. A methodology to accelerate the evaluation of the reaction integral is outlined by extracting the high spectral components of the integral associated to the quasi-static capacitance.

- In **Chapter 3** the numerical model derived for the coaxial probe in the Ch. 2 is used to extract the complex permittivity of the pulp of a mango by modelling it as a two layered stratified medium, assuming the second layer is infinitely extending. The model is further used to study the ripening process of mangoes, by mapping the variation in the pulp permittivity over a duration of time. Moreover the model is also used to identify internal defects (non-visible) in mangoes.

- In **Chapter 4**[2] the sensitivity analysis of the coaxial/ coaxial based sensors to the alterations in the permittivity of a multilayered MUT is studied. The qualitative parameter Sensitivity S which is the difference in the signal in the presence and the

[1]This chapter is an extended version of the article [J1] (a list of the author's publications is included at the end of this dissertation, p. 97)

[2]The content of this chapter is published in [J1] (see p. 97)

absence of an anamoly in the host medium is derived assuming the read-out circuitry to be an impedance balancing bridge. Building on the insight acquired from the sensitivity analysis, guidelines for increasing the detection depth of the sensor are derived. This was further validated with sensitivity measurements.

- **Chapter 5** extends the model developed in Ch. 2 for a coaxial to a patch loaded coaxial geometry, by including an additional magnetic field contribution associated to the equivalent electric currents distributed on the surface of the pin and the patch. From the derived tool, calibration surfaces that map the measured input admittance to complex permittivity are derived for different patch radii. The calibration surfaces are subsequently used in extracting the permittivity of an unknown liquid (ethanol).

- **Chapter 6** outlines the procedure to evaluate the reaction integrals involving vertical and transverse currents in stratified media. For a specific case of a patch loaded coaxial geometry, the basis functions are discussed in-detail.

- In **Chapter 7**[3] an equivalent radial transmission line model is derived to accurately evaluate the input impedance of a single-ended patch sensing element realized in planar technology. A transformer is included in the transmission line model to account for the reactive energy associated to the transition from pin to patch. The end-point load of the line associated to the material under test and the patch metallization thickness is evaluated resorting to an in-house tool based on method of moments procedure. The tool provides an accurate estimate of the current distributions and voltages over the entire structure with accuracies equivalent to full wave commercial tool.

- **Chapter 8** provides concluding remarks about the results achieved in the project and possible indications about the future research directions.

[3]The content of this chapter is published in [J2] (see p. 97)

Chapter 2

Open-ended Coaxial Probe

The most commonly used sensing element for non-destructive sensing applications in the microwave regime is an open-ended coaxial sensing element due to its broadband measurement capabilities and simple calibration procedure. Several inversion procedures for translating the measured reflection coefficient to complex permittivity have been proposed in literature [40–49]. These techniques are based on estimating the permittivity using either static [40–43], quasi-static [44, 45] or full-wave [46–49] based models of the coaxial aperture and the Material Under Test (MUT).

In the static and the quasi-static approach the MUT, either homogeneous or two layered medium, is assumed to be purely reactive and is modelled as a reactive load in parallel with the fringe capacitance associated to the coaxial aperture. They have a direct linear inverse procedure that is computationally inexpensive and fast. Despite the aforementioned advantages the static and quasi-static based models do not aid in probe design and optimization to achieve the required sensitivity and detection depth performances. Additionally they are valid at very low microwave frequencies only. Full wave/spectral-domain based model account for the reactive and the conductive part of the MUT by including the higher order modes. This model is accurate to wider frequency range and is well suited for probe design and optimization. Regardless of being accurate this procedure has no direct inverse method and is computationally expensive and time consuming. Accelerating the evaluation of this model could prove beneficial for its potential usage in on-line systems.

To enable such systems, in this chapter a model is derived resorting to spectral Green's function and is further accelerated by extracting the high spectral components of the integral that are associated to the reactive field i.e. the static capacitance.

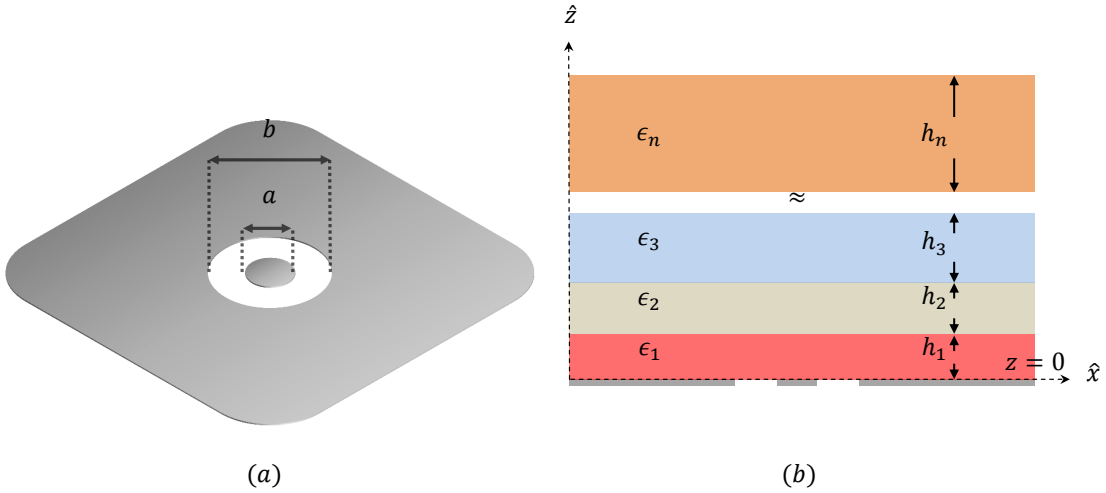

Figure 2.1: (a) Coaxial aperture realized on the ground plane. (b) Cross sectional view of the sensing element loaded with multilayer MUT characterized by dielectric constants ε_1,ε_2,ε_3...$\varepsilon_n$and thicknesses h_1,h_2,h_3...h_n

2.1 Analysis

The objective of this section, is to evaluate the input impedance of an open-ended coaxial aperture in the presence of a stratified MUT that is excited by a forward traveling current in the cable.

The geometry under analysis, schematized in Fig. 2.1 is an open-ended coaxial aperture etched on an infinite ground plane at $z = 0$. The coaxial aperture is characterized by an inner conductor of radius a and an outer conductor of radius b. The aperture is assumed to be radiating into a layered MUT in the upper half-space $z > 0$, visible in Fig. 2.1. The different layers of the MUT are characterized by permittivity's ϵ_1,ϵ_2,ϵ_3...ϵ_n and thicknesses h_1,h_2,h_3...h_n respectively. Moreover the last layer in the stratification is infinitely extending into the upper half-space.

2.1.1 Integral Equation

The desired field distributions in the two half-spaces can be derived by replacing the slot discontinuity by an equivalent magnetic current distribution on a perfectly conducting surface. Thus the problem of evaluating the fields in the two regions is divided into two separate geometries that are equivalent to the original one. Region 1 is the coaxial terminated in a short circuit at $z = 0$ and excited by an incident wave and the magnetic current.

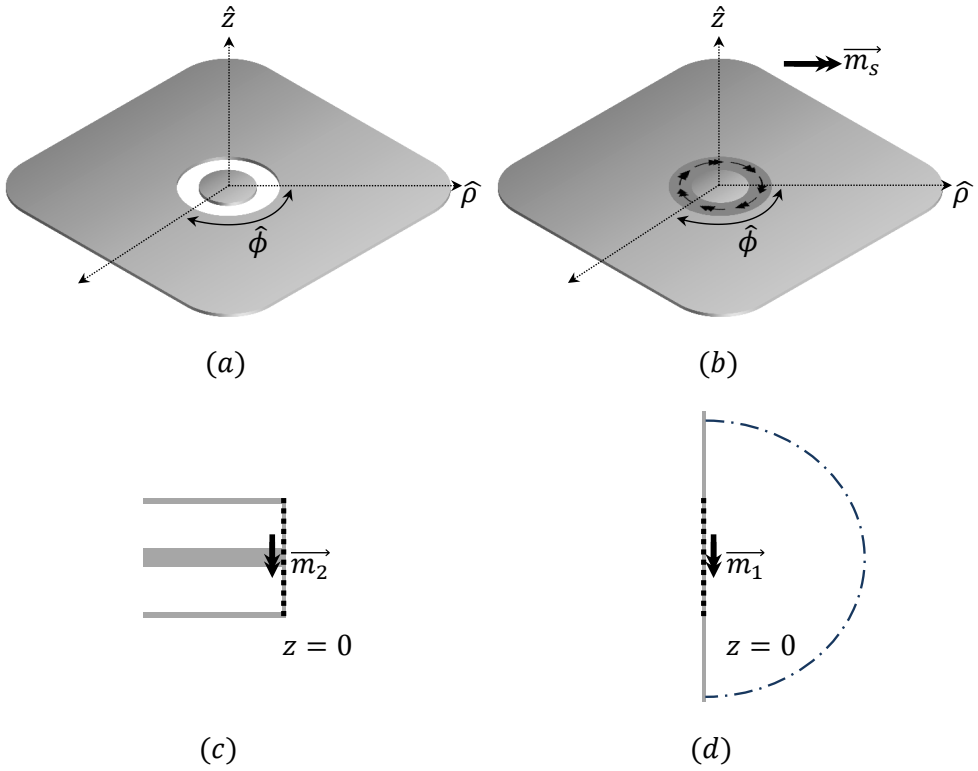

Figure 2.2: Highlights the (a) coaxial aperture etched on a ground plane, (b) Equivalent magnetic current distribution on the slot, whereas (c) and (d) represent two geometries equivalent to the original problem in (b)

Region 2 is the magnetic current on the ground plane radiating into the MUT.
The problem of a coaxial aperture radiating into an MUT can be simplified by applying the boundary condition associated to the continuity of the tangential component of the magnetic fields across the interface at $z = 0$. The continuity of the fields can be represented as follows:

$$\boldsymbol{h_1(r)} = \boldsymbol{h_2(r)} \tag{2.1}$$

where $\boldsymbol{h_1(r)}$ and $\boldsymbol{h_2(r)}$ are the magnetic fields in the two half spaces, $z < 0$ and $z > 0$ respectively. The total magnetic field can further be expressed as the superposition of an incident field, $\boldsymbol{h_l^{inc}(r)}$ and a scattered field, $\boldsymbol{h_l^{sc}(r)}$ as:

$$\boldsymbol{h_l(r)} = \boldsymbol{h_l^{inc}(r)} + \overbrace{\iint_S \bar{\bar{g}}_l^{hm}(\boldsymbol{r}, \boldsymbol{r'}) \cdot \boldsymbol{m_l(r')} d\boldsymbol{r'}}^{\text{scattered field}} \tag{2.2}$$

where $l = 1, 2$ denote the two half-spaces. Moreover the scattered field is expressed as the convolution of the dyadic spatial greens function, $\bar{\bar{g}}_l^{hm}(\boldsymbol{r}, \boldsymbol{r'})$, that gives the magnetic field from the magnetic currents, and the equivalent magnetic currents $\boldsymbol{m_l(r')}$, distributed over the aperture, $\rho \in [a, b]$ as shown in Fig. 2.2. In this problem the incident field is assumed to be a forward traveling wave in the coaxial cable hence $\boldsymbol{h}_2^{inc} = 0$. Additionally to impose the continuity of the electric field the magnetic currents in the two regions are related as follows $\boldsymbol{m_2(r')} = -\boldsymbol{m_1(r')}$. With these assumptions Eq. 2.1 can be rewritten as:

$$\boldsymbol{h_1^{inc}(r)} - \iint\limits_S \bar{\bar{g}}_1^{hm}(\boldsymbol{r}, \boldsymbol{r'}) \cdot \boldsymbol{m_1(r')} d\boldsymbol{r'} = \iint\limits_S \bar{\bar{g}}_2^{hm}(\boldsymbol{r}, \boldsymbol{r'}) \cdot \boldsymbol{m_1(r')} d\boldsymbol{r'} \tag{2.3}$$

where $\bar{\bar{g}}_1^{hm}(\boldsymbol{r}, \boldsymbol{r'})$ and $\bar{\bar{g}}_2^{hm}(\boldsymbol{r}, \boldsymbol{r'})$ are the appropriate greens functions in the two half-spaces. This is the desired integral equation that ensures the continuity of the magnetic field across the aperture. In order to solve the integral equation the incident magnetic field is assumed to be a transverse magnetic field propagating in the coaxial cable as expressed in Eq. 2.4 and the magnetic current is chosen such that it satisfies the boundary condition at the interface, refer Eq. 2.5.

$$\boldsymbol{h_1^{inc}}(z = 0, \boldsymbol{r_t}) = 2I^+ \boldsymbol{h_1(r_t)} \tag{2.4}$$

$$\boldsymbol{m_1(r')} = \hat{i}_z \times \boldsymbol{e_{coax}}(z = 0, \boldsymbol{r_t}). \tag{2.5}$$

where

$$\boldsymbol{e_{coax}}(z = 0, \boldsymbol{r_t}) = \Big(V^+ + V^-\Big) \boldsymbol{e_t(r_t)}. \tag{2.6}$$

$\boldsymbol{e_t(r_t)}$ denote the transverse electric field distribution associated to the first propagating mode in the coaxial cable [**?**], expressed as

$$\boldsymbol{e_t(r_t)} = \frac{1}{\rho \ln \frac{b}{a}} \hat{\rho}. \tag{2.7}$$

and $\boldsymbol{h_t(r_t)}$ is the transverse magnetic modal representation as stated in [?]

$$\boldsymbol{h_t(r_t)} = \frac{1}{2\pi\rho} \hat{\phi}. \tag{2.8}$$

In order to solve the integral equation we first introduce a basis function for the magnetic current.

$$\boldsymbol{m_1(r')} = V \boldsymbol{m_b(r')} \tag{2.9}$$

and

$$\boldsymbol{m_b(r')} = \frac{1}{\rho \ln \frac{b}{a}} \hat{\phi} \tag{2.10}$$

Projecting the test function, $\boldsymbol{m_t(r)} = \frac{1}{2\pi\rho}\hat{\phi}$ on either side of Eq. 2.3 results in the following reaction integral:

$$\overbrace{\iint\limits_S \left\{ \iint\limits_S g_1^{hm}(\boldsymbol{r}, \boldsymbol{r'}) \cdot m_b(\boldsymbol{r'}) d\boldsymbol{r'} \right\} \cdot m_t(\boldsymbol{r}) d\boldsymbol{r}}^{\text{internal admittance}} + \overbrace{\iint\limits_S \left\{ \iint\limits_S g_2^{hm}(\boldsymbol{r}, \boldsymbol{r'}) \cdot m_b(\boldsymbol{r'}) d\boldsymbol{r'} \right\} \cdot m_t(\boldsymbol{r}) d\boldsymbol{r}}^{\text{external admittance}} = \iint\limits_S h_1^{inc}(\boldsymbol{r}) \cdot m_t(\boldsymbol{r}) d\boldsymbol{r}. \tag{2.11}$$

After performing a few mathematical steps Eq. 2.11 can be expressed compactly as

$$\left(V^+ + V^-\right) \times \left(Y_{int} + Y_{ext}\right) = I^+. \tag{2.12}$$

where Y_{int} and Y_{ext} are the internal and external adnittances. The external admittance, Y_{ext} at the aperture plane $z = 0$ can be further expressed as

$$Y_{ext} = \frac{\pi}{\ln \frac{b}{a}} \int\limits_a^b \boldsymbol{h}[\rho, \phi, z; m_b(\boldsymbol{r'})] d\rho \tag{2.13}$$

where $\boldsymbol{h}[\rho, \phi, z; m_b]$ is the magnetic field scattered by the magnetic currents $m_b(\boldsymbol{r'})$ onto the coaxial aperture in the presence of the MUT. Magnetic field can be evaluated as the convolution of $g_{\phi\phi}^{hm}(\boldsymbol{r}, \boldsymbol{r'})$ and $m_b(\boldsymbol{r'})$ as

$$\boldsymbol{h}(\rho, \phi, z) = \int_0^{2\pi} \int_a^b g_{\phi\phi}^{hm}(\rho, z; \rho', \phi', z') m_b(\rho') \rho' d\rho' d\phi' \tag{2.14}$$

where the spatial greens function is (refer [50])

$$g_{\phi\phi}^{hm}(\boldsymbol{r}, \boldsymbol{r'}) = \frac{1}{2\pi} \int\limits_0^\infty \frac{1}{k_\rho} I_{TM}(k_\rho; z, z') \frac{\partial}{\partial \rho'} J_0(k_\rho \rho') \frac{\partial}{\partial \rho} J_0(k_\rho \rho) dk_\rho. \tag{2.15}$$

k_ρ is the radial spectral variable, $I_{TM}(k_\rho; z, z')$ the transverse magnetic spectral current at z due to a series voltage source at z' (equivalent transmission line shown in Appendix-A in [51]) and J_0 is the zeroth-order bessel function. Substituting the greens function in Eq. 2.15

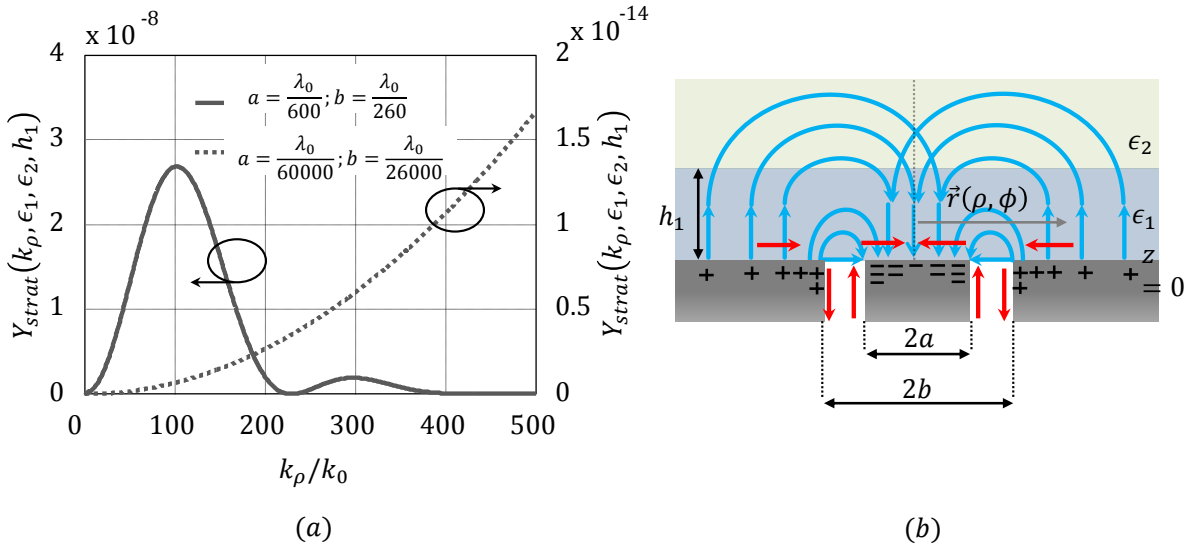

Figure 2.3: (a) Admittance spectrums versus normalised spectral variable k_ρ of a coaxial aperture with dimensions outlined in the inset.

to evaluate the field in Eq. 2.14 and using the identity $\int_a^b \frac{\partial}{\partial \rho'} J_0(k_\rho \rho') d\rho' = J_0(k_\rho b) - J_0(k_\rho a)$ and azimuthal symmetry in ϕ' enables the external admittance to be expressed as a single integral in the spectral variable k_ρ

$$Y_{ext}(a, b, h_i, \epsilon_i) = \frac{\pi}{\ln^2 \frac{b}{a}} \int_{k_\rho=0}^{\infty} \frac{[J_0(k_\rho a) - J_0(k_\rho b)]^2}{k_\rho} I_{TM}(k_\rho, h_i, \epsilon_i) dk_\rho. \tag{2.16}$$

Where $i = 1, 2, \cdots, n$; $h_1, h_2, \cdots, h_n; \epsilon_1, \epsilon_2, \cdots, \epsilon_n$ are the thicknesses and the permittivities of the n dielectric MUT layers. The integration in Eq. 2.16 for the case of freespace can be recognised as the same that is presented in [52].

2.1.2 Admittance Spectrum

The spectrum of the integral in Eq. 2.16 exhibit a decaying oscillatory behavior. Oscillations are attributed mainly due to the bessel functions and the decaying behavior due to the $\frac{I_{TM}(k_\rho, h_1 \cdots h_n, \epsilon_1 \cdots \epsilon_n)}{k_\rho}$ term in Eq. 2.16. The rate at which the spectrum decays depends on how small the coaxial is in terms of the wavelength. This can be observed from the spectrum plots in Fig. 2.3 for different dimensioned coaxials having a characteristic impedance of 50Ω.

Before focusing on the techniques to accelerate the evaluation of the integration in Eq.

2.16 it is useful to provide a physical picture of the meaning of the admittance in Eq. 2.16. The admittance represents the current $I(z = 0)$ when $V(z = 0) = 1$, in the coaxial line, flowing in the positive z-direction at the cross section $z = 0$. With reference to Fig. 2.3, since the line is open circuited, the current in the inner conductor would be infinitesimal in the presence of an hollow cylinder made fom an infinitely thin conductor. However, the admittance from Eq. 2.16 will be different from zero due to the fact that the actual surface current (in red in Fig. 2.3) flowing in the positive z direction bends at the $z = 0$ cross section and continues in the inward radial direction until the center of the inner conductor of the coaxial cable which is metallized (see Fig. 2.3(a) and (b) for the lateral cross section and the top expanded views respectively). It is clear that a larger inner conductor would lead directly to a larger admittance since these current bending can be directly associated to an accumulation of charges that in turn can be associated to a capacitive loading.

2.1.3 Two step extraction of quasi-static capacitance

In the following subsection the integral in Eq. 2.16 is accelerated by extracting the quasi-static capacitance associated to the dielectric closest to the source. To this goal the external admittance, $Y_{ext}(a, b, h_i, \epsilon_i)$ is expressed as a superposition of a regularized admittance, $Y_{reg}(a, b, h_i, \epsilon_i)$ and a homogeneous admittance, $Y_{hs}(a, b, \epsilon_1)$ as shown in Eq. 2.17. The circuital representation of the same is presented in Fig. 2.4. The regularized admittance depends on all the geometrical parameters of the MUT, while the homogeneous admittance depends only on the permittivity of the first dielectric closest to the aperture. In the following analysis the MUT is considered to be two layered, i.e. $i = 2$ with permittivity's ϵ_1, ϵ_2 and thicknesses $h_1, h_2 \to \infty$.

$$Y_{ext}(a, b, h_i, \epsilon_i) = Y_{reg}(a, b, h_i, \epsilon_i) + Y_{hs}(a, b, \epsilon_1) \tag{2.17}$$

Regularized Admittance, $Y_{reg}(a, b, h_i, \epsilon_i)$

The regularized admittance, $Y_{reg}(a, b, h_i, \epsilon_i)$ in Eq. 2.17 can be spectrally expressed as:

$$Y_{reg}(a, b, h_i, \epsilon_i) = \frac{\pi}{\ln \frac{b}{a}} \int_{k_\rho=0}^{\infty} \frac{[J_0(k_\rho a) - J_0(k_\rho b)]^2}{k_\rho} \Big(I_{TM}(k_\rho, h_i, \epsilon_i) - I_{TM}^{hs}(k_\rho, \epsilon_1) \Big) dk_\rho. \tag{2.18}$$

where $i = 1, 2$ denote the two dielectric in the stratification. This choice of representation for the regularized admittance ensures faster convergence in the spectral domain as the high spectral components associated to the medium very close to the sensor i.e. first

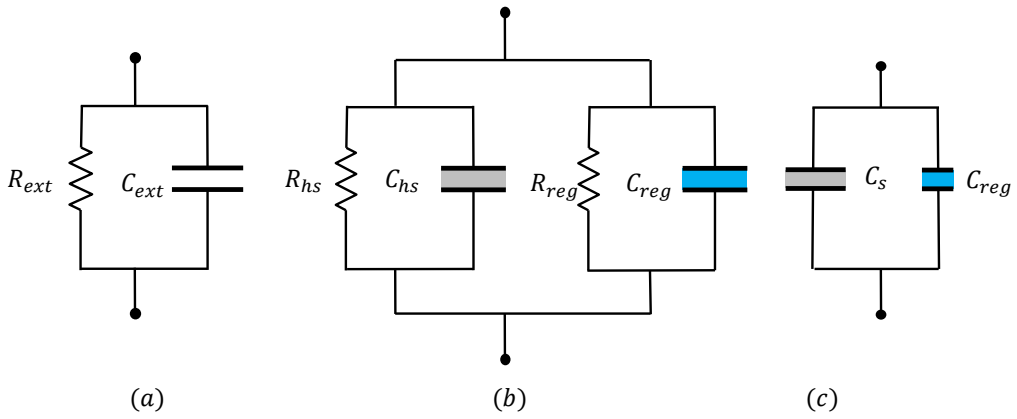

Figure 2.4: (a) External impedance at the coaxial aperture composed of R_{ext} and C_{ext}. (b) Z_{ext} further decomposed as the parallel of a regularized and homogeneous terms. (c) The size of the two capacitors correspond to the capacitance contribution of the two terms.

dielectric is subtracted. This can be observed from Fig. 2.5 where the external admittance spectrum, $\widetilde{Y}_{ext}(k_\rho, h_i, \epsilon_i)$ and regularized admittance spectrum, $\widetilde{Y}_{reg}(k_\rho, h_i, \epsilon_i)$ are plotted versus normalized k_ρ for an aperture with radii $a = 1$ mm and $b = 2.3$ mm. Fig. 2.5(a) highlights the convergence for two layered MUT characterized by $\epsilon_1 = 2.1, \epsilon_2 = 10$ and $h_1 = 3$ mm while Fig. 2.5(b) for $\epsilon_1 = 2.1, \epsilon_2 = 10$ and $h_1 = 1$ mm. From the spectrums presented in Fig. 2.5 one can observe that the spectrum of the regularized admittance is inversely proportional to the thickness h_1.

Homogeneous Admittance, $Y_{hs}(a, b, \epsilon_1)$

Moreover the homogeneous admittance, $Y_{hs}(a, b, \epsilon_1)$ can also be expressed spectrally as :

$$Y_{hs}(a, b, \epsilon_1) = \frac{\pi}{\ln \frac{b}{a}} \int_{k_\rho=0}^{\infty} \frac{[J_0(k_\rho a) - J_0(k_\rho b)]^2}{k_\rho} I_{TM}^{hs}(k_\rho, \epsilon_1) dk_\rho. \tag{2.19}$$

where $I_{TM}^{hs}(k_\rho, \epsilon_1)$ is the homogeneous space transverse magnetic spectral current flowing in the transmission line equivalent to a magnetic source radiating in a homogeneous space with dielectric permittivity ϵ_1. Opening the spatial integrals in ρ and ρ' and rewriting the above integral results in:

$$Y_{hs}(a, b, \epsilon_1) = \frac{k}{\zeta \ln^2 \frac{b}{a}} \int_{\rho=a}^{b} \int_{\rho'=a}^{b} 2\pi j \int_{k_\rho=0}^{\infty} \frac{k_\rho}{\sqrt{k^2 - k_\rho^2}} J_1(k_\rho \rho) J_1(k_\rho \rho') dk_\rho d\rho d\rho'. \tag{2.20}$$

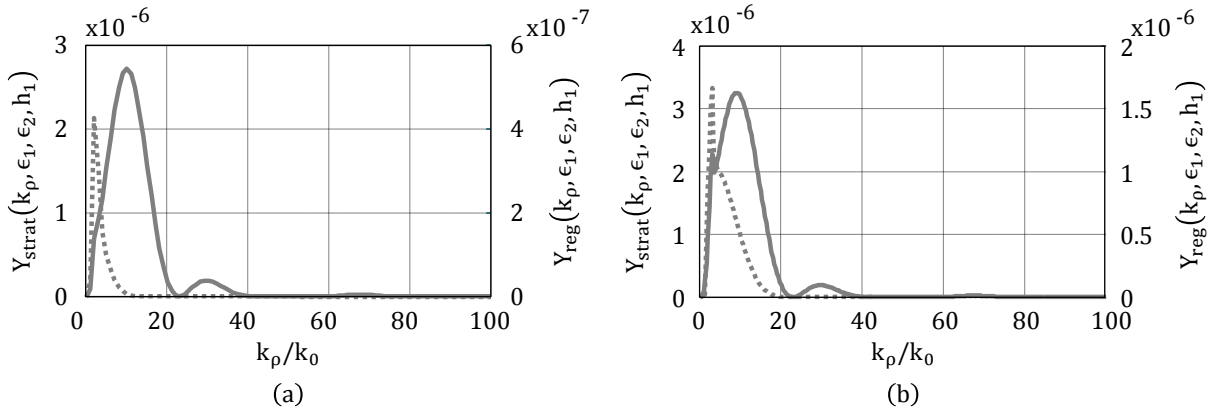

Figure 2.5: External admittance and regularized spectrum versus normalized spectral variable k_ρ for two different thickness of the first dielectric (a) $h_1 = 3$ mm (b) $h_1 = 1$ mm. Bold grey line represents $\widetilde{Y}_{ext}(h_1 = 3mm, 1mm, \epsilon_1 = 2.1, \epsilon_2 = 10)$, while dotted grey line represent $\widetilde{Y}_{reg}(h_1 = 3mm, 1mm, \epsilon_1 = 2.1, \epsilon_2 = 10)$

.

where k and ζ are the propagation constant and the wave impedance in the medium. In the above expression $k_z = \sqrt{k^2 - k_\rho^2}$ was taken to be converging when $\mathfrak{Im}\, k_z \leq 0$. The integral in k_ρ can be further expressed as

$$2\pi \int_{k_\rho=0}^{\infty} \frac{k_\rho}{\pm\sqrt{k_\rho^2 - k^2}} J_1(k_\rho\rho) J_1(k_\rho\rho') dk_\rho d\rho d\rho'. \tag{2.21}$$

However one can identify that the spectral integral can be written as a spatial integral in ϕ using the identity in [46] Pg. 42.

$$2\pi \int_{k_\rho=0}^{\infty} \frac{k_\rho}{\pm\sqrt{k_\rho^2 - k^2}} J_1(k_\rho\rho) J_1(k_\rho\rho') dk_\rho d\rho d\rho' = \int_0^{2\pi} \frac{e^{jk|\boldsymbol{r}-\boldsymbol{r'}|}}{|\boldsymbol{r}-\boldsymbol{r'}|} \cos(\phi) d\phi. \tag{2.22}$$

This enables the homogeneous space admittance, $Y_{hs}(a, b, \epsilon_1)$ to be evaluated completely in the spatial domain as follows:

$$Y_{hs}(a, b, \epsilon_1) = \frac{k}{\zeta \ln^2 \frac{b}{a}} \int_{\rho=a}^{b} \int_{\rho'=a}^{b} \int_{0}^{2\pi} \frac{e^{jk|\boldsymbol{r}-\boldsymbol{r'}|}}{|\ \boldsymbol{r}-\boldsymbol{r'}\ |} \cos(\phi) d\phi d\rho d\rho'. \tag{2.23}$$

It is evident from the above equation that there exists a singularity when $\boldsymbol{r} = \boldsymbol{r'}$ i.e. when the source and the observation points coincide. Extracting the singularity in Eq. 2.23

results in Eq. 2.23 being expressed as a sum of a dynamic and a quasi-static contribution as:

$$Y_{hs}(a,b,\epsilon_1) = Y_{hs}^{dyn}(a,b,\epsilon_1) + j\omega C_s(a,b,\epsilon_1). \tag{2.24}$$

where $Y_{hs}^{dyn}(a,b,\epsilon_1)$ is negligible for low frequency regime and $C_s(a,b,\epsilon_1)$ is independent of frequency and needs to be evaluated numerically only once.

$$C_s(a,b,\epsilon_1) = \frac{\epsilon_0\epsilon_1}{\ln^2\frac{b}{a}} \int_{\rho=a}^{b}\int_{\rho'=a}^{b}\int_{0}^{2\pi} \frac{1}{\mid \boldsymbol{r}-\boldsymbol{r'} \mid}\cos(\phi)d\phi d\rho d\rho'. \tag{2.25}$$

Substituting Eq. 2.25 in Eq. 2.17, the external admittance can be finally expressed a

$$Y_{ext}(a,b,h_i,\epsilon_i) = Y_{reg}(a,b,h_i,\epsilon_i) + j\omega C_s(a,b,\epsilon_1). \tag{2.26}$$

Assuming that the sensor's dimensions are micrometric, the homogeneous and regularized impedances can be approximated as purely capacitive: $Z_{hs}(a,b,\epsilon_1) \approx \frac{1}{j\omega C_{hs}(a,b,\epsilon_1)}$ and $Z_{reg}(a,b,h_i,\epsilon_i) \approx \frac{1}{j\omega C_{reg}(h_i,\epsilon_i)}$. Moreover, in the low frequency regime $C_{hs}(a,b,\epsilon_1) \approx C_s$ since in Eq. 2.24 the dynamic part of the admittance can be assumed to be negligible. Thus for electrically small sensors the equivalent network in Fig. 2.4(b) can be explicitly represented as in Fig. 2.4(c), as the parallel of two lumped capacitors. The size of the two capacitances are drawn in proportion to the values associated to the homogeneous term and the regularized terms (which incorporates the stratification of the MUT). As an example, pertinent to higher frequencies and larger dimensions of the sensing element, the real and imaginary part of the total admittance is plotted in Fig. 2.6 as a function of a very large frequency sweep (0.05 GHz to 5 GHz) for $h_1 = 1$ mm,ϵ_1=4.1 and ϵ_2=10. In the same figure, the regularized admittance, dynamic admittance and the static capacitance is also reported. The curves are plotted for coax dimensions $a = 1$ mm, $b = 2.3$ mm; and $a = 2$ mm, $b = 4.6$ mm respectively. Comparing curves pertinent to small and large coaxial structure it is apparent that for larger diameters the total admittance is larger, corresponding to larger capacitances. However it is also worth noticing that for larger diameters the relative amplitude of the regularized admittance with respect to the total admittance is much larger suggesting a significant dependence of the total admittance from the dielectric under test (in this case ϵ_2=10). For lower frequency regime of operation the dynamic admittance is negligible, as shown in Fig. 2.6(a) and (b) with grey bold and dashed lines.

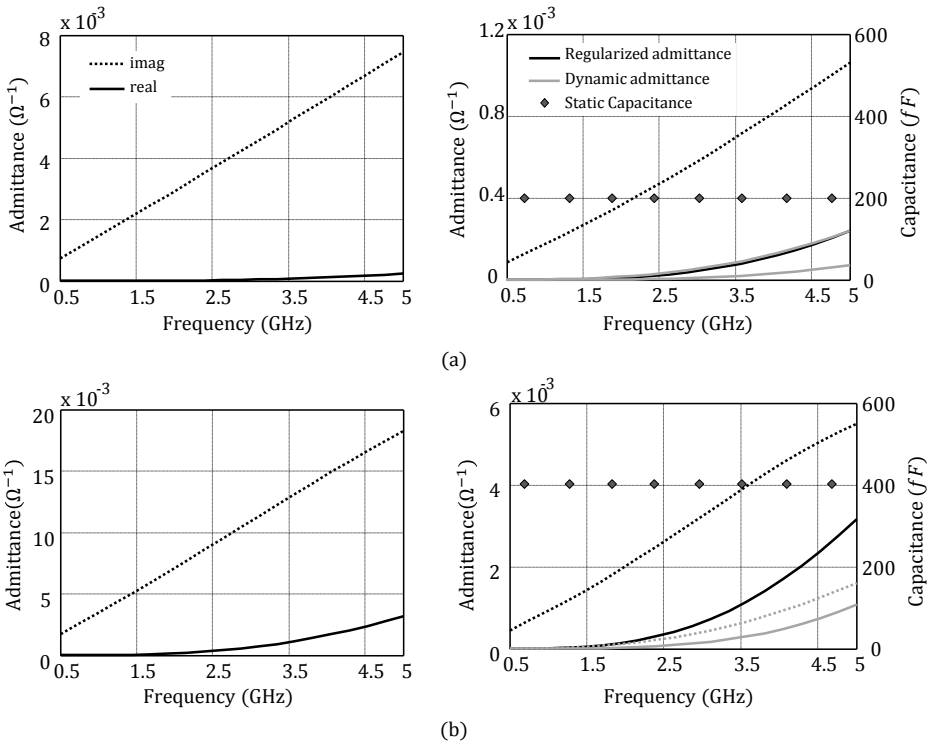

Figure 2.6: Represent the input admittance of a coaxial sensor versus frequency(figure on the left), which is further expressed in terms of the regularized admittance, dynamic admittance and static capacitance(figure on the right) for two dimensions of the coaxial. (a) a=1 mm and b=2.3 mm. (b) a=2 mm,b=4.6 mm.

2.2 Conclusion

In this chapter a magnetic field integral equation (MFIE) was setup across the coaxial aperture to analyze the radiation behavior of the element. The external admittance of a coaxial aperture was presented using the spectral greens function to account for the stratified MUT. A methodology to accelerate the evaluation of the reaction integral is outlined by extracting the singularity in the integral associated to the quasi-static capacitance. Representing the external admittance as the superposition of the regularized admittance and the quasi-static capacitance will facilitate in performing the sensitivity analysis and designing the sensing element in the next chapter.

Chapter 3

Permittivity Extraction of Layered Biological Sample using Coaxial Probe

Broadband dielectric spectroscopy is used as a non-invasive diagnostic tool to identify a material under test (MUT) or its state due to its unique frequency dependent permittivity signature [53, 54]. This feature promotes the usage of this technique as a means to characterize materials in agricultural, automobile, biomedical and chemical industry, among others. The strong variation in permittivity, based on the cell water and sugar content [55], suggest that dielectric spectroscopy can be used to identify or stage the internal physiological changes of a given material over a period of time. When stratified media are considered most often the lower permittivity of the external layer masks variation in the internal layer. Biological samples such as fruits have stratified arrangement of layers with different electrical properties and varied thicknesses, such as skin, pulp and seed. The pulp in particular provides substantial information on the state of the fruit such as the ripening stage and internal defects [53]. However, the low dielectric value of the skin layer (due to the lower concentration of water when compared to the pulp), tends to desensitizes the measurement of the pulp layer. Hence, to properly characterize the effective state (i.e., permittivity) of the internal layer it is critical to remove the effect of the skin. It is important to mention that the internal defect in mangoes, due to a structural breakdown, leading to internal browning are difficult to identify from firmness measurements, optically or using computer vision tools. In this chapter, we present a technique based on open-ended coaxial probe dielectric spectroscopy combined with a fast numerical model based on spectral Green's functions described in the previous chapter.

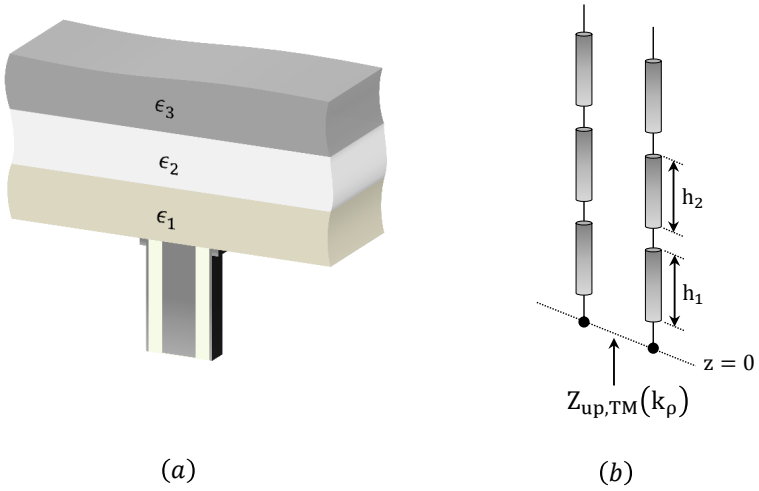

Figure 3.1: Coaxial probe in contact with dielectric layers characterized by permittivity's ϵ_1, ϵ_2 and ϵ_3 with thicknesses h_1, h_2 and infinitely extending last layer. (a) Three dimensional view and (b) equivalent transmission line representation of the dielectric stratification.

3.1 Model

The input admittance of a coaxial aperture can be expressed using Eq. 2.16 which accounts for the coaxial dimensions, thicknesses and permittivities pertinent to every layer in the dielectric stratification.

$$Y_{ext}(a,b,h_i,\epsilon_i) = \frac{\pi}{\ln^2 \frac{b}{a}} \int_{k_\rho=0}^{\infty} \frac{[J_0(k_\rho a) - J_0(k_\rho b)]^2}{k_\rho} I_{TM}(k_\rho, h_i, \epsilon_i) dk_\rho \tag{3.1}$$

where $i = 1, \cdots, n$ and n is the number of dielectric layers. Referring to the equivalent z-transmission line representation of the stratified medium in Fig. 3.1, the transverse magnetic spectral current $I_{TM}(k_\rho, h_i, \epsilon_i)$ in Eq. 3.1 can be evaluated as

$$I_{TM}(k_\rho; h_i, \epsilon_i) = \frac{1}{Z_{up,TM}(k_\rho, h_i, \epsilon_i)} \tag{3.2}$$

where $Z_{up,TM}(k_\rho, h_i, \epsilon_i)$ is the input impedance of the dielectric stack in the upper half space ($z > 0$). For transverse magnetic incidence the transmission lines have characteristic impedance $Z_i^{TM} = \zeta_i \frac{k_{zi}}{k_i}$, where ζ_i and k_i are the impedance and wavenumber pertaining to the i^{th} layer with $k_{zi} = \sqrt{k_0^2 \epsilon_i - k_\rho^2}$. Moreover, regardless of the number of dielectric layers, the spectral current can be evaluated very easily using Eq. 3.2 by computing the input impedance of the equivalent transmission line network.

3.2 Complex Permittivity Extraction

In the following section we will consider the food quality scenario and use the proposed model to evaluate the complex permittivity of mango pulp. The main motivation for having chosen mango as a measurement sample was because it was the fruit of the season. Mangoes can be modelled as a two layered medium with the skin and the pulp being the outer and inner layer respectively. When considering open-ended coaxial probe measurements (i.e., near field), the pulp can be considered as an infinitely extending layer, as its volume is significantly larger with respect to the penetration of the evanescent field generated at the probe aperture. With an a-priori knowledge on the range of thickness of the skin h_1 and the permittivity of the skin ϵ_1, the permittivity of the pulp ϵ_2 can be found by minimizing the following cost function

$$\left| \frac{Y_{meas} - Y_{model}}{Y_{model}} \right| < 10^{-3}. \tag{3.3}$$

Where Y_{meas} is obtained via measurements performed on the sample and Y_{model} is computed using Eq. 3.1.

3.2.1 Measurement Setup

S-parameter measurements are performed using a custom built open-ended coaxial probe setup connected to a Field-Fox Keysight vector network analyzer as shown in Fig. 4.6. The probe inner radius is 0.523 mm while the outer radius is 1.5 mm. The outer and inner conductors are made of copper while teflon is the probe dielectric. The MUT, here the mango, is placed on the lab jack and raised until the probe is in direct contact with the skin with no airgaps between the probe aperture and the skin.

3.2.2 Experimental Results

Pulp permittivity extraction validation

To validate the extraction of the permittivity of the pulp using the approach described in the chapter the following experiment was carried out:

1. Γ measurements were performed on the exterior of several mangoes (gray trace in Fig. 3.3), on five different locations. Measured Γ is subsequently translated into normalised admittance using $Y_{meas} = \frac{1-\Gamma}{1+\Gamma}$.

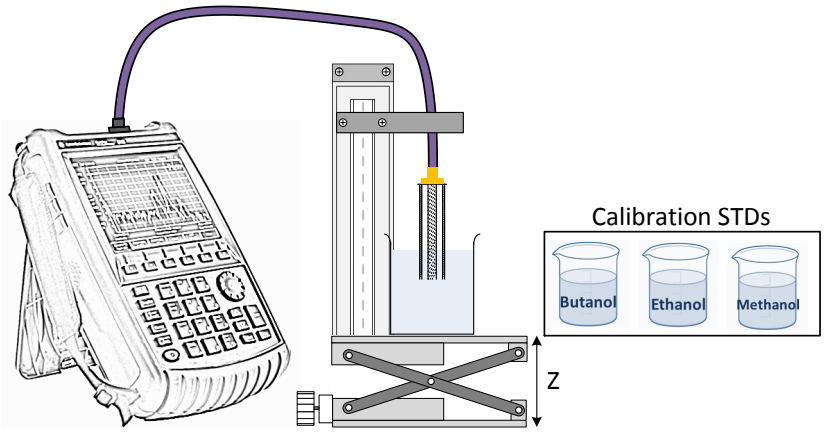

Figure 3.2: Measurement setup consisting of an open-ended coaxial probe connected to the VNA via a cable. The three liquids shown in the inset are used for a direct, liquid based calibration at the probe aperture.

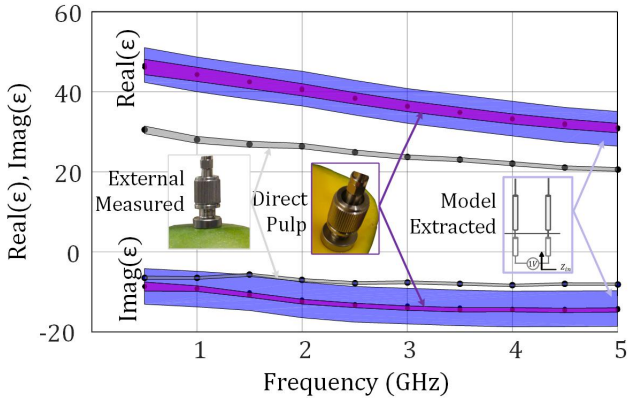

Figure 3.3: Mean and min/max variation of the complex permittivity of: mangoes external measurements on 5 locations (gray trace), direct pulp measurements of four different mangoes (purple trace), pulp permittivity extracted using the analytical tool (light blue trace).

2. Moreover direct pulp measurements were performed on 5 mangoes to obtain reference data (purple trace in Fig. 3.3).

3. The permittivity of the pulp was extracted using the data from 1) and the analytical tool (light blue trace in Fig. 3.3).

The larger standard deviation of the extracted pulp permittivity can be attributed to the deviation in the actual thickness of the skin from the assumed value during optimization.

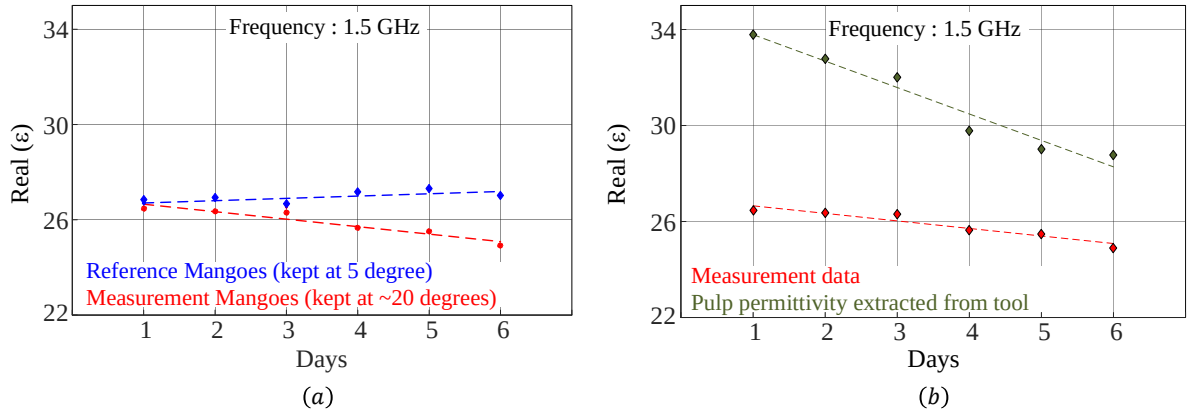

Figure 3.4: Variation of the real part of the mean permittivity of (a) reference and sample mangoes in blue and red respectively. The dashed lines represent the line of best fit (least square method). (b) Extracted epsilon values of sample mangoes before and after applying the analytical model in red and green respectively.

Ripening stages of a Mango

A study on the ripening process (over a duration of seven days) of mangoes was performed using six sample and two reference mangoes. The temperature of the reference mangoes was maintained at 5 degree celcius during the course of the study to delay the ripening process while the sample mangoes were in a controlled room-temperature environment of 20 degree celcius. Measurements were performed at five different locations on every sample and reference mangoes from 0.5 GHz to 5 GHz. Initially, the complex permittivity was extracted using RFM model [56] at the aperture plane without bifurcating the MUT as a two layered medium. The extracted permittivity was averaged over all the measurement locations for both the sample (ripening) and reference mangoes at every frequency point. In Fig. 3.4 the real part of the extracted epsilon over a duration of six days is reported. We can observe a clear trend in the variation of the complex permittivity with the ripening process, although the contrast in the values are very limited. However, when the model is applied to extract the permittivity of the pulp alone, under the assumption that the permittivity of the skin does not vary significantly, we observe a much higher variation at the same frequency (Fig. 3.4).

Internal Defects in a Mango

To investigate on the internal defects of Mangoes, measurements were performed on five samples which appeared healthy from external appearance, while one amongst them,

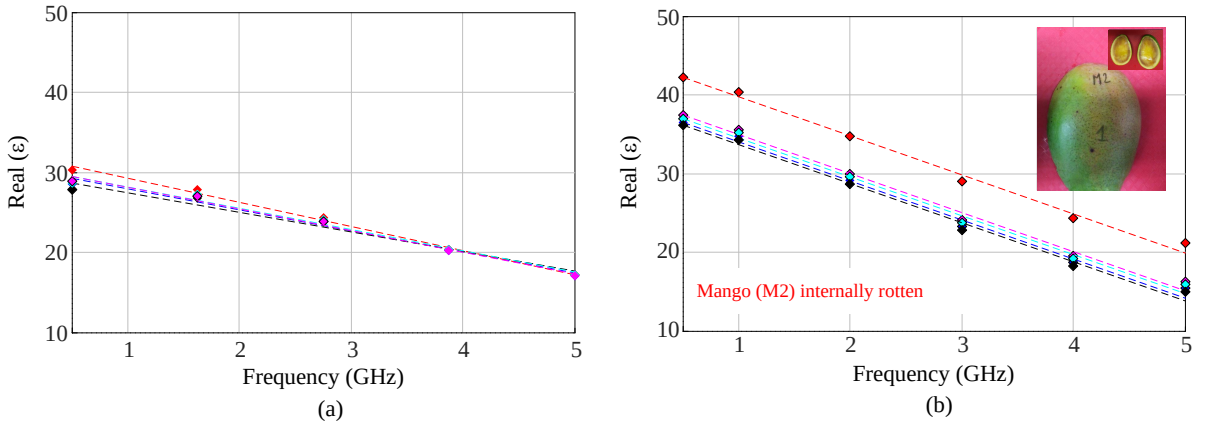

Figure 3.5: (a) Average epsilon values extracted from Γ measurements on the surface of the samples. (b) Extracted epsilon values related to the pulp using the analytical model.

marked M2, was rotten from within as shown in Fig. 3.5. In Fig. 3.5 the mean complex permittivity extracted from each of the samples (considering 5 measurement point per sample) is presented. The extracted dielectric values from all the samples show limited variation, however M2 (red dotted line) show higher permittivity compared to the other samples Fig. 3.5(a). Whereas, post-processing the extracted dielectric values by applying the analytical model clearly differentiates M2 from other mangoes with higher permittivity values, see Fig. 3.5(b).

3.3 Conclusion

A technique, based on spectral Greens' function, to extract the complex permittivity of the mango pulp considering mango has a stratified layered medium using an open-ended coaxial probe was presented. The extracted pulp epsilon was validated with direct measurements. The tool was then subsequently used to enhance the sensitivity in identifying the ripening staging and to identify internal defects (non-visible) in mangoes.

Chapter 4

Detection Depth Analysis of Coaxial based Permittivity Sensors

In this chapter, the sensitivity of a coaxial/coaxial based permittivity sensors to the alteration in the complex permittivity of the medium under test (MUT) from its initial state is specifically addressed. For a given permittivity sensor, high spatial resolution and high sensitivity typically come at the expense of poor detection depth. An informed trade-off in this regard requires an accurate electromagnetic modelling of the sensor accounting for the geometrical dimensions and electrical properties of the sensor and the MUT. Therefore in order to address this a qualitative parameter named Sensitivity, S is defined in this chapter that will assist in designing an efficient sensor based on the requirements.

4.1 Sensitivity of a Coaxial Sensor

In the following section the MUT is modelled as a two layered medium and the sensitivity analysis is performed for changes in the permittivity of the second layer for a given height and permittivity of the first layer.The choice of this configuration is to study the ability of the sensor to detect changes in a layered medium where the first layer is unchanging.
The sensitivity of a dielectric sensor to the variations in the permittivity of the MUT, ϵ_{MUT} predominantly depends on the geometry of the sensor. Most often in integrated technology the read out circuit is a tunable impedance bridge, depicted in Fig. 4.1. The bridge is composed of three variable capacitors, C_{var} each composed of capacitor banks that can be tuned in steps of C_0. The voltage across the terminals $A - A'$, $V_{AA'}$ is different from zero when the load, $Y_{ext}(a, b, h_1, \epsilon_1, \epsilon_{MUT})$ assessed by the sensor deviates from the balanced condition. The initial level of C_{var} is set by sensing a reference sample and

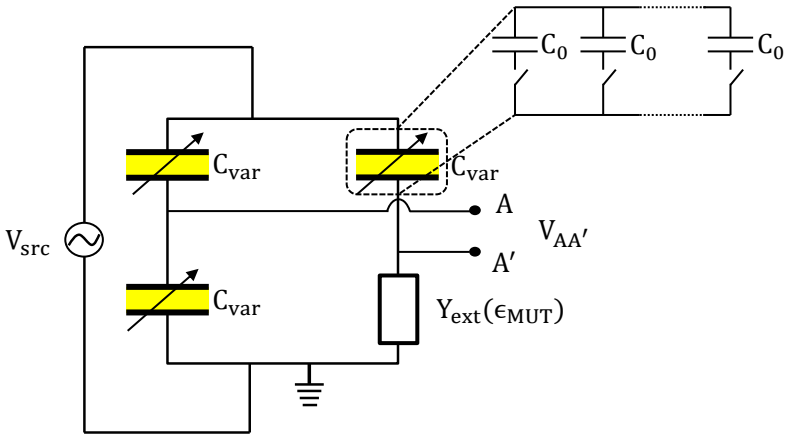

Figure 4.1: Represents the read-out circuitry, RF equivalent network based on lumped capacitor banks.

accordingly varying the capacitors to read a minimal voltage $V_{AA'}$. The voltage $V_{AA'}$ is further expressed in terms of ϵ_{MUT} as

$$V_{AA'} = \frac{V_{src}}{2}\left\{\frac{Z_{MUT} - Z_{ref}}{Z_{MUT} + Z_{ref}}\right\} \tag{4.1}$$

where $Z_{MUT} = Y_{ext}(a, b, h_1, \epsilon_1, \epsilon_{MUT})^{-1}$ and $Z_{ref} = Y_{ext}(a, b, h_1, \epsilon_1, \epsilon_{ref})^{-1}$. Moreover ϵ_{ref} and ϵ_{MUT} refer to the change in the second dielectric, ϵ_2 in Fig. 4.2. Accordingly, it is convenient to introduce a qualitative parameter, Sensitivity S, that can help in the design of the sensing element. Such sensitivity is defined as

$$S = \frac{Z_{MUT} - Z_{ref}}{Z_{MUT} + Z_{ref}} \tag{4.2}$$

4.1.1 Parametric Study

As established in the previous chapter the regularization capacitance of a coax with a smaller spacing between the inner and outer conductors is relatively much smaller than the larger coax with a larger spacing. This implies that the sensitivity of the sensor from the dielectric constant ϵ_2 is very small when the dimensions of the coaxial aperture are smaller than the thickness of the substrate. In order to increase the sensitivity of the sensor it is essential to increase the spacing between the inner and the outer conductor or realize a larger coaxial line. Fig. 4.2 schematizes the electric field distribution in the stratified medium, and presents two different qualitative pictures for small and large coaxial average radii, $r_{ave} = (a + b)/2$. The green arrows in Fig. 4.2 depict electric field lines uniting

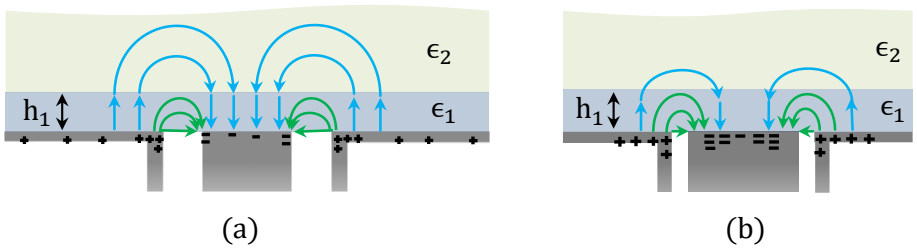

Figure 4.2: Pictorial representation of the electric field lines (in blue and green) in the dielectric stratification, and the charge distribution in an open-ended coaxial cable for a large and small size probe.

positive and negative charges from the outer conductor to the inner conductor through the first medium, ϵ_1. The blue arrows depict electric field lines which cross into the second medium, ϵ_2.

The advantages in terms of sensitivity of larger radii coaxial cables can be observed in Fig. 4.3. Here the sensitivity from Fig. 4.2 is presented assuming $\epsilon_{ref} = 1$ and $\epsilon_{MUT} = 40$, as a function of the average radii of a coaxial probe, r_{ave} in the presence of the stratification, $\epsilon_1 = 4$, $h_1 = 1$ mm. In Fig. 4.3(a) sensitivity is plotted versus the normalised average radii of the coaxial sensing element for a 50Ω coaxial line and of a coaxial line characterized by (b-a)=1 mm. The increased sensitivity for larger radii can be associated with more field lines penetrating the MUT, as in Fig. 4.2. Fig. 4.3(b) describes parametrically the sensitivity of coaxial lines of different radii as a function of thickness h_1. It is apparent that the sensitivity of larger coaxial (which has a larger spacing between the inner and outer conductors) is always higher. Fig. 4.3(c) shows the comparison between the capacitances versus the normalised average radii plots obtained from our analytical tool and HFSS for $\epsilon_{ref} = 1$ and $\epsilon_{MUT} = 40$, the good comparison between the results gives us confidence in the sensitivity plots obtained using the analysis tool described in the previous chapter. Finally, Fig. 4.3(d) shows the variation in the sensitivity versus the radius of the inner conductor for three different gaps (i.e. b-a) between the conductors. It is evident from this analysis that as the spacing between the conductors increase the sensitivity also increases for a given radius of the inner conductor.

4.2 Loadings for the Coaxial Line

As explained in Fig. 4.3 in the previous section, one way to enhance the sensitivity of the sensor is to realize a larger coaxial probe. While still resorting to planar technology

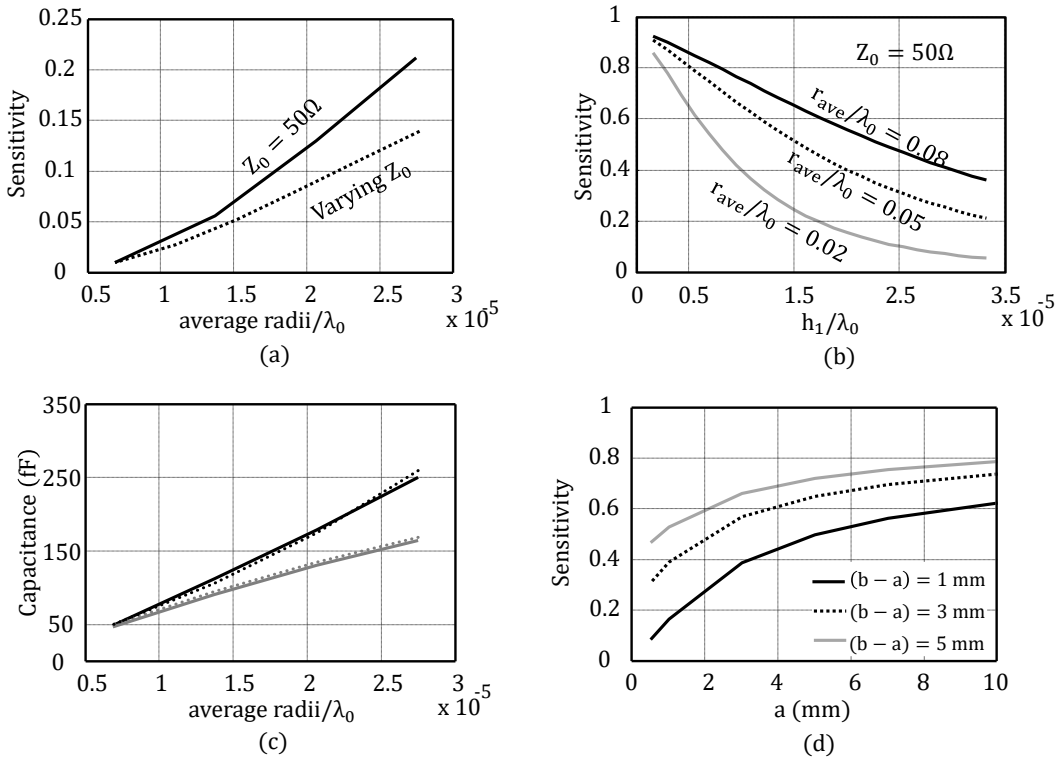

Figure 4.3: Sensitivity of the sensing element versus (a) the normalized average radii for 50Ω and varying characteristic impedance of the probe. (b) the normalized thickness h_1 of the first dielectric for different probe dimensions with $Z_0 = 50\Omega$. Capacitance versus (c) normalized average radii. Black and grey lines represent the capacitance evaluated for $\epsilon_{MUT} = 40$ and $\epsilon_{ref} = 1$ respectively.

a possibility to realize a larger coaxial aperture is by terminating the via with a circular patch, as in Fig. 4.4(a).

4.2.1 Coaxial terminated by a patch loading

The external impedance at the aperture of the inner coaxial line $[\rho \in (a, b); z = 0]$ is impacted by the pin and patch loading, Fig. 4.4(b), such that the loading enhances the electric current flowing through the coaxial aperture. Seen from the top the current on the patch loading and the ground plane will still look similar to the coaxial case, but with proportionally much smaller aperture with respect to the average radius r_{ave}. At least in static terms, the admittance contribution due to the loading of the patch and the pin can be imagined to be equivalent to that of a much larger coaxial probe. In fact the external

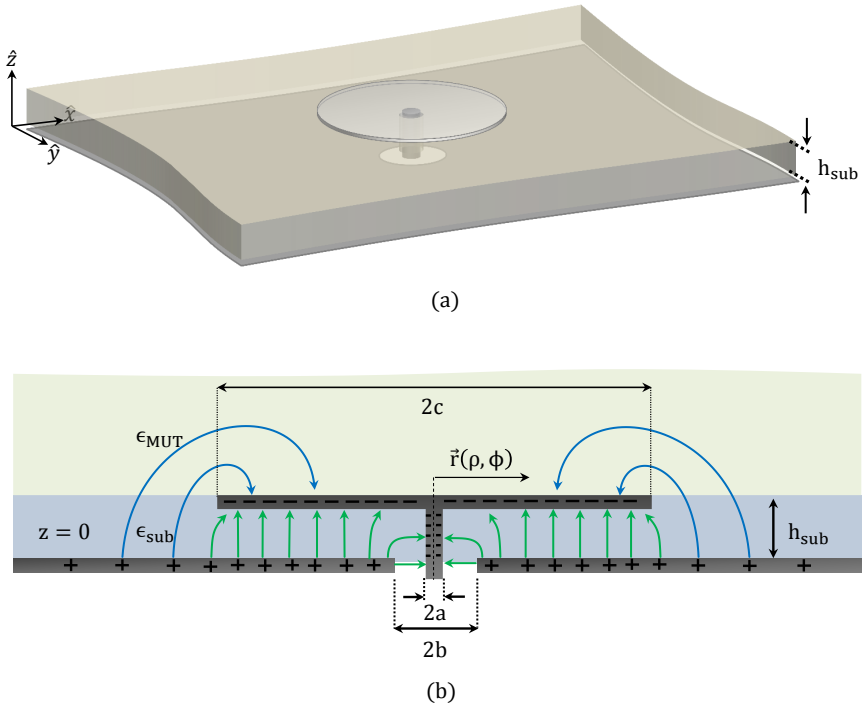

Figure 4.4: Patch terminated coaxial sensor. (a)3-dimensional view and (b)Cross sectional view of the sensor. The greens lines represent the electric field lines between the patch and the ground plane while the blue lines represent the fringing field lines.

total capacitive loading, $j\omega C_{ext}$, is proportional to the accumulated charge for a given impressed voltage: $C_{ext} = \frac{Q}{V}$. It is apparent that the charge that can be stored in the surfaces of the pin and patch will be much larger than the one that can be stored in the surface of the center conductor of the coaxial guide, simply because of the much larger physical area over which the charges can be accumulated. The complication with respect to the open-ended coaxial case is that the magnetic field Green's function in the presence of the pin terminated by a patch, is not known. However, the external capacitance at least for very low frequencies can be modelled as the superposition of two capacitances connected in parallel:

$$C_{ext} = C_{pp} + C_{fringe} \tag{4.3}$$

Here C_{pp} corresponds to a circular parallel plate capacitor between the patch and the ground plane, for which $C_{pp} = \epsilon_0 \epsilon_{sub} \frac{\pi(2c)^2}{4h_{sub}}$ and the associated electric field lines are drawn in green in Fig. 4.4(b). Meanwhile, C_{fringe} corresponds to the external quasi-static capacitance associated to a coaxial opening of inner and outer radii equal to $a = c$ and

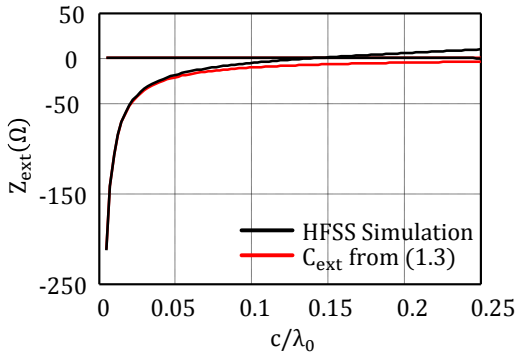

Figure 4.5: The red and the black dashed lines represent the input impedance evaluated using C_{ext} in Eq. 4.3 and the HFSS simulation respectively.

$b = c + h_{sub}$ and the electric field lines are drawn in blue in Fig. 4.4(b). The validation of the approximated formulation in Eq. 4.3 is presented in Fig. 4.5 for dimensions a=1 mm, b=2.3 mm, h_{sub}=1 mm and $\epsilon_1 = \epsilon_2 = 1$.

4.3 Prototype

Sensitivity analysis for increasing distance of the MUT from the coaxial/coaxial based (coaxial line capacitively loaded by a patch) sensors performed via S-parameter measurements are discussed. The sensing elements consists of two single-ended coax fed pin-patch sensors fabricated in printed circuit board (PCB) technology of patch radii 1.5 mm and 2.5 mm respectively, shown in Fig. 4.6(b), and an open ended coaxial probe of inner radius 0.523 mm and outer radius 1.5 mm, in Fig. 4.6(c). A Silicon wafer of 500 μm thickness was used as a MUT layer to perform the sensitivity analysis using the various probes outlined above. The vertical distance between the sensor and the wafer was increased systematically using a motor embedded in the setup with a resolution in the order of few tens of μm.
The pin-patch sensing elements were fabricated in 2 metal layered PCB. The first metal layer served as the ground plane were a coaxial aperture was etched to solder a SMA connector. The circular metal was printed (the second layer) on a dielectric I-Tera MT RF (ϵ_r=3.38 and thickness 0.508 mm).

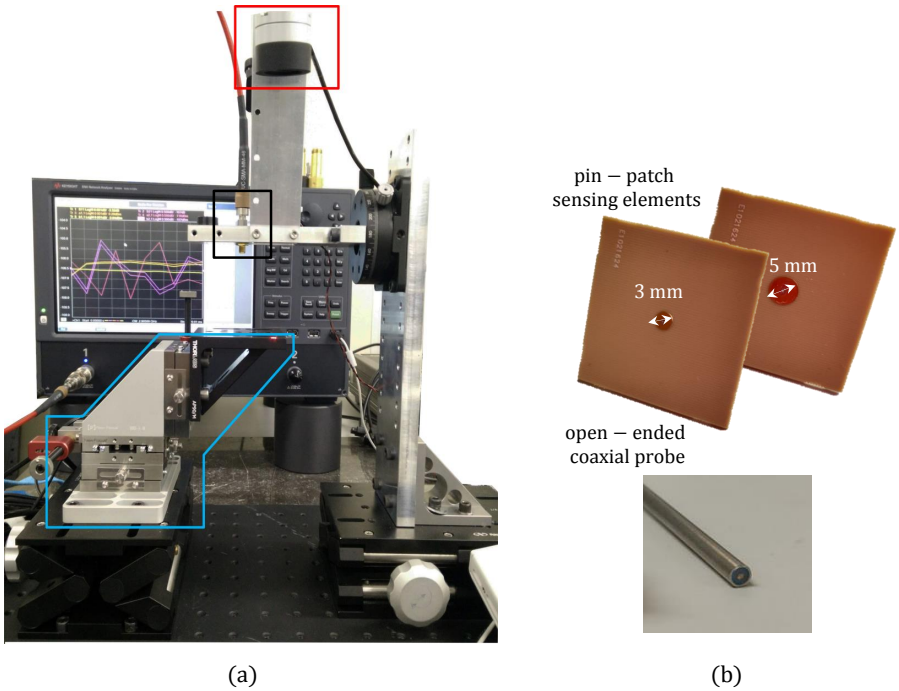

Figure 4.6: (a) Setup for sensitivity measurements. (b) Single ended patch fabricated in PCB technology. (c) A open-ended coaxial probe.

4.3.1 Measurement Setup

The sensitivity measurements of coaxially fed permittivity sensors were performed using the probe station shown in Fig. 4.6(a), at the VSL Dutch Metrology Institute. The left arm, blue highlight in Fig. 4.6(a), employs a a piezo actuator to allow a vertical displacement with μm accuracy. A Keysight PNA is used to perform S11 measurements, after performing a three liquid calibration at the sensor tip.

4.3.2 Calibration

The VNA calibration was performed on the sensing elements to extract the complex permittivity of the MUT at the sensor element reference plane. The calibration process is a mapping of the conventional short-open-load calibration in the liquid environment. The three equations to compute the required error coefficient for a one port calibration (i.e., ed, es and et) are solved by measuring three known liquids, i.e., air, methanol and water. The only known characteristic of the liquid that is employed is the frequency dependent permittivity, computed using nominal Debye coefficients. Using the tool described in this

paper the permittivity of the liquid is translated in the admittance (and converted in reflection coefficient using known formulas) applying the exact dimensions of the coaxial and pin/patch probes. After the calibration coefficients are computed, the VNA can provide the reflection coefficient at the sensor element aperture plane using simple one-port error correction formulas. The reflection coefficient is then translated to admittance, $Y_{meas}(f)$ using $Y_{meas}(f) = (1-\Gamma)/(1+\Gamma)$. For the coaxial cable $Y_{meas}(f)$ is converted into the MUT's average permittivity by minimizing the following cost function:

$$\left| \frac{Y_{meas}(f) - Y_{lookup}(f,\epsilon)}{Y_{meas}(f)} \right| \leq 10^{-3} \tag{4.4}$$

where $Y_{lookup}(f,\epsilon)$ is the admittance surfaces generated for frequencies ranging 5 MHz$\leq f \leq$ 1050 MHz and MUT epsilon 1$\leq \epsilon \leq$40 using Eq. 2.16. Here MUT is assumed to be a homogeneous medium.

However for the pin-patch sensors the admittance surfaces were constructed using an in-house tool based on method of moments, theory outlined in Ch. **??**, yet again with the same constraints as used for the coaxial probe. In order to perform a fair comparison between the average permittivity slopes for the three sensors, the h_{airgap} corresponding to the average epsilon measurement was determined by minimizing the following cost function for all the three probes:

$$\left| \frac{Y_{meas}(f) - Y_{lookup}(f,\epsilon_{air},\epsilon_{Si},h_{airgap})}{Y_{meas}(f)} \right| \leq 10^{-3} \tag{4.5}$$

This time around in generating $Y_{lookup}(f,\epsilon_{air},\epsilon_{Si},h_{airgap})$ the MUT is modelled as a multi-layered medium, the first layer being air of height h_{airgap}, second layer silicon with 500μm

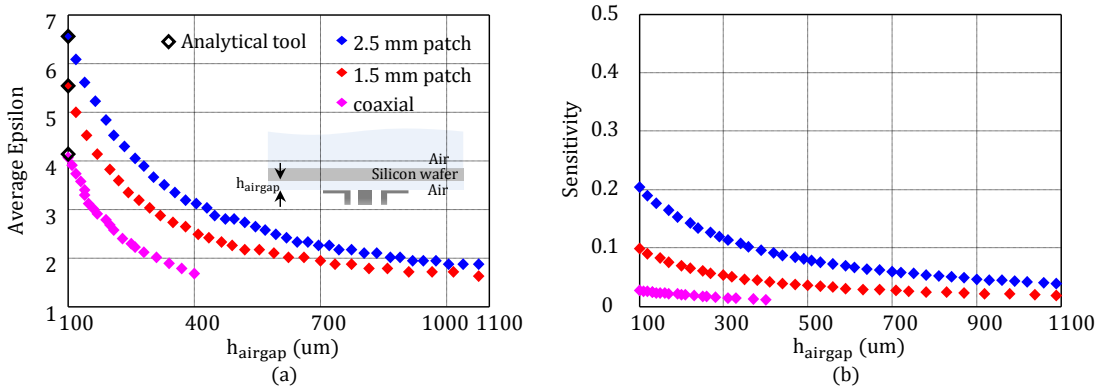

Figure 4.7: Represents the (a) extracted average epsilon using the setup for sensitivity measurements at 405 MHz and (d) Sensitivity versus height of the airgap.

thick, followed by an infinitely extending freespace, for a range of h_{airgap} and frequencies, i.e. 10μm$\leq$ h_{airgap} $\leq$2000μm; and 5 MHz$\leq$ f $\leq$1050 MHz. See Fig. 4.7(a) inset for the MUT stratification.

4.3.3 Measurement Results

The average permittivity of the multilayered media, described in the previous section, extracted using the three permittivity sensors while varying h_{airgap} over a 100 μm to 1.1 mm range is reported in Fig. 4.7(a). In the same figure the average epsilon predicted by the tool, black diamonds, for the stratification shown in the inset of Fig. 4.7(a) for the initial height of 100 μm is also presented. It can be observed from Fig. 4.7(a) that the average epsilon of the coaxial and pin-patch sensors decreases as the sensor-wafer separation increases. Also the average epsilon determined using coaxial tends to approach the freespace value i.e. 1 faster than the other sensors. This highlights a lower detection depth capability of the coaxial compared to the patches. Similar trends can be observed for the patch loaded sensors in the same figure. 1.5 mm radius patch approaches the freespace permittivity faster than the 2.5 mm patch highlighting the enhanced detection depth of the larger patch. Sensitivity's evaluated using (18) is highlighted in Fig. 4.7(b). It is evident from the sensitivity analysis that as the patch radius increases the detection depth also increases for a given sensitivity.

$$S = \frac{C_{meas}(\epsilon_1 = 1, \epsilon_2 = Si, h_{airgap}) - C_{meas}(\epsilon = 1)}{C_{meas}(\epsilon_1 = 1, \epsilon_2 = Si, h_{airgap}) + C_{meas}(\epsilon = 1)} \tag{4.6}$$

where $C_{meas}(\epsilon_1 = 1, \epsilon_2 = Si, h_{airgap}) = \frac{1}{j\omega Z_{meas}(\epsilon_1=1,\epsilon_2=Si,h_{airgap})}$ and $C_{meas}(\epsilon = 1) = \frac{1}{j\omega Z_{meas}(\epsilon=1)}$.

4.4 Conclusions

The sensitivity of the coaxial/ coaxial based sensors to the alterations in the MUT is essentially dependent on the regularized admittance term which becomes a driver for the sensor design. Building on the insight acquired from the sensitivity analysis, guidelines for increasing the detection depth of the sensor are derived: the detection depth of the sensor can be enhanced by realizing a structure equivalent to a larger coaxial cable. This can be achieved by extending the central conductor of the coaxial aperture as a pin and terminating it with a patch in planar technology. This was further validated with sensitivity measurements.

Chapter 5

Analysis of a Single-ended Circular Sensing Element

5.1 Introduction

Design and analysis of a pin-patch sensing element using commercially available electromagnetic solvers would be an extremely time consuming task if the MUT is multilayered and the layers are electrically dense with frequency dependent dielectric properties. Even more if the sensor dimensions are electrically very small, which is the case in integrated technology at microwave frequencies. Moreover when such a sensing element is implemented in CMOS technology along with the back-end read-out circuitry, the thickness of the top metal layer becomes comparable to the substrate thickness there by rendering the simulation of the design in commercial EM solvers very cumbersome. To facilitate the design of such sensing elements, analysis using integral equations is performed in this chapter.

5.2 Single-ended sensing element

The geometry under analysis is a single-ended pin-patch as shown in Fig. 5.1. The circular patch realized on the top metal layer of a multilayered planar technology is fed using a metallic via. The via forms the central conductor of the coaxial aperture etched on the ground plane at $z = 0$ and is extended through the substrate of permittivity ϵ_{sub} and height h_{sub} to feed the patch at the center. As mentioned in the Ch. 2 the coaxial aperture is characterized by an inner conductor of radius a and an outer conductor of radius b, whereas the circular patch has radius c.

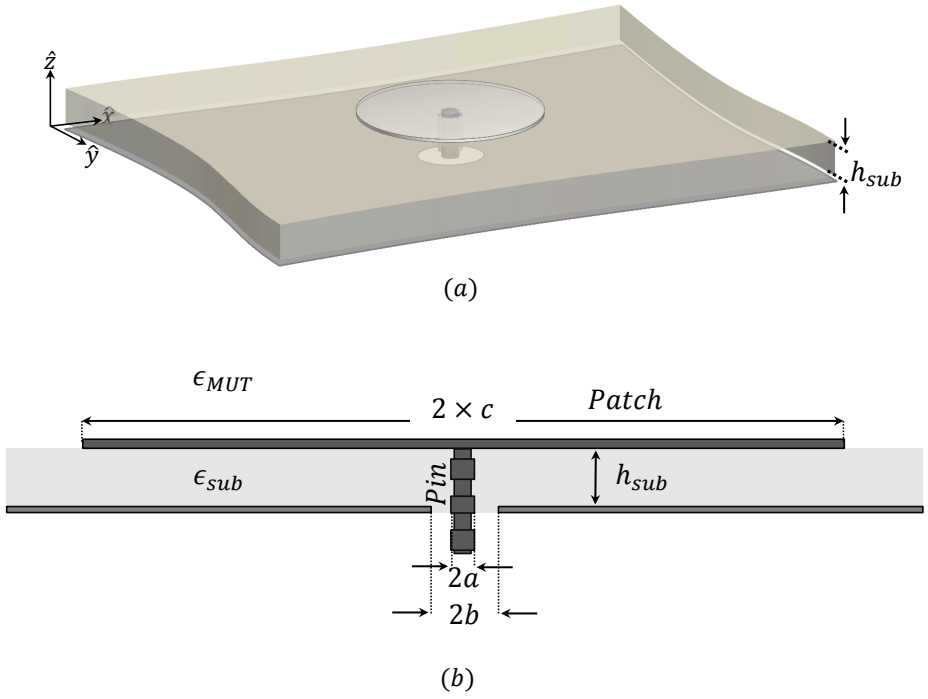

Figure 5.1: Single-ended pin-patch sensing element (a) three dimensional view of the sensor in the presence of a dielectric substrate of thickness h_{sub} and (b) side view of the element highlighting the sensor dimensions.

5.2.1 Integral Equation

As outlined in the Ch. 2 the solution of the fields in the two half-spaces ($z > 0$ and $z < 0$) due to the geometry outlined in Fig. 5.1 can be derived by replacing the slot discontinuity with equivalent magnetic currents. Reiterating, the original problem becomes equivalent to finding fields in the two half-spaces using two separate geometries as shown in Fig. 2.2(c) and (d). However in the current scenario the total magnetic field scattered onto the aperture in the region $z > 0$ will be the superposition of two contributions. The first contribution is attributed to the magnetic currents $\boldsymbol{m_1}(\boldsymbol{r'})$ on the coaxial aperture, whereas the second contribution is due to the equivalent electric currents $\boldsymbol{j}(\boldsymbol{r'})$ distributed on the surface of the pin and the patch, refer Fig. 5.2(b). Subsequently the total admittance can be expressed as

$$Y_{ext}(z=0) = Y_{ext}^{coax}(z=0) + Y_{ext}^{pin+patch}(z=0) \tag{5.1}$$

where $Y_{ext}^{coax}(z=0)$ is the input admittance of the coaxial aperture, that can be evaluated using Eq. 2.16, and $Y_{ext}^{pin+patch}(z=0)$ is the input admittance of the coaxial aperture

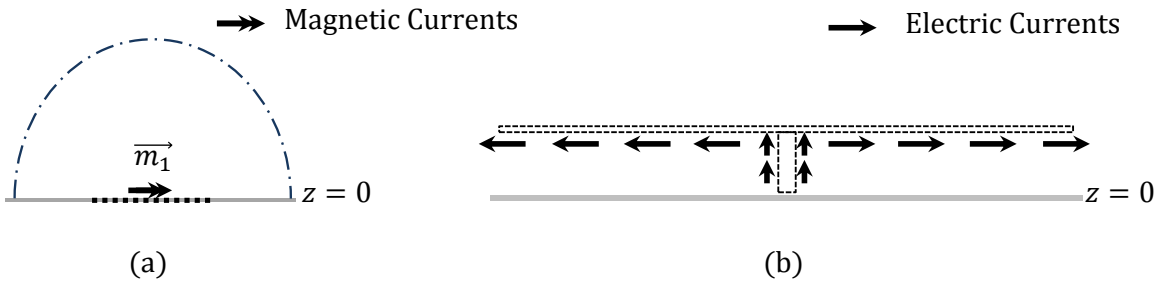

Figure 5.2: (a) Equivalent magnetic currents, $\boldsymbol{m}_1$ distributed on the coaxial aperture at $z = 0$. (b) Equivalent electric currents, $\boldsymbol{j}(\boldsymbol{r'})$ distributed on the surface of the pin and the patch.

loaded with a pin terminated by a patch. Both evaluated in the presence of the MUT. $Y_{ext}^{pin+patch}(z = 0)$ can be expressed using the same definition as in Eq. 2.13, however in this case due to $\boldsymbol{j}(\boldsymbol{r'})$

$$Y_{ext}^{pin+patch}(z = 0) = \frac{\pi}{\ln \frac{b}{a}} \int_a^b h_\phi[\rho, \phi, z = 0; \boldsymbol{j}(\boldsymbol{r'})] d\rho. \tag{5.2}$$

Where $h_\phi[\rho, \phi; \boldsymbol{j}]$ is the magnetic field scattered onto the coaxial aperture due to the equivalent currents $\boldsymbol{j}(\boldsymbol{r'})$ which are further expressed using sub-domain basis functions with unknown weights I_n as follows

$$\boldsymbol{j}(\boldsymbol{r'}) = \sum_{i=1}^{N} I_n \boldsymbol{b_n}(\boldsymbol{r'}). \tag{5.3}$$

The complication however with respect to the open-ended coaxial case is that the magnetic field greens function in the presence of a pin and a patch is unknown. Hence an integral equation for the continuity of the electric field (EFIE) is imposed on the surface of the sensing element to evaluate the weights of the basis function using method of moments, explained in detail in Ch. 6. The currents will then be used in Eq. 5.2 to compute the input admittance.

The magnetic field in Eq. 5.2 can be expressed as a convolution of the basis function $\boldsymbol{j}(\boldsymbol{r'})$ with the appropriate greens function that gives the azimuthal component of the magnetic field from an electric source.

$$h_\phi[\rho, \phi, z = 0] = \iint_{S_{pin+patch}} g_{\phi\lambda}^{hj}(\boldsymbol{r}, \boldsymbol{r'}) \cdot \boldsymbol{j}(\boldsymbol{r}) d\boldsymbol{r'} \tag{5.4}$$

where $S_{pin+patch}$ is the surface on which the basis function is defined and λ is the orientation of the basis functions which in this case is along $\hat{\rho}$ and $\hat{z}$. The explicit expression of the greens function, $g_{\phi z}^{hj}(\boldsymbol{r}, \boldsymbol{r'})$ in the cylindrical domain from [50] is

$$g_{\phi z}^{hj}(\rho, \rho', z, z') = -\frac{j}{2\pi} \int_0^\infty \frac{\zeta k_\rho}{k} I_{TM}^{J_z}(k_\rho; z, z') e^{jk_\rho \rho' \cos(\alpha - \phi')} J_1(k_\rho \rho) k_\rho dk_\rho. \tag{5.5}$$

Where $J_1(k_\rho \rho)$ is the bessel function of the first order, ζ and k the wave impedance and wavenumber in the medium, k_ρ the radial spectral variable, ρ and ρ' the radial distance. $I_{TM}^{J_z}(k_\rho; z, z')$ is the transverse magnetic current flowing in the transmission line equivalent to the dielectric stratification due to a unitary electric source at z'. Likewise the greens function $g_{\phi\rho}^{hj}(\rho, \rho', z, z')$ from [50] is

$$g_{\phi\rho}^{hj}(\rho, \rho', z, z') = \frac{1}{2\pi} \int_0^\infty I_{TM}(k_\rho; z, z') J_1(k_\rho \rho) J_1(k_\rho \rho') k_\rho dk_\rho. \tag{5.6}$$

$I_{TM}(k_\rho; z, z')$ in the above expression is the transverse magnetic current in the equivalent tx-line due to a current source in parallel at z'.

Fig. 5.3 reports the input admittance evaluated at the coaxial aperture using Eq. 5.1 versus frequency for two geometries. Geometry-1 has a total length L, where $L = (2c + h)$, equal to $\lambda_0/4$ at ≈3.6 GHz whereas geometry-2 has a total length L equal to $\lambda_0/557.25$ at 5 GHz. λ_0 is the wavelength in freespace. The dimensions of the sensor along with the dielectric properties of the stratification is outlined in the figure. The tool shows good agreement with Ansoft HFSS simulation results.

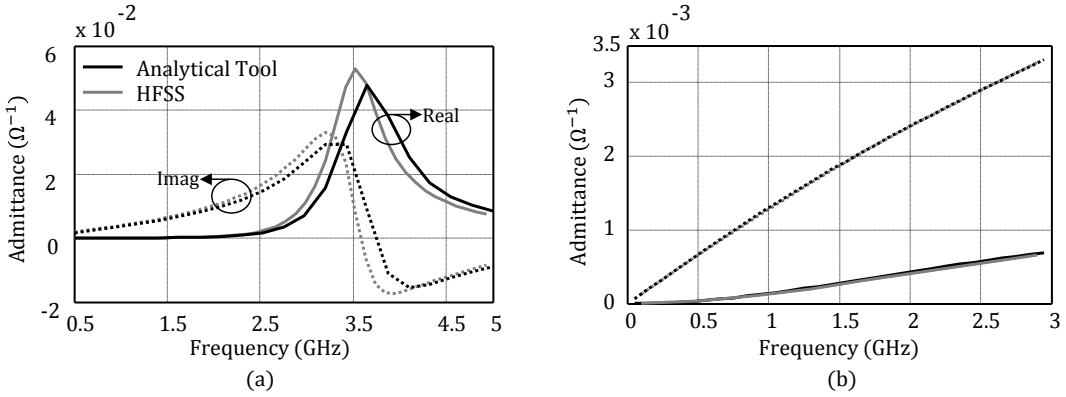

Figure 5.3: Input admittance evaluated at the coaxial aperture using Eq. 5.1 for two geometries: (a) a=1 mm, b=2.3 mm, h=10 mm, c=5 mm in freespace and (b) $a = 2.16\mu m$, $b = 5.5\mu m$, $h = 2.67\mu m$, $c = 52.2\mu m$ with $\epsilon_{sub} = 4$ and $\epsilon_{MUT} = \epsilon_{methanol}$.

5.3 Measurements

In this section, we use the formulation introduced in the previous section to assess the input impedance of various pin-patch sensing elements and subsequently extract the complex permittivity of a known liquid using calibration surfaces that map the measured admittance to a complex permittivity for a given frequency.

5.3.1 Prototype

Pin-patch sensing elements of patch radii 1.5mm, 2.5mm and 5mm were fabricated in printed circuit board technology as shown in Fig. 5.4. The metallic patch was printed on top of a dielectric substrate, RogersRO5003 with permittivity $\epsilon = 3.66$ and having a thickness of 0.523 mm. Plated hole of diameter 0.1 mm was drilled through the dielectric substrate until the top metal layer, feeding the patch at the center. The plated holes were filled with metal later on to have a connection to the connector. The connector was soldered on the bottom layer of the PCB as show in Fig. 5.4. The measurement setup as shown in Fig. 5.4 comprises of a Keysight vector network analyzer, single ended sensor connected to one of the ports via a probe, beaker containing the sample liquid into which the sensor will be immersed and a vertical bench.

5.3.2 Calibration

The VNA calibration was performed on the sensing elements to extract the complex permittivity of the MUT at the sensor element reference plane. The calibration process is a mapping of the conventional short-open-load calibration in the liquid environment. The three equations to compute the required error coefficient for a one port calibration (i.e., ed, es and et) are solved by measuring three known liquids, i.e., air, methanol and water. The only known characteristic of the liquid that is employed is the frequency dependent permittivity, computed using nominal Debye coefficients, [57]. Using the Eq. 5.2 described in this paper the permittivity of the liquid is translated in the admittance (and converted in reflection coefficient using known formulas) applying the exact dimensions of pin/patch probes. After the calibration coefficients are derived, using simple one-port error correction formulas as in [58], the reflection coefficient at the sensor element aperture plane can be evaluated. The reflection coefficient is then translated to admittance, $Y_{meas}(f)$ using $Y_{meas}(f) = (1 - \Gamma)/(1 + \Gamma)$. The unknown permittivity is extracted by minimizing the following cost function:

$$\left| \frac{Y_{meas}(f) - Y_{lookup}(f, \epsilon)}{Y_{meas}(f)} \right| < 10^{-3}. \tag{5.7}$$

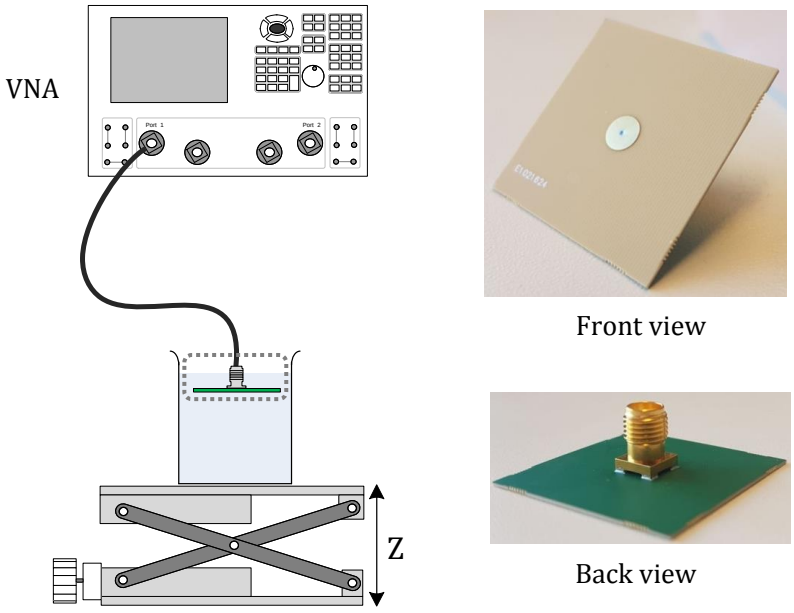

Figure 5.4: Schematic representation of the measurement setup with the front and back view of the sensing element in the inset.

where $Y_{lookup}(f, \epsilon)$ is the admittance surfaces shown in Fig. 5.5, Fig. 5.6 and Fig. 5.7 generated using the analytical tool, Eq. 5.2. The surfaces maps the complex permittivity of the MUT to a complex input admittance at the coaxial aperture for frequency range between 50 MHz to 1050 MHz, ϵ' from 5 to 40 and ϵ'' also from 1 to 40.

5.3.3 Results

Fig. 5.8 reports the extracted complex permittivity of the material under test, ethanol and its error with reference to its cole-cole parameters versus frequency for the three sensing elements. The blue diamond markers denote ϵ' whereas the red diamond markers denote ϵ''. The bold blue and red lines are derived from the cole-cole parameters. It can be observed that the absolute error of the extracted epsilon is well within ± 1 for both the real and the imaginary part of the complex permittivity.

5.4 Conclusions

In this chapter, the integral equation imposed on the coaxial aperture in the previous chapter is further extended by including the contribution of the pin-patch structure terminating the aperture. The additional contribution is evaluated by setting up an electric

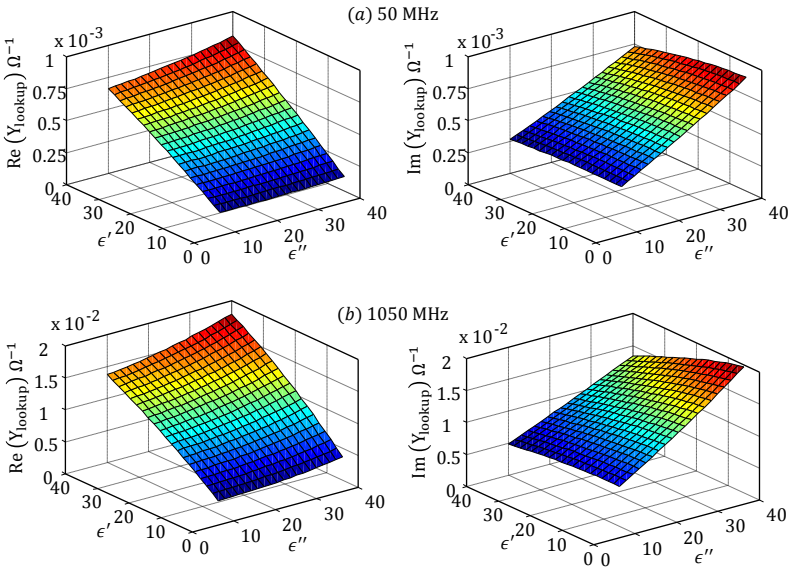

Figure 5.5: Calibration surfaces acquired from the analytical tool versus the real and imaginary part of the MUT epsilon for a patch of radius 1.5 mm at (a) 50 MHz and (b) 1050 MHz.

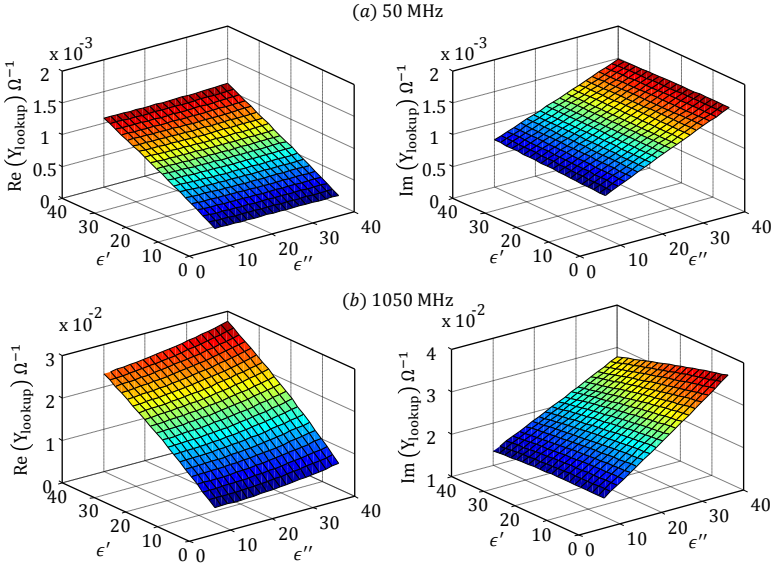

Figure 5.6: Calibration surfaces acquired from the analytical tool versus the real and imaginary part of the MUT epsilon for a patch of radius 2.5 mm at (a) 50 MHz and (b) 1050 MHz.

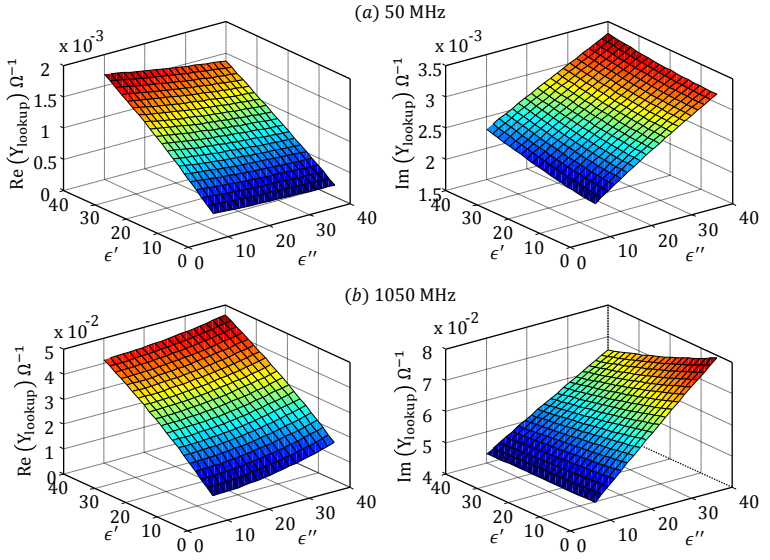

Figure 5.7: Calibration surfaces acquired from the analytical tool versus the real and imaginary part of the MUT epsilon for a patch of radius 5 mm at (a) 50 MHz and (b) 1050 MHz.

field integral equation on the pin-patch structure and estimating the current resorting to small domain method of moments. Furthermore the analytical tool is used in generating calibration surfaces to evaluate the complex permittivity of the material under test from

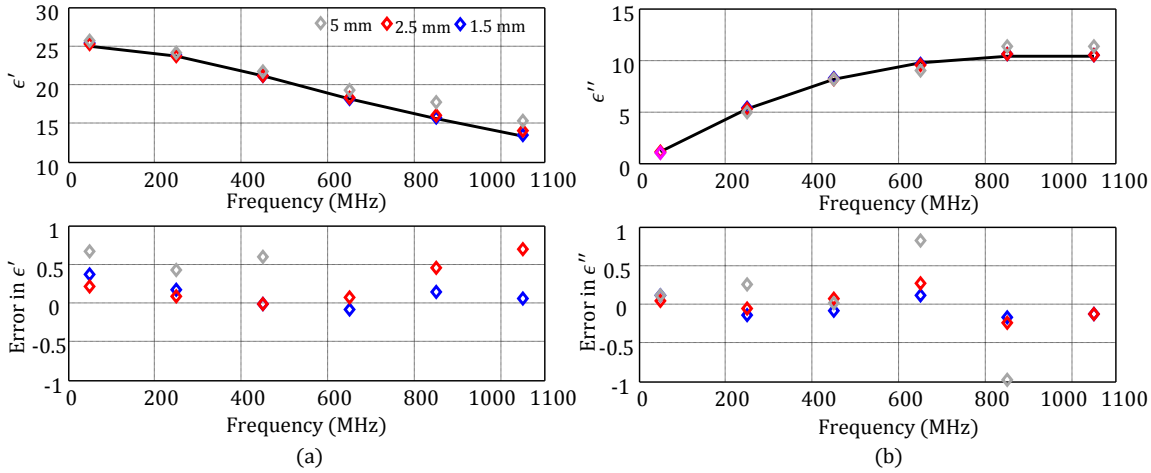

Figure 5.8: Complex permittivity extraction of ethanol versus frequency along with the absolute error with respect to the reference values for (a) 1.5mm (b) 2.5mm and (c) 5mm sensing elements.

Γ measurements. The tool is validated with measurements performed using three sensing elements fabricated in PCB technology of different radii.

Chapter 6

Method of Moments for pin-fed patch in Stratified Media with Reaction Integrals Directly in the Spectral Domain

6.1 Introduction

In this chapter, A detailed procedure to evaluate the reaction integrals for the Method of Moments (MoM) solution of problems containing vertical/ transverse currents in stratified media is discussed.

6.2 Analysis of Patch Loaded Coaxial Sensor

A specific geometry is now addressed, shown in Fig. 6.1, which is similar to the structure discussed in Ch. 5 but with a thick patch metal. Equivalent electric currents, $\boldsymbol{j}$, are distributed on the surface of the pin and the patch. Since these currents are unknown they need to be derived by solving an integral equation for the electric field (EFIE). To this goal, an EFIE is imposed on the surface of the metallic pin and the patch

$$\boldsymbol{e_i}(\boldsymbol{r}) + \boldsymbol{e_s}(\boldsymbol{r}; \boldsymbol{j}) = 0 \tag{6.1}$$

where, $\boldsymbol{e_i}(\boldsymbol{r})$ is the electric field incident in the absence of the pin and the patch, and $\boldsymbol{e_s}(\boldsymbol{r}; \boldsymbol{j})$ is the electric field scattered by the equivalent currents distributed on the pin

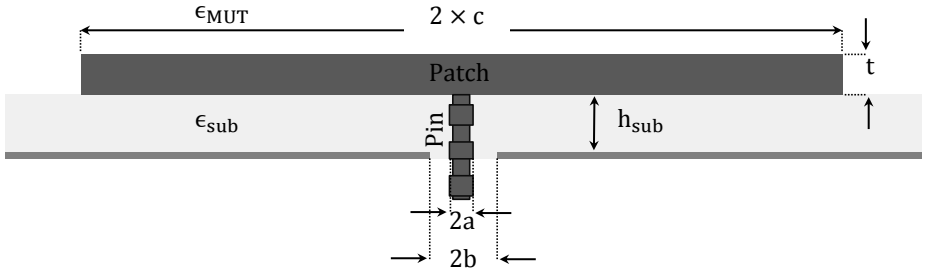

Figure 6.1: Single-ended sensor with a patch metal thickness t.

and the patch. The incidence field $\boldsymbol{e_i(r)}$ in Eq. 6.1 can be assumed to be due to a magnetic frill source defined on the coaxial aperture (at z=0) with voltage V_{coax}. The explicit expressions for the incident electric field along $\hat{\rho}$ and $\hat{z}$ is derived in Appendix A. The equivalent currents $\boldsymbol{j(r')}$ can be further expanded using the following basis functions.

6.2.1 Basis Functions

The electric current $\boldsymbol{j(r')}$ is further expanded using sub-domain basis functions $\boldsymbol{b_p(r')}$, $\boldsymbol{b_a(r')}$ and $\boldsymbol{b_e(r')}$.

1. $\boldsymbol{b_p(r')}$: *Piecewise Linear Functions* (oriented along $\hat{z}$)
   defines the currents on the vertical pin embedded in a substrate of height h_{sub}, refer Fig. 6.2(a).

$$b_p(z',\rho') = \begin{cases} \frac{1}{2\pi a}\left[\frac{1}{\Delta_{pin}}\left(z' + \frac{\Delta_{pin}}{2}\right)\right]\hat{z} & -\frac{\Delta_{pin}}{2} \le z' \le \frac{\Delta_{pin}}{2}; \rho' = a \\ \frac{1}{2\pi a}\left[\frac{1}{\Delta_{pin}}\left(1 - \frac{2|z'|}{\Delta_{pin}}\right)\right]\hat{z} & -\frac{\Delta_{pin}}{2} \le z' \le \frac{\Delta_{pin}}{2}; \rho' = a \end{cases} \tag{6.2}$$

   where Δ_{pin} is the width of the basis function and a the radius of the cylindrical pin.

2. $\boldsymbol{b_a(r')}$: *Attachment Basis Function* (oriented along $\hat{z}$ and $\hat{\rho}$)
   consists of two terms $b_a^{pin}(z',\rho')$ and $b_a^{patch}(z',\rho')$, oriented along $\hat{z}$ and $\hat{\rho}$ respectively, to define the radial and the vertical currents, see Fig. 6.2(b). The two terms ensure the continuity of the currents at the pin-patch junction at $z' = h$ and $\rho' = a$ quote.

$$\boldsymbol{b_a(r')} = b_a^{pin}(z',\rho')\hat{z} + b_a^{patch}(z',\rho')\hat{\rho} \tag{6.3}$$

$$b_a^{pin}(z',\rho') = \frac{1}{2\pi a}\left\{\frac{1}{\Delta_{attach}}\left(z' + \frac{\Delta_{attach}}{2}\right)\right\}\hat{z} \qquad -\frac{\Delta_{attach}}{2} \le z' \le \frac{\Delta_{attach}}{2} \tag{6.4}$$

and

$$b_a^{patch}(z',\rho') = \begin{cases} -\frac{\rho'}{2\pi c^2}\hat{\rho} & 0 \le \rho' \le a; z' = h_{sub} \\ -\frac{\rho'}{2\pi c^2} + \frac{1}{2\pi\rho'}\hat{\rho} & a \le \rho' \le c; z' = h_{sub} \\ 0 & elsewhere \end{cases} \tag{6.5}$$

where, Δ_{attach} is the width of the attachment basis function. $\boldsymbol{b_a}$ was previously introduced in [59] and is the most often used basis function in the study of probe excited planar antennas.

3. $\boldsymbol{b_e}(\boldsymbol{r'})$: *edge basis function* (oriented along $\hat{z}$ and $\hat{\rho}$)
consists of two sub functions namely the bottom edge $b_e^{bottom}(z',\rho')$ and the top edge $b_e^{top}(z',\rho')$ basis function. Each sub function is further composed of two terms oriented along $\hat{z}$ and $\hat{\rho}$ respectively, for e.g. $b_{e,z}^{bottom}$ and $b_{e,\rho}^{bottom}$, see Fig. 6.2(c) and Fig. 6.2(d). The two terms ensure the continuity of the currents at the bending corners in the metallic patch.

$$\boldsymbol{b_e}(\boldsymbol{r'}) = b_e^{bottom}(z',\rho') + b_e^{top}(z',\rho') \tag{6.6}$$

$$b_e^{bottom}(z',\rho') = b_{e,z}^{bottom}(z',\rho')\hat{z} + b_{e,\rho}^{bottom}(z',\rho')\hat{\rho} \tag{6.7}$$

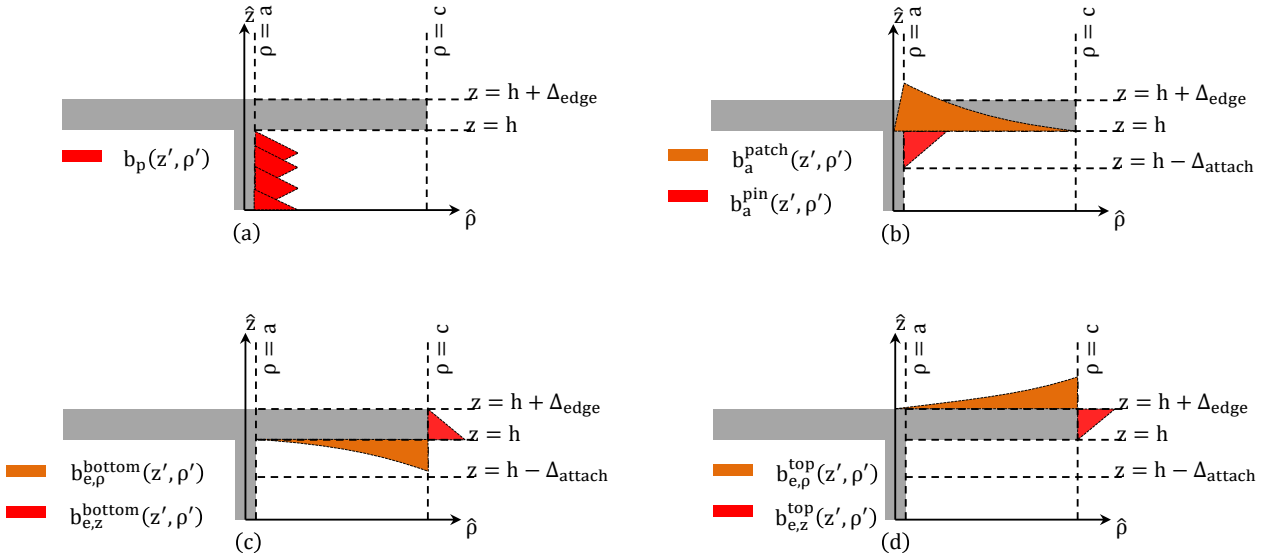

Figure 6.2: Represents the basis functions used in the integral equation. The red and yellow area highlights the profile of the basis functions oriented along $\hat{z}$ and $\hat{\rho}$ respectively. (a) Piecewise linear basis function $b_p(z',\rho')$ (b) Attachment basis function, $b_a(z',\rho')$ (c) Bottom edge basis function, $b_e^{bottom}(z',\rho')$ and (d) Top edge basis function, $b_e^{top}(z',\rho')$.

where

$$b_{e,z}^{bottom}(z',\rho') = \frac{1}{2\pi c}\left\{\frac{1}{\Delta_{edge}}\Big(\frac{\Delta_{edge}}{2} - z'\Big)\right\}\hat{z} \qquad -\frac{\Delta_{edge}}{2} \leq z' \leq \frac{\Delta_{edge}}{2}; \rho' = c \tag{6.8}$$

$$b_{e,\rho}^{bottom}(z',\rho') = \Big(\frac{\rho_1'}{2\pi c^2} - \frac{\rho_2'}{2\pi c^2}\Big)\hat{\rho} \qquad 0 \leq \rho_1' \leq c; 0 \leq \rho_2' \leq a \tag{6.9}$$

Similarly,

$$b_{e,z}^{top}(z',\rho') = \frac{1}{2\pi c}\left\{\frac{1}{\Delta_{edge}}\Big(z' + \frac{\Delta_{edge}}{2}\Big)\right\}\hat{z} \qquad -\frac{\Delta_{edge}}{2} \leq z' \leq \frac{\Delta_{edge}}{2}; \rho' = c \tag{6.10}$$

$$b_{e,\rho}^{top}(z',\rho') = \frac{\rho'}{2\pi c^2}\hat{\rho} \qquad 0 \leq \rho_1' \leq c; z' = h + \Delta_{edge} \tag{6.11}$$

here, Δ_{edge} is the width of the edge basis functions.

6.2.2 Reaction Integrals

In the following subsections the reaction integrals involving vertical and radials currents are derived in-detail using spectral greens functions to account for the dielectric stratification along $\hat{z}$.

Vertical Currents

The spectral representation of the greens function in terms of plane waves is

$$g_{zz}^{ej}(\boldsymbol{r},\boldsymbol{r}') = \frac{1}{4\pi^2}\int_0^{\infty}\int_0^{2\pi} e^{-j\boldsymbol{k_\rho}\cdot(\boldsymbol{\rho}-\boldsymbol{\rho'})} G_{zz}^{ej}(\boldsymbol{k_\rho}; z, z') k_\rho dk_\rho d\alpha \tag{6.12}$$

where

$$G_{zz}^{ej}(k_\rho; z, z') = -\frac{\zeta}{k}\left(\frac{\zeta}{k}k_\rho^2 I_{TM}^{J_z}(k_\rho; z, z') - j\delta(z - z')\right) \tag{6.13}$$

For the case when the source is bounded between dielectrics, as shown in Fig. 6.3, the current $I_{TM}^{J_z}(k_\rho; z, z')$ in the i^{th} section of the transmission line due to a point voltage generator in series at z' is extensively derived in literature [60–65]. The current in the i^{th} section is expressed as a sum of a source term and a secondary term, $Q(z, z')$ that accounts for the reflections at the interfaces as shown

$$I_{TM}^{J_z}(k_\rho; z, z') = \frac{1}{2Z}\Big\{e^{-jk_{zi}|z-z'|} - Q(z, z')\Big\} \tag{6.14}$$

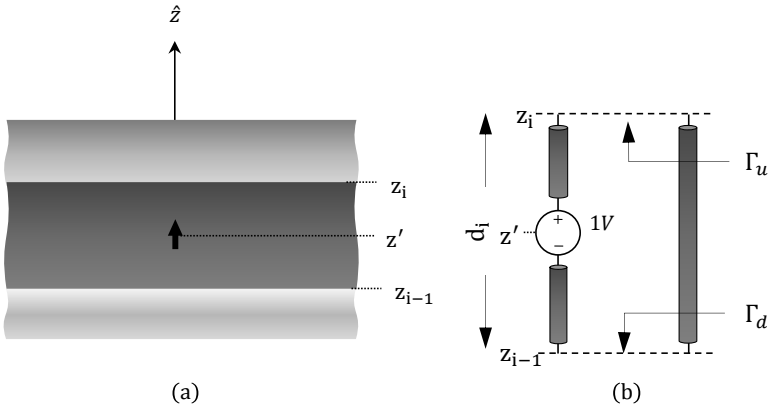

Figure 6.3: $\hat{z}$ oriented electric source placed in a grounded dielectric of permittivity ϵ_s and height h . (a) Cross sectional view. (b) Equivalent z-transmission lines.

where

$$Q(z,z') = \frac{1}{1-\Gamma_u\Gamma_d e^{-2jk_{zi}d_i}}\Big(\Gamma_u e^{-jk_{zi}[(z+z')-2z_i]} + \Gamma_d e^{-jk_{zi}[2z_{i-1}-(z+z')]} + \tag{6.15}$$

$$2\Gamma_u\Gamma_d e^{-2jk_{zi}d_i}\cos[k_{zi}(z-z')]\Big). \tag{6.16}$$

where $\Gamma_u = \frac{Z_{i+1}-Z_i}{Z_{i+1}-Z_i}$ and $\Gamma_d = \frac{Z_{i-1}-Z_i}{Z_{i-1}-Z_i}$. Rewriting Eq. 6.17 as a sum of discontinuous term (source term) and a continuous term (secondary term).

$$I^{J_z}_{TM}(k_\rho;z,z') = I^{cont}_{TM}(k_\rho;z,z') + I^{disc}_{TM}(k_\rho;z,z') \tag{6.17}$$

where

$$I^{cont}_{TM}(k_\rho;z,z') = Q(z,z') \tag{6.18}$$

and

$$I^{disc}_{TM}(k_\rho;z,z') = \frac{1}{2Z}e^{-jk_{zi}|z-z'|}. \tag{6.19}$$

However one can identify Eq. 6.19 as the freespace greens function. Subsequently the reaction Z_{zz} can be expressed as

$$Z_{zz} = -\frac{\zeta}{k}\frac{1}{4\pi}\int_{-\infty}^{\infty}\frac{\zeta}{k}\Big\{F^{cont}(k_\rho) + F^{disc}(k_\rho)\Big\}J_0(k_\rho\rho')H_0^2(k_\rho\rho)k_\rho^3 dk_\rho \tag{6.20}$$

where

$$F^{cont}(k_\rho) = \int_z\int_{z'} I^{cont}_{TM}(k_\rho;z,z')f_b(z')f_t(z)dz'dz \tag{6.21}$$

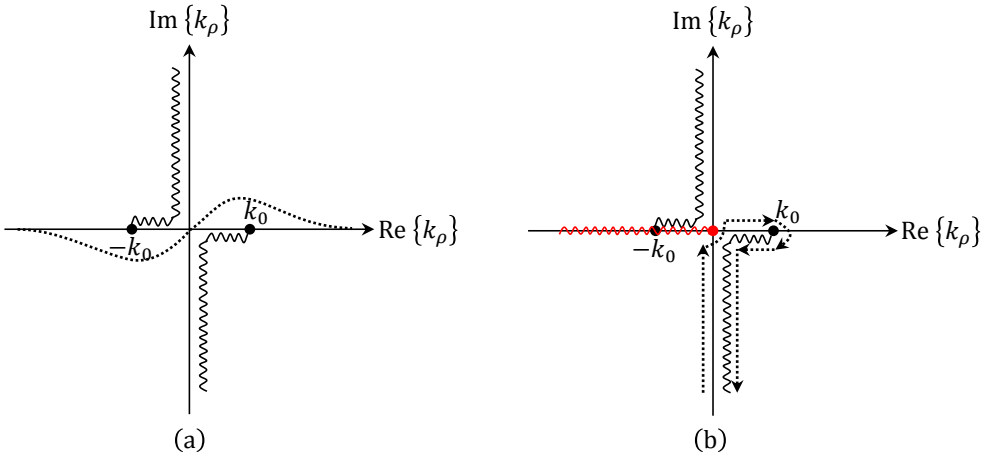

Figure 6.4: Singularities on a k_ρ plane. (a) The dotted black line is the integration path along the real axis. (b) The red lines represent the hankel functions singularities. The dotted black line is the integration path.

and

$$F^{disc}(k_\rho) = \int_z \int_{z'} I_{TM}^{disc}(k_\rho; z, z') f_b(z') f_t(z) dz' dz \tag{6.22}$$

In Eq. 6.20 the integrations in α,ϕ and ϕ' are performed analytically in view of the azimuthal symmetry of the basis and test functions. The integrations in Eq. 6.21 can be expressed directly as products of the fourier transform of the basis and test functions along $\hat{z}$. The integration in k_ρ can be performed along the path in Fig. 6.4(b) surrounding the branch, since the original integration is first extended to an integration from $-\infty$ to ∞ transformed in the path in Fig. 6.4(a), and then deformed.
The integrations in Eq. 6.22 can be performed using the procedure outlined in Appendix B.

Vertical and Transverse Currents

In this section the evaluation of the reaction between the vertical and transverse currents using the Green's function in the spectral domain derived from the projection of rectangular greens functions in the cylindrical co-ordinates is reported.

- ***Green's Function:*** Spatial cylindrical greens function $g_{\rho z}^{ej}(\boldsymbol{r}, \boldsymbol{r}')$ can be expressed in terms of the rectangular greens functions $g_{xz}^{ej}(\boldsymbol{r}, \boldsymbol{r}')$ and $g_{yz}^{ej}(\boldsymbol{r}, \boldsymbol{r}')$ as

$$g_{\rho z}^{ej}(\boldsymbol{r}, \boldsymbol{r}') = g_{xz}^{ej}(\boldsymbol{r}, \boldsymbol{r}') \cos\phi + g_{yz}^{ej}(\boldsymbol{r}, \boldsymbol{r}') \sin\phi \tag{6.23}$$

where

$$g_{\lambda z}^{ej}(\boldsymbol{r},\boldsymbol{r'}) = \frac{1}{(2\pi)^2}\int_0^{2\pi}\int_0^{\infty} G_{\lambda z}^{ej}(k_\rho,\alpha;z,z')e^{-jk_\rho\rho\cos(\alpha-\phi)}e^{-jk_\rho\rho'\cos(\alpha-\phi')}k_\rho dk_\rho d\alpha \quad (6.24)$$

and $\lambda \in (x,y)$. While the spectral components are known to be $G_{xz}^{ej}(k_\rho,\alpha;z,z') = \frac{\zeta k_\rho\cos\alpha}{k}V_{TM}^{Jz}(k_\rho;z,z')$ and $G_{yz}^{ej}(k_\rho,\alpha;z,z') = \frac{\zeta k_\rho\sin\alpha}{k}V_{TM}^{Jz}(k_\rho;z,z')$. Moreover $V_{TM}^{Jz}(k_\rho;z,z')$ is the transverse magnetic voltage at z in the tx-line equivalent to the dielectric stratification with voltage source in series at z'. Substituting the spectral Green's functions discussed above we obtain

$$g_{\lambda z}^{ej}(\boldsymbol{r},\boldsymbol{r'}) = \frac{1}{(2\pi)^2}\int_0^{2\pi}\frac{\zeta k_\rho}{k}V_{TM}^{Jz}(k_\rho;z,z')e^{-jk_\rho\rho'\cos(\alpha-\phi')}I_\lambda(\rho;k_\rho,\phi)k_\rho dk_\rho d\alpha \quad (6.25)$$

where

$$I_x(\rho;k_\rho,\phi) = \int_0^{2\pi}\cos\alpha e^{-jk_\rho\rho\cos(\alpha-\phi)}d\alpha \quad (6.26)$$

$$I_y(\rho;k_\rho,\phi) = \int_0^{2\pi}\sin\alpha e^{-jk_\rho\rho\cos(\alpha-\phi)}d\alpha. \quad (6.27)$$

Using the identity in [add reference], the integral in α can be evaluated analytically as

$$I_x(\rho;k_\rho,\phi) = \frac{2\pi}{j}\cos\phi J_1(k_\rho\rho) \quad (6.28)$$

$$I_y(\rho;k_\rho,\phi) = \frac{2\pi}{j}\sin\phi J_1(k_\rho\rho) \quad (6.29)$$

Substituting Eq. 6.25 in Eq. 6.23 the spatial Green's function $g_{\rho z}^{ej}(\boldsymbol{r},\boldsymbol{r'})$ can be written compactly as

$$g_{\rho z}^{ej}(\boldsymbol{r},\boldsymbol{r'}) = -\frac{j}{2\pi}\int_0^{2\pi}\frac{\zeta k_\rho}{k}V_{TM}^{Jz}(k_\rho;z,z')e^{-jk_\rho\rho'\cos(\alpha-\phi')}J_1(k_\rho\rho)k_\rho dk_\rho. \quad (6.30)$$

- ***Mutual Impedance:*** The general representation of the mutual impedance $Z_{\rho z}$ is

$$Z_{\rho z} = \iint_{S_t}\iint_{S_b} g_{\rho z}^{ej}(\boldsymbol{r},\boldsymbol{r'})f_{bz}(\boldsymbol{r'})f_{t\rho}(\boldsymbol{r})d\boldsymbol{r'}d\boldsymbol{r} \quad (6.31)$$

where $f_{bz}(\boldsymbol{r}'), f_{t\rho}(\boldsymbol{r})$ denote a $\hat{z}$ basis function and $\hat{\rho}$ test function respectively. Expressing the integrals explicitly

$$Z_{\rho z} = \frac{1}{2\pi}\int_{\rho}\int_{\Delta}\Big[\int_0^{2\pi}\int_0^{2\pi} g_{\rho z}^{ej}(\boldsymbol{r},\boldsymbol{r}')d\phi d\phi'\Big] f_{\rho}(\rho)f_z(z)dz\rho d\rho. \tag{6.32}$$

Identifying the integrals in ϕ and ϕ' to be $\int_0^{2\pi} e^{-jk_\rho\rho'\cos(\alpha-\phi')}d\phi' = 2\pi J_0(k_\rho\rho')$ and $\int_0^{2\pi} d\phi = 2\pi$. The reaction integral becomes

$$Z_{\rho z} = -j\int_{\rho}\int_{z'}\left\{\int_0^{\infty}\frac{\zeta k_\rho}{k}V_{TM}^{J_z}(k_\rho;z,z')J_1(k_\rho\rho)J_0(k_\rho\rho')k_\rho dk_\rho\right\} j_z(z')j_\rho(\rho)dz'\rho d\rho \tag{6.33}$$

Moreover $\int_\rho j_\rho(\rho)J_1(k_\rho\rho)\rho d\rho = T_\rho(k_\rho)$, is the hankel transform of the basis function along ρ. Finally the mutual impedance can be expressed as

$$Z_{\rho z} = -j\frac{\zeta}{k}\int_{z'}\left\{\int_0^{\infty}V_{TM}^{J_z}(k_\rho;z,z')J_0(k_\rho\rho')T_\rho(k_\rho)k_\rho^2 dk_\rho\right\} j_z(z')dz'. \tag{6.34}$$

The integration domain in k_ρ is further extended from $-\infty$ to ∞ by transforming a bessel function to an hankel function to ensure faster convergence.

Transverse Currents

The spatial cylindrical greens function that gives a radial electric field from a radial electric current and is azimuth symmetric is known from [50] to be

$$g_{\rho\rho}^{ej}(\boldsymbol{r},\boldsymbol{r}') = \frac{1}{2\pi}\int_0^{\infty}\frac{1}{k_\rho}V_{TM}^{J_\rho}(k_\rho;z,z')\frac{\partial}{\partial\rho'}J_0(k_\rho\rho')\frac{\partial}{\partial\rho}J_0(k_\rho\rho)dk_\rho \tag{6.35}$$

and the impedance $Z_{\rho\rho}$ can be expressed as

$$Z_{\rho\rho} = \iint_{S_t}\iint_{S_b} g_{\rho\rho}^{ej}(\boldsymbol{r},\boldsymbol{r}')f_{b\rho}(\boldsymbol{r}')f_{t\rho}(\boldsymbol{r})d\boldsymbol{r}'d\boldsymbol{r}. \tag{6.36}$$

Substituting Eq. 6.35 in Eq. 6.36 and evaluating the integrals in ϕ and ϕ' analytically results in the impedance being expressed as

$$Z_{\rho\rho} = 2\pi\int_{\rho}\int_{\rho'}\left\{\int_0^{\infty}V_{TM}^{J_\rho}(k_\rho;z,z')J_1(k_\rho\rho')J_1(k_\rho\rho)k_\rho dk_\rho\right\} j_\rho(\rho')j_\rho(\rho)\rho' d\rho'\rho d\rho. \tag{6.37}$$

$V_{TM}^{J_\rho}(k_\rho;z,z')$ is the voltage at z in the equivalent transmission line with a current source in parallel at z'. The integrals in ρ and ρ' can be identified as the hankel transforms as explained in the previous section.

$$Z_{\rho\rho} = 2\pi\int_0^{\infty}V_{TM}^{J_\rho}(k_\rho;z,z')T_\rho(k_\rho)T_\rho(k_\rho)k_\rho dk_\rho. \tag{6.38}$$

6.3 Conclusions

In this chapter, a detailed procedure to evaluate the reaction integrals including vertical currents in the Method of Moments for stratified media is presented. The procedure resorts to evaluating analytically the Fourier Transforms of the basis and test functions, and then performing the reactions entirely in the spectral domain. The basis and test functions can be factorized as products of radial functions and circular harmonics. Accordingly all the reaction integrals resulted in single folded ones. In a general case, the spectral integrals remain double in k_ρ and α. When compared with the simple spatial integrations of the relevant electric field Green's function along the vertical axis procedure, the present procedure is numerically very convenient for comparable accuracies.

Chapter 7

Equivalent Circuit Modelling of a Single-ended Patch Sensing Element

7.1 Introduction

In this chapter, we derive an equivalent circuit for the single-ended patch sensing element, shown in Fig. 5.1, embedded in a RF driven impedance bridge and radiating into a stratified MUT. For the lowest frequency regimes of operation, the pin+patch ensemble can be modelled as a simple parallel plate capacitor, however, as the frequency becomes higher the quasi-static capacitive model becomes inaccurate as the simple parallel plate capacitance model doesnt account for the fringing fields due to the finiteness of the patch. To extend the usage of the sensor over a wide frequency regime we propose to model the patch along with the ground plane as a parallel plate waveguide (PPW) with a frequency dependent transformer to describe the coupling from the coaxial aperture opening to the PPW. Similar models were previously proposed to represent the coupling between a slot and a patch in a stripline/ microstrip fed aperture-coupled patch antennas [66,67]. Specifically, coaxially fed patches have been investigated by Prof. Vandenbosch et. al in the 90's resorting to cylindrical field modal representations. In particular in [68] the geometry was artificially divided in two domains, so that the fields in each one of these two domains could be represented separately as a superposition of coaxial type of modes. The continuity of the electric and magnetic fields across the auxiliary boundary was then imposed to obtain the exact values of the coefficients of the modes describing the complete field in the waves guides. In [69] it was shown that most of these calculations could be performed analytically which gave a significant boost to the computational efficiency of the numerical procedure. When more specifically comparing the equivalent networks in the works [68–71] with the

results presented in Ch. 7, it is apparent that the numerical computation for the transition parameters is probably equivalent. In the cases in [68] the reaction integrals were approximated analytically, while the expression for the admittance in this work needs to be calculated numerically. However, with our procedure coming 30 years after the evaluation of the integral with Matlab is really not a problem. The advantage of our procedure, in our view is that the equivalent transmission line representation of the patch, and the connection to the coaxial cable by means of a capacitance and a transformer is extremely intuitive.
The relative impact of the MUT and the metal thickness is accurately included in the evaluation of the end point load of the transmission line. This load is evaluated resorting to an in-house tool based on a Method of Moments (MoM) procedure in the spectral domain, refer Ch. 6. The model is validated with the results obtained by performing full wave simulations via a commercial tool based on FDTD. The model is further used for detecting permittivity variations in an MUT using a CMOS permittivity sensor matrix in [72]. The matrix consists of 25 elements that are arranged in a 5x5 rectangular matrix.

7.2 Analysis

Geometry under investigation is a patch loaded coaxial sensor schematized in Fig. 5.1. The admittance Y at the coaxial aperture can be evaluated as the following reaction integral

$$Y(z=0) = \int\limits_{S_{coax}} \boldsymbol{h}(\boldsymbol{r}_t; V=1) \cdot \boldsymbol{h}_b(\boldsymbol{r}_t) d\boldsymbol{r}_t \tag{7.1}$$

where $\boldsymbol{h}(\boldsymbol{r}_t; V=1)$ is the magnetic field generated by the unitary voltage electric field distribution which can be further expressed as the radiation integral due to the magnetic current $\boldsymbol{m}_2$ and $\boldsymbol{h}_b(\boldsymbol{r}_t)$ is the model magnetic field distribution with an azimuthal profile $\frac{1}{2\pi\rho}\hat{\phi}$.

7.2.1 The Infinite PPW Model

Let us begin the analysis of the admittance by focusing on the auxiliary problem of an infinitely extending patch that results in a parallel plate waveguide (PPW) formed between the patch and the ground plane, refer Fig. 7.1(a). Hence $\boldsymbol{h}$ in Eq. 7.1 is replaced by $\boldsymbol{h}_{ppw}$ to highlight the evaluation of the magnetic field in the presence of an infinitely extend-

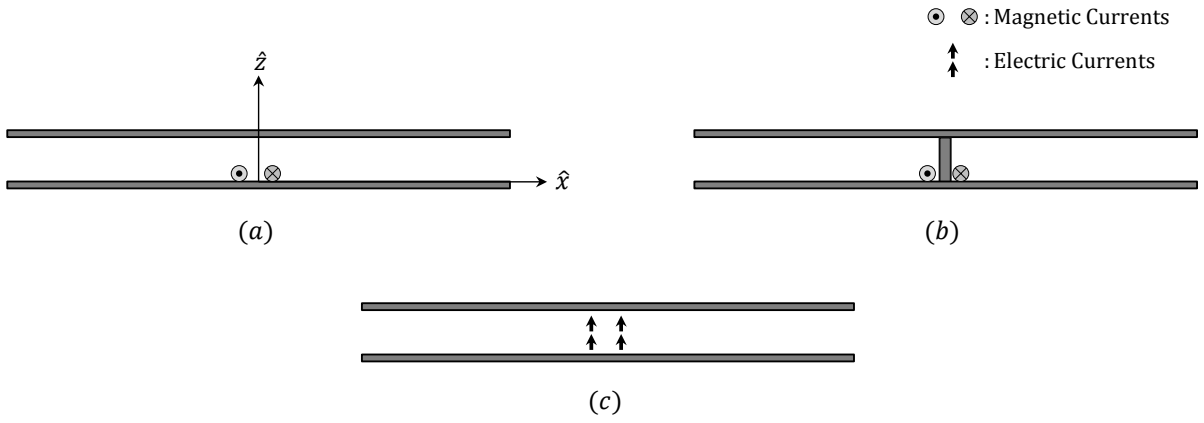

Figure 7.1: Green's function of the single-ended pin patch structure. (a) Magnetic current radiating in a PPW structure formed between the infinitely extending patch and ground plane. (b) Magnetic current radiating in the presence of a pin in a PPW. (c) Pin equivalent electric currents radiating in a PPW.

ing PPW. Formalizing the problem in Fig. 7.1(a) by means of equivalence theorem, the magnetic field in Eq. 7.1 can be expressed as a superposition of two separate contributions

$$\boldsymbol{h}(\boldsymbol{r}_t) = h_\phi(\boldsymbol{r}_t)\hat{\phi} = h_{coax}^{ppw}(\boldsymbol{r}_t)\hat{\phi} + h_{coax}^{ppw+pin}(\boldsymbol{r}_t)\hat{\phi}. \tag{7.2}$$

The first term $h_{coax}^{ppw}(\boldsymbol{r}_t)\hat{\phi} = [g_{hm}^{ppw} \cdot \boldsymbol{m}_b(\boldsymbol{r}_t)]\hat{\phi}$, is the azimuthal magnetic field radiated by the magnetic current, $\boldsymbol{m}_b(\boldsymbol{r}_t)$ in the presence of an infinitely extended PPW but in absence of a pin, refer Fig. 7.1(a). This term can be evaluated using the stratified media dyadic Green's function that relates the magnetic currents to a magnetic field. The second term $h_{coax}^{ppw+pin}(\boldsymbol{r}_t)\hat{\phi} = [g_{hm}^{ppw+pin} \cdot \boldsymbol{m}_b(\boldsymbol{r}_t)]\hat{\phi}$ is the azimuthal magnetic field scattered onto the same aperture by equivalent electric currents, $j_{pin}(\boldsymbol{r}_t)$ distributed on the vertical pin in a PPW configuration, as shown in Fig. 7.1(c). The electric current on the pin is assumed to be uniform and its amplitude is evaluated numerically by setting up a Method of Moments (MoM) procedure to solve the electric field integral equation (EFIE) that imposes the tangential component of the electric field on the pin to be zero. Subsequently Y in Eq. 7.1 can be expressed as a sum of two contributions: Y_{coax}^{ppw} due to $h_{coax}^{ppw}(\boldsymbol{r}_t)\hat{\phi}$ and $Y_{coax}^{ppw+pin}$ due to $h_{coax}^{ppw+pin}(\boldsymbol{r}_t)\hat{\phi}$, as shown in Fig. 7.2.

7.2.2 Transformer from the coaxial line to the PPW

The integral equation on the metallic pin is

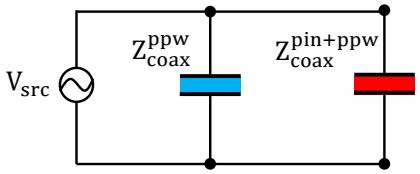

Figure 7.2: The total input admittance of the coaxial line accounting for an infinite PPW line as the parallel of two contributions.

$$e_z^{sc}(z, \rho = a, j_{pin}) = -e_z^i(z, \rho = a; m_\phi). \tag{7.3}$$

The incident electric field $e_z^i(z, \rho = a; m_\phi)$ is generated by a unitary voltage magnetic currents m_ϕ radiating in the presence of a PPW as in Fig. 7.2(a). The scattered field $e_z^{sc}(z, \rho = a, j_{pin})$ is radiated by unknown electric currents j_{pin} equivalent to the pin, again in the presence of a PPW, refer Fig. 7.2(c). The assumption that the current in the pin is constant with respect $\hat{z}$ allows one to obtain a simple expression for the fields. Assuming a surface current distribution on the pin as $j_{pin}(\rho, \phi, z) = \frac{I_{pin}}{2\pi a}\delta(\rho - a)\hat{z}$, where I_{pin} is the net current in the pin and a the radius of the pin the electric field radiated in the PPW along $\hat{z}$ can be expressed as

$$e_z^{sc}(z, \rho = a, j_{pin}) = -\frac{k\zeta}{4} I_{pin} H_0^{(2)}(k|\rho = a|). \tag{7.4}$$

$H_0^{(2)}$ is the Hankel function of zeroth order and second kind, ζ and k are the homogeneous media impedance and wavenumber respectively. Solving the EFIE in Eq. 7.3 using Galerkin's approach results in

$$I_{pin} \int_0^{h_{sub}} e_z^{sc}(z, \rho = a, j_{pin}) dz = -\int_0^{h_{sub}} e_z^i(z, \rho = a; m_\phi) dz. \tag{7.5}$$

Indicating the integral term on the LHS of Eq. 7.5 as pin impedance Z_{ppw}^{∞} and the term on the RHS as an impressed voltage V_{pin} we obtain $Z_{ppw}^{\infty} I_{pin} = V_{pin}$. The impedance Z_{ppw}^{∞} can be evaluated as the input impedance of an infinite radial transmission line at $\rho = a$ using the following

$$Z_{ppw}^{\infty} = -\frac{k\zeta}{4} \int_0^{h_{sub}} H_0^{(2)}(k|\rho = a|)dz. \tag{7.6}$$

The forcing term V_{pin}, being the average electric field due to the magnetic currents on the ground plane, corresponds to retaining only the fundamental mode in a complete expansion in terms of PPW modes [52].

$$V_{pin} = \frac{j}{2} \frac{\pi}{\ln \frac{b}{a}} \left\{ H_0^{(2)}(kb) - H_0^{(2)}(ka) \right\} \tag{7.7}$$

Substituting Eq. 7.7 and Eq. 7.6 in Eq. 7.5 the unknown I_{pin} is

$$I_{pin} = \frac{j}{2} \frac{\pi}{\ln \frac{b}{a}} \frac{H_0^{(2)}(kb) - H_0^{(2)}(ka)}{Z_{ppw}^{\infty}}. \tag{7.8}$$

After having evaluated I_{pin}, $Y_{coax}^{pin+ppw}$ can be expressed as the integration of the magnetic field over the coaxial aperture in $\rho \in [a, b]$ and $z = 0$.

$$Y_{coax}^{pin+ppw} = \iint_{S_{coax}} \boldsymbol{h}_{coax}^{pin+ppw}(\boldsymbol{r}) \cdot \boldsymbol{m}(\boldsymbol{r}) d\boldsymbol{r} \tag{7.9}$$

The magnetic field $\boldsymbol{h}_{coax}^{pin+ppw}(\rho, z = 0)$ due to a vertical current in a parallel plate waveguide is known analytically from [73] to be

$$\boldsymbol{h}_{coax}^{pin+ppw}(\rho, z = 0) = I_{pin} \frac{-jk}{4} H_1^{(2)}(k\rho) \tag{7.10}$$

Accordingly, substituting Eq. 7.10 in Eq. 7.9 and integrating in ρ results in the input impedance of a coax loaded with an infinitely extending patch to be

$$Z_{coax}^{pin+ppw} = \frac{Z_{ppw}^{\infty}}{\frac{j}{2} \frac{\pi}{\ln \frac{b}{a}} \left\{ H_0^{(2)}(kb) - H_0^{(2)}(ka) \right\}} \tag{7.11}$$

From a network perspective the impedance factorization in Eq. 7.11 can be interpreted as a transformer, Fig. 7.3, of turns ratio $n_{SQR} = \frac{j}{2} \frac{\pi}{\ln \frac{b}{a}} \left\{ H_0^{(2)}(kb) - H_0^{(2)}(ka) \right\}$. For small

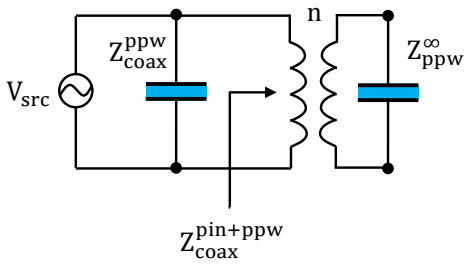

Figure 7.3: Equivalent circuit to evaluate the input admittance of an infinite PPW line as the parallel of two contributions.

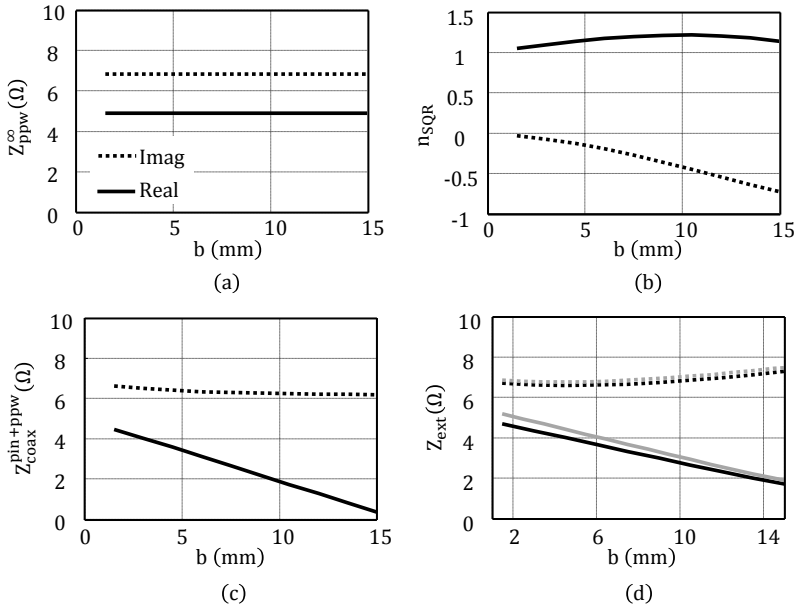

Figure 7.4: Different impedances of the equivalent circuit in Figure 7.3 and turns ration n versus b, the outer radius of the coaxial feed. Grey lines in (d) are obtained from HFSS Ansoft simulations.

dimensions of the coaxial aperture the turns ratio $n_{SQR} \approx 1$ and consequently $Z_{coax}^{pin+ppw} = Z_{ppw}^{\infty}$. For an infinitely extending PPW of height 0.5 mm fed by a pin of radius 1.2 mm Fig. 7.4 represents the variation of the various impedances, highlighted in Fig. 7.3, and the turns ratio versus b. In the same figure the external impedance Z_{ext} is validated with Ansoft HFSS simulation.

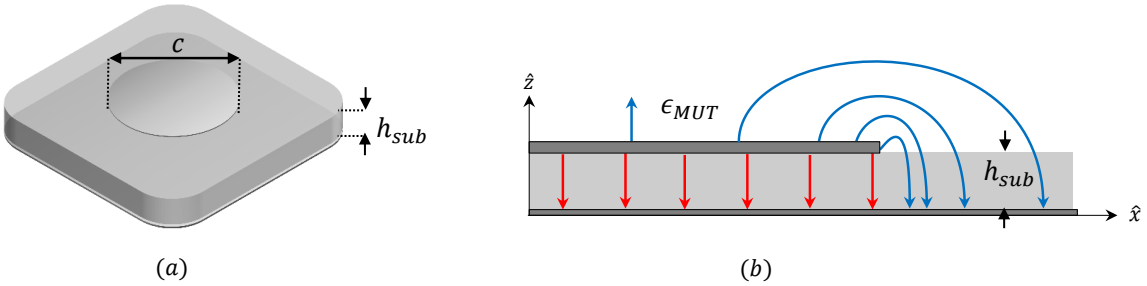

Figure 7.5: (a) Top view of the patch of radius c on the SiO_2 substrate of thickness h_{sub}. (b) Cross section of the PPW line where the red lines represent the electric field lines between the patch and the ground, while the blue lines represent the fringing fields at the end point.

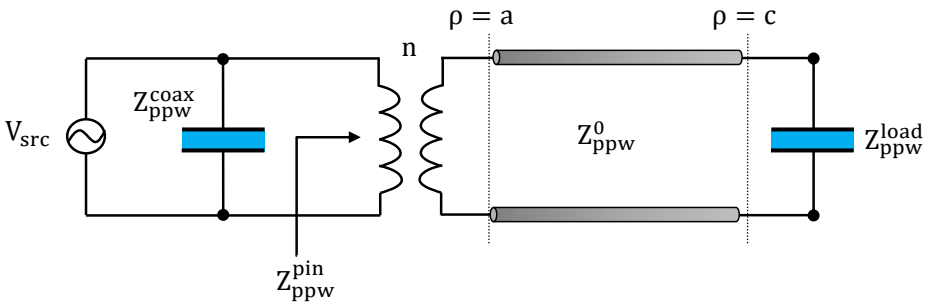

Figure 7.6: Equivalent circuit for the input admittance of a finite radius patch.

7.2.3 Patch as a finite PPW line

The end point of a finite PPW line realized between the patch and the ground plane is shown in Fig. 7.5. Accordingly in the equivalent circuit in Fig. 7.3 Z_{ppw}^{∞} should be replaced by Z_{ppw}^{finite} which also accounts for the loading associated to the fringing fields. Z_{ppw}^{finite} can be represented by a loaded radial PPW line of length c, refer Fig. 7.6. It should be recalled that the characteristic impedance, Z_{ppw}^{0} of a radial line is a function of the radial distance ρ from the centre of the patch. For growing ρ the electric current entering via the pin is spread over a wider surface, whereas the voltage drop is always taken between the patch and the ground plane. As a consequence $Z_{ppw}^{0}(\rho) = \frac{\zeta h_{sub}}{2\pi\rho}$ [52] where ζ is the wave impedance in the substrate media, h_{sub} the height of the substrate. The solution of radial transmission lines is well described in [52] page 43. Thus the problem of evaluating the properties of the entire sensor can be reduced to the problem of estimating the load, Z_{ppw}^{load}, of the finite PPW line. The input impedance of the sensor can be derived resorting to standard cylindrical transmission line theory and the transformer n_{SQR} . An approximate

technique can be used to estimate the load Z_{ppw}^{load} when $\epsilon_{sub} > \epsilon_{MUT}$, whereby the problem in Fig. 7.7(a) was reduced to the evaluation of external admittance of a coaxial probe of internal radius $\rho = c$ and external radius $\rho = c + h_{sub}$, radiating in the presence of planar stratification, Fig. 7.7(b).

Derivation of Z_{ppw}^{load}

When the permittivity of the material under test is significantly higher than the dielectric of the substrate ($\epsilon_{MUT} > \epsilon_{sub}$), the load can no longer be evaluated resorting to the approximation in Fig. 7.7(b). Moreover the procedure in Fig.7.7(b) does not take into account the thickness of the metallic patch. In such scenarios, an in-house tool based on method of moments is used to evaluate the input impedance (equivalent to $Z_{coax}^{pin+ppw}$ in Fig. 7.6) at the aperture of the coaxial cable. The basis functions and the reaction integrals used in the MoM are outlined in Ch. 6. Subsequently using the transformer turns ratio n_{SQR} and the solutions of the radial transmission line, the impedance $Z_{coax}^{pin+ppw}$ is transformed into Z_{ppw}^{load}. In the frequency range where the sensor is purely capacitive, the capacitance associated to the load, $Z_{ppw}^{load} = \frac{1}{j\omega C^{load}(\epsilon)}$ needs to be evaluated only at one frequency using the in-house tool. $C^{load}(\epsilon)$ in Fig. 7.8 is the sum of two contributions $C_{MUT}^{load}(\epsilon)$ and $C_{th}^{load}(\epsilon)$ associated to the MUT and the metal thickness respectively. The frequency range across which the sensor remains purely capacitive depends on the dielectric constant of the MUT, denser the MUT smaller is the frequency range across which the sensor is purely capacitive. This is highlighted in Fig. 7.9 for two different dielectrics of

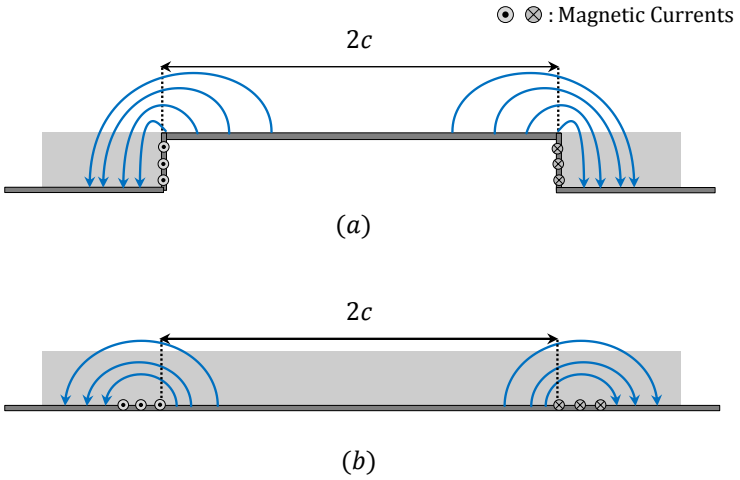

Figure 7.7: Equivalent problems for the open ended PPW line.

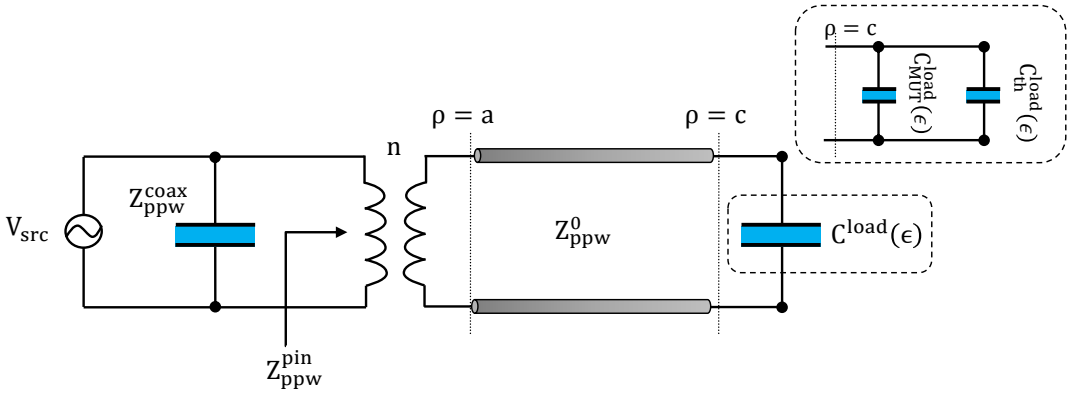

Figure 7.8: Equivalent circuit for the input admittance of a finite radius purely capacitive patch.

the MUT, $\epsilon_{MUT} = 80$ and $\epsilon_{MUT} = 40$, over a frequency band spanning 0.5-100 GHz. In the same figure the total load capacitance in the presence of a finite metal thickness is also presented. As the thickness of the metal becomes larger in terms of wavelength in the MUT, the additional capacitance contribution from the patch thickness also increases. This can qualitative be explained as due to larger currents flowing on the lateral part of the metal with denser MUT's. Fig. 7.10(a) compares the increase in the load capacitance for two thickness ($t = 0.02c$ and $t = 0.05c$) of the patch (grey bold and dotted lines) versus the infinitesimal thin patch (black bold line). This is also true with the patch radius, as the radius of the patch becomes electrically longer the capacitance associated to the load also increases. This is highlighted for two MUT dielectrics, $\epsilon_{MUT} = 40$ (black line) and $\epsilon_{MUT} = 10$ (grey line) in Fig. 7.10(b). With the aprior knowledge of C^{load} at one frequency and the frequency range where the sensor is purely capacitive the input impedance of the sensor across the whole band can be calculated using the transmission line tool in Fig. 7.8 whose load is $C^{load}(\epsilon)$.

7.3 A 5x5 Microwave Permittivity Sensor Matrix in 0.14-μm CMOS

In this section we demonstrate the usage of CMOS microwave permittivity sensor matrix for the localized detection of permittivity variations in a material. The matrix comprises of 25 sensing pixels arranged in a 5x5 rectangular matrix. Top metal patches utilized as sensing pixels are embedded into RF bridges and voltage-to-current conversion readout stages.

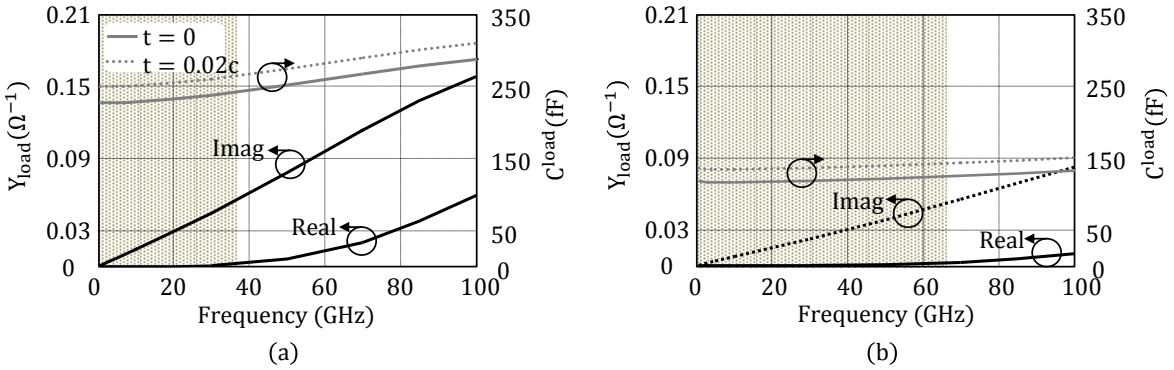

Figure 7.9: $Y^{load}(\Omega^{-1})$ and $C^{load}(fF)$ versus frequency for a sensor of dimensions: c=52.5μm, a=0.02c, b=2.3a, h=0.05c and $\epsilon_{sub} = 4$ (a) $\epsilon_{MUT} = 80$ (b) $\epsilon_{MUT} = 40$. Gray bold and dashed lines represent the load capacitance of the sensor without and with metal thickness, whereas the black bold and dashed lines represent the load admittance $Y^{load}(\Omega^{-1})$.

7.3.1 Matrix Design

The single-ended patch sensing elements are fabricated on the top metal layer in a 6-layer CMOS stack with the passivation layer removed for direct contact with the MUT. The patch sensors permittivity dependent admittance, depending on the real and imaginary part of the MUT permittivity was extracted using the analytical tool. To enable scalability to a larger number of sensing elements, the active detector circuits are integrated below

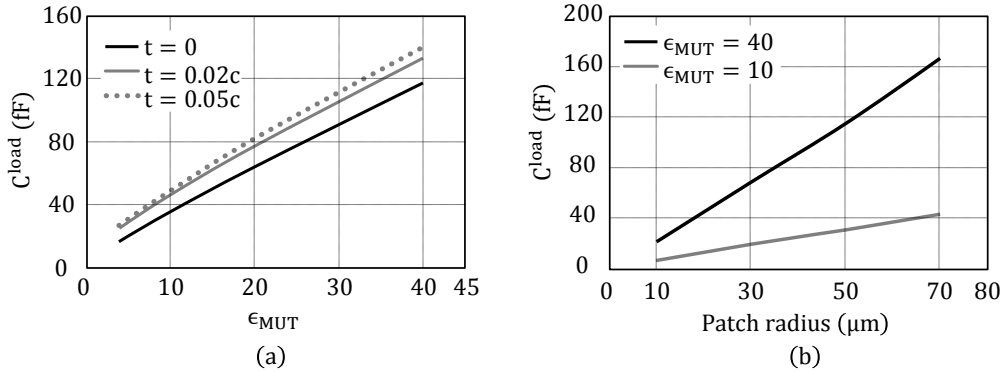

Figure 7.10: (a)$C^{load}(fF)$ versus ϵ_{MUT} at 5GHz for infinitesimal thin patch (black bold line), patch with thickness t=0.02c (grey bold line) and t=0.05c (grey dotted line). Rest of the sensor dimensions as outlined in Fig. 7.9. (b) $C^{load}(fF)$ versus radius of the patch at 5GHz for a sensor with dimensions a=1μm, b=2.3μm, h=3μm, t=3μm and $\epsilon_{sub} = 4$ $\epsilon_{MUT} = 40$ (black line) and $\epsilon_{MUT} = 10$ (grey line).

the patch. Metal 4 is used as a ground plane to isolate the patch from the active circuits. The octagonal shape patch is connected to a metal 3 feed that provides access to the active drive and read circuitry through a vertical stacked via connection.

7.3.2 Matrix Read-out

As outlined in [72], each patch sensor is connected to a double-balanced Wheatstone bridge, using a local clipping RF driver buffer, to provide fundamental and harmonic output voltage dependent on the patch load YL. Differential readout is performed by means of a dummy bridge to cancel common-mode signals. As a result, the output voltage of the bridge is directly linked to the permittivity of the material interfaced to the patch. The bridge branches contain reconfigurable admittance YB, in the form of 4-bit binary switched capacitor control, in order to allow dynamic tuning of the bridge to the patch admittances (YL≈YB). Under this condition, the bridge achieves the highest sensitivity to its load, hence permittivity, variations. This flexibility allows to vary the sensitive point of the bridge depending on the MUT's properties.

7.3.3 Experimental Results

To validate the proposed architecture, the permittivity sensor was designed and fabricated in 140-nm CMOS technology. The chip size is 2.5×2.3 mm^2, with the effective sensor area

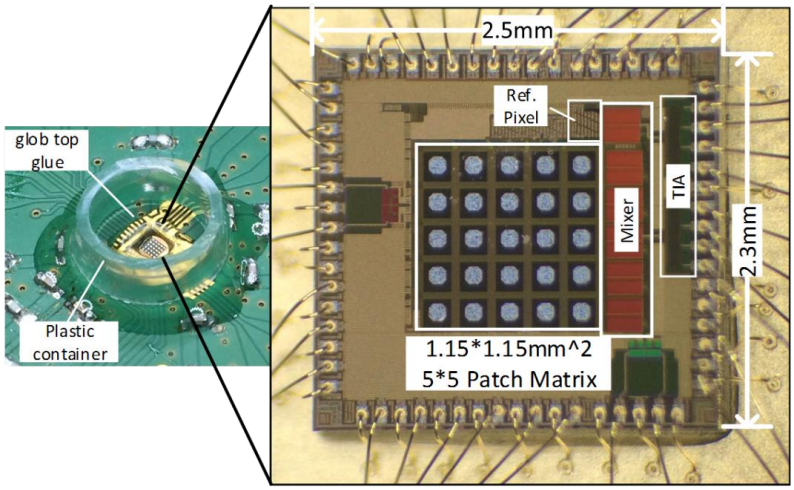

Figure 7.11: Photograph of prototype chip assembling and chip micrograph.

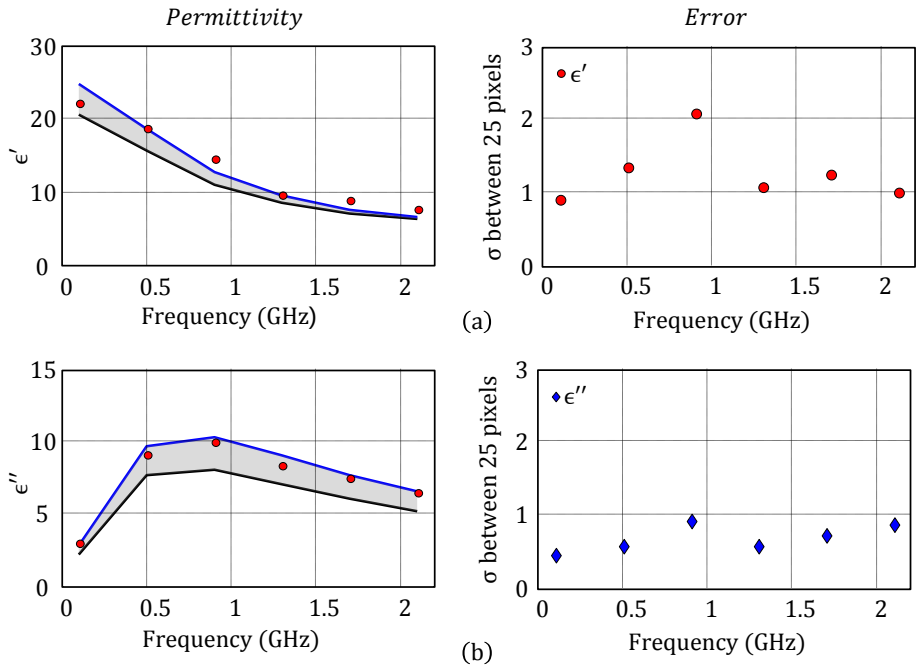

Figure 7.12: Measured permittivity of ethanol (red dots) versus frequency. Blue and black lines are the permittivity of ethanol using cole-cole parameters at 20° and 50° respectively. (a) and (b) represent the real and the imaginary part of the measured permittivity along with the standard deviation between the 25 pixels.

of 1.15×1.15 mm^2. Together with a small container, the chip was mounted on a PCB for liquid measurements (see Fig. 7.11), while the bonding wires were isolated from the MUT using a glob top packaging method. Six materials (de-ionized water, methanol, ethanol, 2-propanol, 1-butanol and air) are employed for complex permittivity measurement. To calibrate every pixel of the sensor matrix for absolute permittivity versus frequency, five of the aforementioned materials were employed. Based on the linear equation and the known permittivity of five calibration materials, the expected YL of the patch versus permittivity were firstly estimated. Then, the offset value and coefficient of the permittivity-to-Vout relation were calculated by fitting the measured bridge output to a least square (LS) approximation algorithm. Fig. 7.12(a) and (b) show the average measured complex permittivity of ethanol versus frequency. Fig. 7.13 shows the permittivity imaging result of a drop of oil inside propanol (ϵ' contrast: 7.4 to 3), with a scan rate of 4 image/s, demonstrating a clear permittivity detection function. The 3D permittivity surface clearly highlights the capability of the matrix sensor to resolve a sub-mm discontinuity.

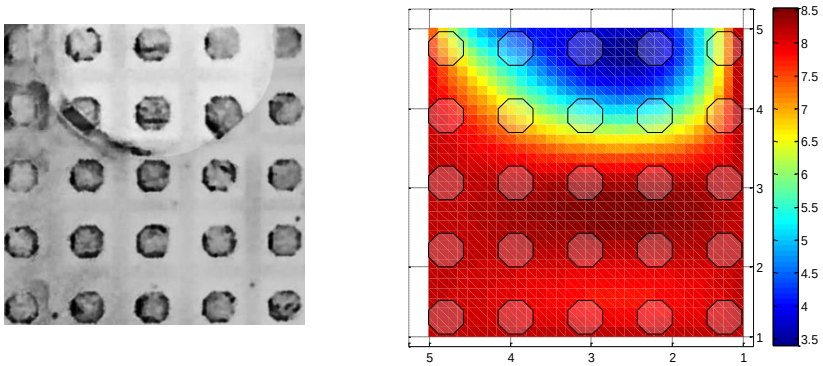

(a) (b)

Figure 7.13: (a) Permittivity contrast across the various pixels at 900MHz. (b) Micrograph of the chip highlighting the oil droplet immersed in propanol.

7.4 Conclusion

In this chapter, a fast and efficient equivalent radial transmission line tool was outlined to accurately evaluate the input impedance of a single-ended patch sensing element realized in planar technology. The procedure provides a physical interpretation of the different field mechanisms that occur as the frequency increases. A transformer accounts rigorously for the reactive energy associated to the transition from pin to patch, also when the length of the pin is not negligible in terms of the wavelength. A PPW transmission line represents the finiteness of the metallic patch. Finally an end point load associated to the MUT and the thickness of the metallization is evaluated resorting to an in-house tool based on a MoM procedure. The tool provides an accurate impedance, current distributions and voltages over the entire structure with accuracies equivalent to full wave 3D tool, with much lower computational cost, but much higher physical insight. A simulation with propanol as the MUT takes about 2minutes and 46 seconds for three frequency points in a commercial software such as Ansoft HFSS whereas the analytical tool takes 39.56 seconds with the same resources.

Chapter 8

Conclusions and Future Prospects

The research work reported in this dissertation was carried out at Delft University of Technology, Delft, Netherlands. The scope of this thesis was the development of a new class of sensors, enabling fast and accurate dielectric characterization of samples, with high-sensitivity and high-spatial resolution by employing advanced CMOS technology for various applications in the bio-medical and food industry.
Near-field dielectric spectroscopy, as targeted by the proposed solution, with high spatial lateral resolution can provide an in-depth knowledge on the dielectric and subsequently on the composition of the superficial and sub-interface layers of a sample. This data can provide key information in making decisions for various applications ranging from bio-medical to quality assessment of food produce.
In this dissertation, a methodology to evaluate the complex permittivity of an unknown multilayer sample by measuring the reflection co-efficient using a coaxial/ coaxial based sensors is presented. This consists in generating calibration surfaces that maps the measured complex admittance to a complex permittivity by minimizing a cost function, which in this case in the difference in the measured and evaluated admittance using the tool developed. The main aspects pertaining to the theoretical development and the practical implementation of permittivity sensors are investigated. The most significant results achieved in this thesis work are summarized in the subsequent sections.

8.1 Analysis of open-ended coaxial sensors

In Ch. 2 the input admittance of a coaxial aperture is derived to study the effect of the variation in the MUT's dielectric properties on the coaxial's input admittance. To this goal, a magnetic field integral equation (MFIE) is imposed on the aperture to ensure the

continuity of the tangential components of the magnetic fields in the two regions, below and above the aperture.
In the presence of a multilayered media, a methodology is outlined to accelerate the evaluation of the reaction integral by extracting the high spectral components in the integral associated to the quasi-static capacitance. Subsequently the input admittance is expressed as the superposition of a regularized admittance and a quasi-static capacitance. The quasi-static capacitance is associated to the permittivity of the first layer the aperture is exposed to. Whereas the regularized admittance depends on the thicknesses and dielectric constants of the layers following the first layer. The relative amplitude of the regularized admittance with respect to the total admittance determines the dependence of the total admittance of a coaxial of a given dimension to the layer under test.

8.1.1 Characterization of Layered Media using Coaxial sensor

In Ch. 3 the analytical model developed in Ch. 2 is used to extract the complex permittivity of the pulp of a biological sample (mango in this case) by modelling the sample as a two layered medium. The electrical properties of the first layer (skin in this case) is assumed to be consistent through out the measurement. The extracted pulp epsilon is validated with direct measurements. The tool is then subsequently used to enhance the sensitivity in staging the ripening process over a duration of time and to identify internal defects (non-visible) in mangoes.

8.1.2 Detection depth analysis

In Ch. 4 the sensitivity analysis of the coaxial/ coaxial based sensors to the alterations in the MUT's dielectric properties is addressed. The analysis is performed by assuming the read-out circuitry to be an impedance wheat-stone bridge. Building on the insight acquired from the sensitivity analysis performed using the analytical tool in Ch. 2, guidelines for increasing the detection depth of the sensor are derived: the detection depth of the sensor can be enhanced by realizing a sensor equivalent to a larger coaxial cable. This can be achieved by extending the central conductor of the coaxial aperture as a pin and terminating it with a patch in planar technology. This is further validated with sensitivity measurements performed using two pin-patch prototypes of different radii fabricated in printed circuit board technology and a custom made open-ended coaxial probe.

8.2 Analysis of Single-Ended Sensing Element

In Ch. 5, the integral equation imposed on the coaxial aperture etched on a ground plane in Ch. 2 is further extended by including the contribution of the pin-patch structure terminating the aperture. The additional contribution is evaluated by setting up an electric field integral equation on the pin-patch structure and estimating the magnitude of the electric current resorting to method of moments. Furthermore the analytical tool is used in generating calibration surfaces that maps the complex permittivity of the material under test to an admittance at the coaxial aperture. The calibration surfaces are further used to evaluate the complex permittivity of the unknown material from Γ measurements. The tool is validated with measurements performed using three sensing elements fabricated in PCB technology of different radii.

8.2.1 Method of Moments

In Ch. 6, a detailed procedure to evaluate the reaction integrals including vertical/ longitudinal currents in the Method of Moments for stratified media is presented. The procedure resorts to evaluating analytically the Fourier Transforms of the basis and test functions, and then performing the reactions entirely in the spectral domain. For a specific example, of a coaxial loaded pin-patch structure, the basis functions were defined such that they ensure the continuity of the currents at the transitions . Such structures have been extensively studied in literature.

8.2.2 Equivalent Circuit Modelling

In Ch. 7, a fast and efficient equivalent radial transmission line tool is outlined to accurately evaluate the input impedance of a single-ended patch sensing element realized in planar technology. The procedure provides a physical interpretation of the different field mechanisms that occur as the frequency increases. A transformer accounts rigorously for the reactive energy associated to the transition from pin to patch, also when the length of the pin is not negligible in terms of the wavelength. A parallel plate waveguide transmission line represents the finiteness of the metallic patch. Finally an end point load associated to the material under test and the thickness of the patch metallization is evaluated resorting to an in-house tool based on a method of moments procedure derived in Ch. **??**. The tool provides an accurate impedance, current distributions and voltages over the entire structure with accuracies equivalent to full wave 3D tool, with much lower computational cost, but much higher physical insight. A simulation with propanol with frequency dependent

dielectric properties as the MUT takes about 2minutes and 46 seconds for three frequency points in a commercial software such as Ansoft HFSS whereas the analytical tool takes 39.56 seconds with the same resources.

8.3 Future Prospects

The work presented in this thesis has been concerned with the development of a CMOS based integrated instrument for the investigation of the spectral signatures of various materials with micro-metric resolutions. The frequency band between 0.5 GHz and 5 GHz have been addressed due to the choice of developing the sources and the detectors for these frequencies. In most cases, because of the choice of focusing in these low frequency regimes, the analysis steps could also have been performed with entirely quasi static tools. However, choosing a more advanced nodes (CMOS technology) than the ones utilized in this thesis, one can move towards higher frequencies that are of interest for fundamental scientific investigations.

The TeraHertz (THz) spectrum in fact contains the key information characterizing the dynamics of complex molecules and materials and near-field infrared spectroscopy is the tool of choice for material characterization [74]. Micro-metric [75] or even nano-metric resolutions [75–77], together with wide frequency spectra, could provide a plethora of information on the most complex and interesting phenomena. However, whenever the channels carrying the signals are lossy, as in the near-field setups, the poor signal to noise ratios available in current sensing systems does not allow for fast investigations in the few THz ranges. For these reason the optimization of the interface between the passive integrated circuitry and the active portions of the transmit and receive modules is the field in which lie the maximum potential benefits in exploiting the analytical techniques developed in this thesis. We expect that over the next few years the traditional distinction between the integrated circuits design and the radiation/sensing interface will become more and more obsolete.

In this respect we imagine that the future development of this work will be the systematic extension of planar spectral representation techniques developed mostly for the analysis of planar printed circuit boards to 3D circuits, that are not intrinsically planar, when looked from very close by, since the metallizations and the dielectric layers are of comparable thicknesses.

Appendix A

Electric Fields due to Azimuthal Magnetic Current in Stratified Medium

The Greens function in planar stratified media can be calculated using the solution of the equivalent transmission line of the stratification as described in [78]. In this appendix the electric field radiated by an azimuthal magnetic current, that defines the current profile on a coaxial aperture in specific, in the presence of stratified media along $\hat{z}$ and $\hat{\rho}$ is reported using the spectral greens functions formalized in [78].

A.1 Electric Field along $\hat{z}$

From [50] we know the spatial greens function that gives the azimuthal magnetic field radiated by an azimuthal magnetic current to be

$$g^{hm}_{\phi\phi'}(\rho,\phi,z;\rho',\phi',z') = \frac{1}{2\pi}\sum_{m=-\infty}^{\infty} e^{-jm(\phi-\phi')}\int_0^{\infty}\frac{1}{k_\rho}G^{hm}_{\phi\phi}(k_\rho,m;z,z')dk_\rho \tag{A.1}$$

where m is the modes in ϕ. The spectral greens function, $G^{hm}_{\phi\phi}(k_\rho,m;z,z')$ is a sum of two contributions associated to the Transverse Electric (TE) and Transverse Magnetic (TM) transmission lines,

$$G^{hm}_{\phi\phi}(k_\rho,m;z,z') = G^{hm}_{\phi\phi,TM}(k_\rho,m;z,z') + G^{hm}_{\phi\phi,TE}(k_\rho,m;z,z') \tag{A.2}$$

where

$$G^{hm}_{\phi\phi,TM}(k_\rho, m; z, z') = I^{m_\phi}_{TM}(k_\rho; z, z')\left\{\frac{\partial}{\partial\rho'}J_m(k_\rho\rho')\frac{\partial}{\partial\rho}J_m(k_\rho\rho)\right\} \tag{A.3}$$

and

$$G^{hm}_{\phi\phi,TE}(k_\rho, m; z, z') = m^2 I^{m_\phi}_{TE}(k_\rho; z, z')\left\{\frac{J_m(k_\rho\rho')}{\rho'}\frac{J_m(k_\rho\rho)}{\rho}\right\}. \tag{A.4}$$

$I^{m_\phi}_{TM}(k_\rho; z, z')$ and $I^{m_\phi}_{TE}(k_\rho; z, z')$ are the TE and TM spectral currents flowing at z in the equivalent transmission lines with the voltages source in series at z'. $J_m(k_\rho\rho)$ and $J_m(k_\rho\rho')$ are the bessel functions of order m. The basis function $m_\phi(\boldsymbol{r})$ that defines the magnetic current profile on the coaxial aperture is azimuth symmetric, hence $m = 0$, thereby condensing the greens function to

$$g^{hm}_{\phi\phi'}(\rho, z; \rho', z') = \frac{1}{2\pi}\int_0^\infty \frac{1}{k_\rho} I^{m_\phi}_{TM}(k_\rho; z, z')\left\{\frac{\partial}{\partial\rho'}J_0(k_\rho\rho')\frac{\partial}{\partial\rho}J_0(k_\rho\rho)\right\}dk_\rho. \tag{A.5}$$

The azimuthal magnetic field radiated by $m_\phi(\boldsymbol{r})$ is expressed using the following reaction

$$h_\phi(\boldsymbol{r}) = \int_0^{2\pi}\int_a^b g^{hm}_{\phi\phi}(\boldsymbol{r}; \boldsymbol{r}')m_\phi(\boldsymbol{r}')\rho' d\rho' d\phi'. \tag{A.6}$$

Subsequently substituting the greens function $g^{hm}_{\phi\phi}(\boldsymbol{r}; \boldsymbol{r}')$, basis function $m_\phi(\boldsymbol{r}')$ and evaluating the integrals in ρ', ϕ' analytically results in the field being expressed as a single integral in k_ρ as

$$h_\phi(\boldsymbol{r}) = -\frac{1}{\ln\frac{b}{a}}\int_0^\infty I^{m_\phi}_{TM}(k_\rho; z, z')\Big(J_0(k_\rho b) - J_0(k_\rho a)\Big)J_1(k_\rho\rho)dk_\rho \tag{A.7}$$

The electric field can further be evaluated from Eq. A.7 using duality theorem as shown in [79]

$$\boldsymbol{E} = \frac{1}{j\omega\epsilon}\Big(\nabla\times\boldsymbol{H}\Big) \tag{A.8}$$

where

$$\nabla\times\boldsymbol{H} = \nabla\times h_\phi(\boldsymbol{r}) = \frac{-\partial h_\phi(\boldsymbol{r})}{\partial z}\hat{\rho} + \frac{1}{\rho}\frac{\partial\big\{\rho h_\phi(\boldsymbol{r})\big\}}{\partial\rho}\hat{z}. \tag{A.9}$$

Substituting Eq. A.9 in Eq. A.8 and performing few mathematical steps the electric field oriented along $\hat{z}$ at $\rho = 0$ is expressed as

$$e_z(z) = -\frac{1}{j\omega\epsilon\ln\frac{b}{a}}\int_0^\infty I^{m_\phi}_{TM}(k_\rho; z, 0)\Big(J_0(k_\rho b) - J_0(k_\rho a)\Big)k_\rho dk_\rho. \tag{A.10}$$

A.2 Electric Field along $\hat{\rho}$

Similarly the spatial greens function that gives the radial electric field radiated from an azimuthal magnetic current from [50] is formalized as

$$g^{em}_{\rho\phi'}(\rho,\phi,z;\rho',\phi',z') = \frac{1}{2\pi}\sum_{m=-\infty}^{\infty} e^{-jm(\phi-\phi')}\int_0^{\infty}\frac{1}{k_\rho}G^{em}_{\rho\phi}(k_\rho,m;z,z')dk_\rho. \tag{A.11}$$

The spectral greens function, $G^{em}_{\rho\phi}(k_\rho,m;z,z')$ is a sum of two contributions associated to the TE and TM transmission lines. However as mentioned in the previous section the magnetic current in azimuth symmetric hence $m=0$ and only TM component persists

$$G^{em}_{\rho\phi}(k_\rho,m;z,z') = V^{m_\phi}_{TM}(k_\rho;z,z')\left\{\frac{\partial}{\partial\rho'}J_0(k_\rho\rho')\frac{\partial}{\partial\rho}J_0(k_\rho\rho)\right\}. \tag{A.12}$$

Substituting Eq. A.12 in Eq. A.11, the spatial electric greens function that gives the $\hat{\rho}$ component of the field can be expressed as

$$g^{em}_{\rho\phi'}(\rho,\phi,z;\rho',\phi',z') = \frac{1}{2\pi}\int_0^{\infty}\frac{1}{k_\rho}V^{m_\phi}_{TM}(k_\rho;z,z')\left\{\frac{\partial}{\partial\rho'}J_0(k_\rho\rho')\frac{\partial}{\partial\rho}J_0(k_\rho\rho)\right\}dk_\rho. \tag{A.13}$$

The electric field along $\hat{\rho}$ due to $m_\phi(\boldsymbol{r}')$ is evaluated as the reaction between the greens function, $g^{em}_{\rho\phi'}(\boldsymbol{r};\boldsymbol{r}')$ and $m_\phi(\boldsymbol{r}')$ as

$$e_\rho(\boldsymbol{r}) = \int_0^{2\pi}\int_a^b g^{em}_{\rho\phi}(\boldsymbol{r};\boldsymbol{r}')m_\phi(\boldsymbol{r}')\rho'd\rho'd\phi'. \tag{A.14}$$

Substituting Eq. A.13 and $m_\phi(\boldsymbol{r}')$ in Eq. A.14 and evaluating the integral in ρ' analytically, the electric field can be expressed as a single integral in k_ρ

$$e_\rho(\rho,z) = -\frac{1}{\ln\frac{b}{a}}\int_0^{\infty}V^{m_\phi}_{TM}(k_\rho;z,0)J_1(k_\rho\rho)\left\{J_0(k_\rho b)-J_0(k_\rho a)\right\}dk_\rho. \tag{A.15}$$

Appendix B

Reaction Integrals

The objective of this appendix is to evaluate the reaction integral between overlapping basis and test functions for the problems containing vertical currents in homogeneous media in the spectral domain.

B.1 Green's function

The spatial Green's function, $g_{zz}^{ej}(\boldsymbol{r},\boldsymbol{r'})$ in an homogeneous space can be expressed as the inverse fourier transform of the spectral Green's function as follows

$$g_{zz}^{ej}(\boldsymbol{r},\boldsymbol{r'}) = j\frac{\zeta}{k}\frac{1}{8\pi^3} \iiint_{-\infty}^{\infty} \frac{k^2-k_z^2}{k^2-k_x^2-k_y^2-k_z^2} e^{-jk_x(x-x')} e^{-jk_y(y-y')} e^{-jk_z(z-z')} dk_x dk_y dk_z \tag{B.1}$$

where ζ and k are the wave impedance and wave number in the homogeneous space. Introducing the polar coordinates (ρ,ϕ) and (k_ρ,α) via the transformation $x=\rho\cos\phi$, $y=\rho\sin\phi$, $k_x=k_\rho\cos\alpha$ and $k_y=k_\rho\sin\alpha$, the greens function in Eq. B.1 can be rewritten as

$$g_{zz}^{ej}(\boldsymbol{r},\boldsymbol{r'}) = j\frac{\zeta}{k}\frac{1}{8\pi^3} \int_{-\infty}^{\infty}\int_{0}^{\infty}\int_{0}^{2\pi} \frac{k^2-k_z^2}{k^2-k_\rho^2-k_z^2} e^{-jk_\rho\rho\cos(\alpha-\phi)} e^{-jk'_\rho\rho'\cos(\alpha-\phi')} e^{-jk_z(z-z')} d\alpha k_\rho dk_\rho dk_z. \tag{B.2}$$

The reaction integral using the definition of Galerkin's projection can be expressed as

$$Z_{zz} = \iint_{S_t} J_z(\boldsymbol{r}) \iint_{S_b} J_z(\boldsymbol{r'}) g_{zz}^{ej}(\boldsymbol{r},\boldsymbol{r'}) d\boldsymbol{r} d\boldsymbol{r'} \tag{B.3}$$

where

$$J_z(\boldsymbol{r}) = \frac{1}{2\pi a}\delta(\rho - a)i(z)\hat{z} \tag{B.4}$$

and $i(z)$ is the current distribution, a the radius of the pin and S_b, S_t the surface of the test and basis functions. Substituting Eq. B.4 in Eq. B.3 and evaluating the integrals in ρ and ρ', Eq. B.3 can be further written as

$$\begin{aligned} Z_{zz} =& \frac{1}{(2\pi)^2}\int_z\int_0^{2\pi} i_z(z)\int_{z'}\int_0^{2\pi} i_z(z') \\ & j\frac{\zeta}{k}\frac{1}{8\pi^3}\int_{-\infty}^{\infty}\int_0^{\infty}\int_0^{2\pi}\frac{k^2-k_z^2}{k^2-k_\rho^2-k_z^2}e^{-jk_\rho\rho\cos(\alpha-\phi)}e^{-jk'_\rho\rho'\cos(\alpha-\phi')}e^{-jk_z(z-z')} \\ & d\alpha k_\rho dk_\rho dk_z d\phi' dz' d\phi dz. \end{aligned} \tag{B.5}$$

The above expression can be further simplified by using the following identities

$$\int_0^{2\pi} e^{-jk_\rho\rho'\cos(\alpha-\phi')}d\phi' = 2\pi J_0(k_\rho\rho') \tag{B.6}$$

$$\int_0^{2\pi} e^{jk_\rho\rho\cos(\alpha-\phi)}d\phi = 2\pi J_0(k_\rho\rho) \tag{B.7}$$

$$\int_0^{2\pi} d\alpha = 2\pi \tag{B.8}$$

Subsequently Z_{zz} reduces to a four fold integral, two in spectral domain and two in spatial domain

$$\begin{aligned} Z_{zz} =& \frac{1}{(2\pi)^2}j\frac{\zeta}{k}\int_z\int_{z'} i(z)i(z') \\ & \left\{\int_{-\infty}^{\infty}\int_0^{\infty}\frac{k^2-k_z^2}{k^2-k_\rho^2-k_z^2}J_0(k_\rho a)J_0(k_\rho a)e^{-jk_z(z-z')}k_\rho dk_\rho dk_z\right\}dzdz'. \end{aligned} \tag{B.9}$$

Furthermore

$$Z_{zz} = \frac{1}{(2\pi)^2}j\frac{\zeta}{k}\int_{-\infty}^{\infty}\int_0^{\infty}\frac{k^2-k_z^2}{k^2-k_\rho^2-k_z^2}J_0(k_\rho a)J_0(k_\rho a)I_b(k_z)I_t(-k_z)k_\rho dk_\rho dk_z \tag{B.10}$$

$I_b(k_z), I_t(-k_z)$ being the fourier transform of the basis and test functions. Extending the integration domain in k_ρ from $-\infty$ to ∞, Eq. B.10 can be expressed as

$$Z_{zz} = \frac{1}{8\pi^2}j\frac{\zeta}{k}\int_{-\infty}^{\infty}\int_{-\infty}^{\infty}\frac{k^2-k_z^2}{k^2-k_\rho^2-k_z^2}J_0(k_\rho a)H_0^{(2)}(k_\rho a)I_b(k_z)I_t(-k_z)k_\rho dk_\rho dk_z. \tag{B.11}$$

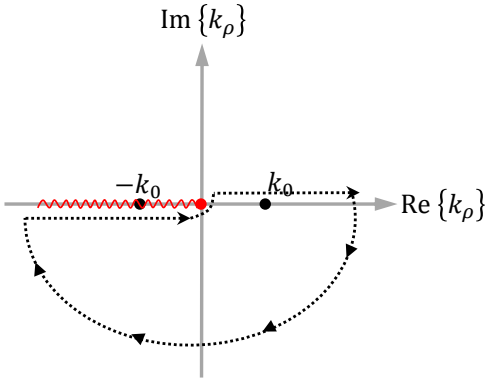

Figure B.1: Singularities and deformation path in the k_ρ plane. Red dot and line refers to the Hankel functions branch point and branch cut singularity whereas the black dotted line correspond to the deformation path.

The spectral integral in k_ρ contains branch point and branch cut singularity associated to the Hankel function and two poles at $\sqrt{k^2-k_z^2}$ and $-\sqrt{k^2-k_z^2}$. By using Cauchy theorem, the residue theorem can be applied. To ensure convergence, the path can be deformed at infinity as shown in Fig. B.1. The result of the integral can be obtained as the residue corresponding to that singularity. Eq. B.11 can be eventually evaluated using a single spectral integral as shown

$$Z_{zz} = \frac{\zeta}{8\pi k}\int_{-\infty}^{\infty} J_0\Big(\sqrt{k^2-k_z^2}a\Big)H_0^{(2)}\Big(\sqrt{k^2-k_z^2}a\Big)(k^2-k_z^2)I_b(k_z)I_t(-k_z)dk_z. \quad \text{(B.12)}$$

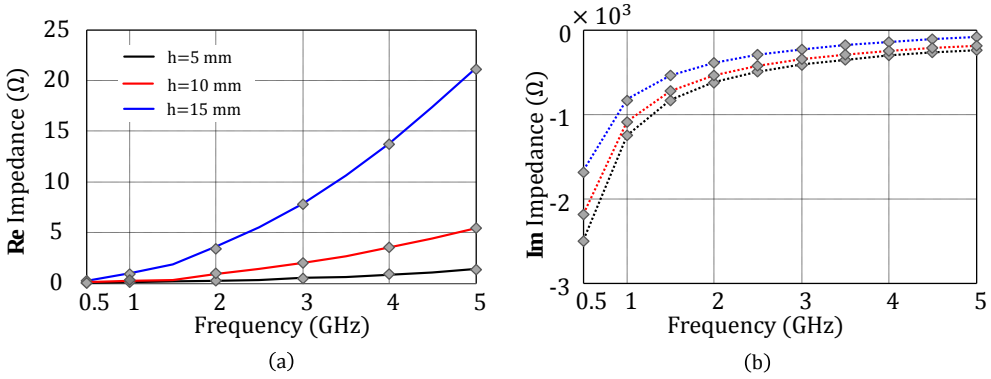

Figure B.2: Impedance evaluated for a piecewise sinusoidal of different lengths h using Eq. B.11 (bold lines in (a) and dotted lines in (b))and validated with impedance obtained using Eq. B.12 (filled grey diamonds).

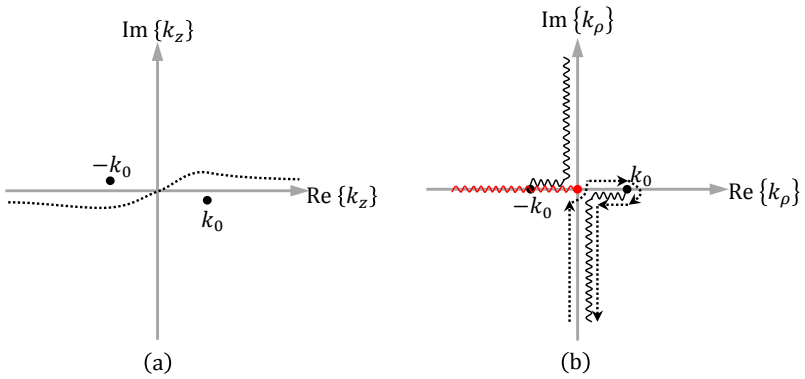

Figure B.3: Equivalent deformation paths (a) k_z plane and (b) k_ρ plane.

Fig. B.2 shows the comparison between the impedance evaluated using the double spectral integrals in Eq. B.11 to that of the single spectral integral in k_z in Eq. B.12 for a piecewise linear (PWL) basis function of length h.

The integration in Eq. B.12 is performed along the real axis where k_z is real and varies from $-\infty$ to $+\infty$. Introducing change of variable $k_z = \sqrt{k^2 - k_\rho^2}$ and performing the integration along the branch as shown in Fig. B.3(b), is equivalent to performing integration as in Fig. B.3(a). Choosing the square root to be $k_z = -j\sqrt{-(k^2 - k_\rho^2)}$(top Reimann sheet), and deforming along the vertical axis, $k_\rho \rightarrow -jk_{\rho large}$ results in $k_z \approx k_{\rho large}$. This renders the fourier transforms of the basis and test functions to be oscillatory and convergence is brought about by the hankel function which decays exponentially. This transformation enables the reaction integral to be evaluated as a single integral in k_ρ as follow:

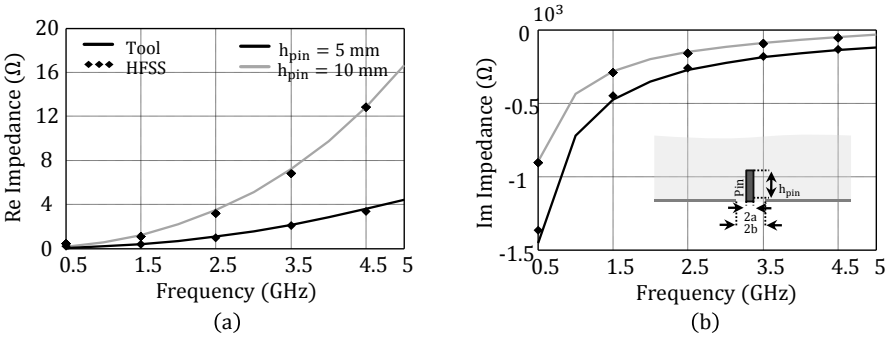

Figure B.4: Input impedance of a vertical pin in a homogeneous freespace excited by a magnetic frill generator. (a) and (b) Represents the real and the imaginary part of the input impedance for two different heights of the pin, h_{pin}(bold lines from in-house too while the filled diamonds are from Ansoft HFSS).

$$Z_{zz} = \frac{\zeta}{8\pi k} \int_{-\infty}^{\infty} \frac{J_0(k_\rho a) H_0^{(2)}(k_\rho a)}{\sqrt{k^2 - k_\rho^2}} I_b(\sqrt{k^2 - k_\rho^2}) I_t(-\sqrt{k^2 - k_\rho^2}) k_\rho^3 dk_\rho. \tag{B.13}$$

To highlight the validation of the proposed procedure, input impedance of a vertical cylindrical pin of height h_{pin} and radius a (as shown in Fig. B.4 inset) evaluated using Eq. 5.2 (in the absence of the patch) in freespace (bold lines) is shown in Fig. B.4(a) and (b) along with the simulation results (filled diamonds).

Bibliography

[1] JP Grant, RN Clarke, GT Symm, and Nicholas M Spyrou, "A critical study of the open-ended coaxial line sensor technique for rf and microwave complex permittivity measurements," *Journal of Physics E: Scientific Instruments*, vol. 22, no. 9, pp. 757, 1989.

[2] Cynthia Furse, Douglas A Christensen, and Carl H Durney, *Basic introduction to bioelectromagnetics*, CRC press, 2009.

[3] RT Tregear, "Interpretation of skin impedance measurements," *Nature*, vol. 205, no. 4971, pp. 600, 1965.

[4] Camelia Gabriel, Sami Gabriel, and y E Corthout, "The dielectric properties of biological tissues: I. literature survey," *Physics in medicine & biology*, vol. 41, no. 11, pp. 2231, 1996.

[5] Elise C Fear, Susan C Hagness, Paul M Meaney, Michal Okoniewski, and Maria A Stuchly, "Enhancing breast tumor detection with near-field imaging," *IEEE Microwave magazine*, vol. 3, no. 1, pp. 48–56, 2002.

[6] Ha-Young Jang, Hye-Ryun Kim, Mi-Sun Kang, Myoung-Hee Kim, and Bing Zhang, "The demand for quantitative techniques in biomedical image informatics," *Biomedical Engineering Letters*, vol. 4, pp. 319–327, 2014.

[7] R. Chandra, H. Zhou, I. Balasingham, and R. M. Narayanan, "On the opportunities and challenges in microwave medical sensing and imaging," *IEEE Transactions on Biomedical Engineering*, vol. 62, no. 7, pp. 1667–1682, July 2015.

[8] John A Zitelli, Christine Brown, and Barbara H Hanusa, "Mohs micrographic surgery for the treatment of primary cutaneous melanoma," *Journal of the American Academy of Dermatology*, vol. 37, no. 2, pp. 236–245, 1997.

[9] Sho Takamori, Kenny Kong, Sandeep Varma, Iain Leach, Hywel C Williams, and Ioan Notingher, "Optimization of multimodal spectral imaging for assessment of resection margins during mohs micrographic surgery for basal cell carcinoma," *Biomedical optics express*, vol. 6, no. 1, pp. 98–111, 2015.

[10] A Bennàssar, A Vilata, S Puig, and J Malvehy, "Ex vivo fluorescence confocal microscopy for fast evaluation of tumour margins during mohs surgery," *British Journal of Dermatology*, vol. 170, no. 2, pp. 360–365, 2014.

[11] Bo Stenquist, Marica B Ericson, C Strandeberg, Lena Mölne, Arne Rosén, Olle Larkö, and Ann-Marie Wennberg, "Bispectral fluorescence imaging of aggressive basal cell carcinoma combined with histopathological mapping: a preliminary study indicating a possible adjunct to mohs micrographic surgery," *British Journal of Dermatology*, vol. 154, no. 2, pp. 305–309, 2006.

[12] JK Karen, DS Gareau, SW Dusza, M Tudisco, M Rajadhyaksha, and KS Nehal, "Detection of basal cell carcinomas in mohs excisions with fluorescence confocal mosaicing microscopy," *British Journal of Dermatology*, vol. 160, no. 6, pp. 1242–1250, 2009.

[13] Marica B Ericson, Charlotta Berndtsson, Bo Stenquist, Lena Molne, Olle Larko, Ann-Marie Wennberg, and Arne Rosen, "Fluorescence demarcation of basal cell carcinoma controlled by histopathological mapping," in *Medical Imaging 2004: Image Processing*. International Society for Optics and Photonics, 2004, vol. 5370, pp. 1411–1418.

[14] Su-Young Jeon, Ki-Ho Kim, and Ki-Hoon Song, "Efficacy of fluorescence diagnosis-guided mohs micrographic surgery for pigmented vs non-pigmented basal cell carcinoma," *Acta dermato-venereologica*, vol. 94, no. 5, pp. 568–573, 2014.

[15] Caterina Longo, Moira Ragazzi, Milind Rajadhyaksha, Kishwer Nehal, Antoni Bennassar, Giovanni Pellacani, and Josep Malvehy Guilera, "In vivo and ex vivo confocal microscopy for dermatologic and mohs surgeons," *Dermatologic clinics*, vol. 34, no. 4, pp. 497–504, 2016.

[16] Zeina Tannous, Abel Torres, and Salvador González, "In vivo real-time confocal reflectance microscopy: a noninvasive guide for mohs micrographic surgery facilitated by aluminum chloride, an excellent contrast enhancer," *Dermatologic surgery*, vol. 29, no. 8, pp. 839–846, 2003.

[17] Milind Rajadhyaksha, Gregg Menaker, Thomas Flotte, Peter J Dwyer, and Salvador González, "Confocal examination of nonmelanoma cancers in thick skin excisions to

potentially guide mohs micrographic surgery without frozen histopathology," *Journal of investigative dermatology*, vol. 117, no. 5, pp. 1137–1143, 2001.

[18] Eileen S Flores, Miguel Cordova, Kivanc Kose, William Phillips, Anthony Rossi, Kishwer S Nehal, and Milind Rajadhyaksha, "Intraoperative imaging during mohs surgery with reflectance confocal microscopy: initial clinical experience," *Journal of biomedical optics*, vol. 20, no. 6, pp. 061103, 2015.

[19] John Strasswimmer, Mark C Pierce, Hyle Park, Victor Neel, and Johannes F de Boer, "Polarization-sensitive optical coherence tomography of invasive basal cell carcinoma," *Journal of biomedical optics*, vol. 9, no. 2, pp. 292–299, 2004.

[20] John R Durkin, Jeffery L Fine, Hakeem Sam, Melissa Pugliano-Mauro, and Jonhan Ho, "Imaging of mohs micrographic surgery sections using full-field optical coherence tomography: a pilot study," *Dermatologic surgery*, vol. 40, no. 3, pp. 266–274, 2014.

[21] D Cunha, T Richardson, N Sheth, G Orchard, A Coleman, and R Mallipeddi, "Comparison of ex vivo optical coherence tomography with conventional frozen-section histology for visualizing basal cell carcinoma during mohs micrographic surgery," *British Journal of Dermatology*, vol. 165, no. 3, pp. 576–580, 2011.

[22] Katie Xiaoyi Wang, Adam Meekings, Joachim W Fluhr, Gordon McKenzie, David A Lee, Juliya Fisher, Orit Markowitz, and Daniel M Siegel, "Optical coherence tomography–based optimization of mohs micrographic surgery of basal cell carcinoma: a pilot study," *Dermatologic Surgery*, vol. 39, no. 4, pp. 627–633, 2013.

[23] Elena de Castro, Diane M Barrett, Jennifer Jobling, and Elizabeth J Mitcham, "Biochemical factors associated with a co2-induced flesh browning disorder of pink lady apples," *Postharvest Biology and Technology*, vol. 48, no. 2, pp. 182–191, 2008.

[24] John Erwin, "Factors affecting flowering in ornamental plants," in *Flower Breeding and Genetics*, pp. 7–48. Springer, 2007.

[25] Peter Bonants and René te Witt, *Molecular Diagnostics in Plant Health*, pp. 175–202, Springer Singapore, Singapore, 2017.

[26] Hannah Jill James et al., "Understanding the flesh browning disorder of cripps pink apples," 2007.

[27] Inayat Bashir Pathan and C Mallikarjuna Setty, "Chemical penetration enhancers for transdermal drug delivery systems," *Tropical Journal of Pharmaceutical Research*, vol. 8, no. 2, 2009.

[28] MI Foreman, "Stratum corneum hydration; consequences for skin permeation experiments," *Drug Development and Industrial Pharmacy*, vol. 12, no. 3, pp. 461–463, 1986.

[29] A. M. Grishin and V. P. Denysenkov, "Broad band microwave probe for nondestructive test of dielectric coatings," in *Proceedings of the 13th IEEE International Symposium on Applications of Ferroelectrics, 2002. ISAF 2002.*, June 2002, pp. 91–93.

[30] DQM Craig, "Applications of low frequency dielectric spectroscopy to the pharmaceutical sciences," *Drug development and industrial pharmacy*, vol. 18, no. 11-12, pp. 1207–1223, 1992.

[31] Geoff Smith, Alistair P Duffy, Jie Shen, and Cedric J Olliff, "Dielectric relaxation spectroscopy and some applications in the pharmaceutical sciences," *Journal of pharmaceutical sciences*, vol. 84, no. 9, pp. 1029–1044, 1995.

[32] Ariel Lipson, Stephen G Lipson, and Henry Lipson, *Optical physics*, Cambridge University Press, 2010.

[33] C Gabriel, RH Bentall, and EH Grant, "Comparison of the dielectric properties of normal and wounded human skin material," *Bioelectromagnetics: Journal of the Bioelectromagnetics Society, The Society for Physical Regulation in Biology and Medicine, The European Bioelectromagnetics Association*, vol. 8, no. 1, pp. 23–27, 1987.

[34] Camelia Gabriel, Sami Gabriel, and y E Corthout, "The dielectric properties of biological tissues: I. literature survey," *Physics in medicine & biology*, vol. 41, no. 11, pp. 2231, 1996.

[35] Shakti K Davis, Henri Tandradinata, Susan C Hagness, and Barry D Van Veen, "Ultrawideband microwave breast cancer detection: a detection-theoretic approach using the generalized likelihood ratio test," *IEEE transactions on biomedical engineering*, vol. 52, no. 7, pp. 1237–1250, 2005.

[36] CP Vlahacos, RC Black, SM Anlage, A Amar, and FC Wellstood, "Near-field scanning microwave microscope with 100 μm resolution," *Applied physics letters*, vol. 69, no. 21, pp. 3272–3274, 1996.

[37] Massood Tabib-Azar, J Lawrence Katz, et al., "Evanescent microwaves: A novel super-resolution noncontact nondestructive imaging technique for biological applications," *IEEE Transactions on Instrumentation and Measurement*, vol. 48, no. 6, pp. 1111–1116, 1999.

[38] Y Ben-Aryeh, "Increase of optical resolution by evanescent waves," *Physics Letters A*, vol. 328, no. 4-5, pp. 306–312, 2004.

[39] M Tabib-Azar, S Bumrerraj, JL Katz, and SH You, "Evanescent electromagnetics: a novel, super-resolution, and non-intrusive, imaging technique for biological applications," *Biomedical Microdevices*, vol. 2, no. 1, pp. 73–80, 1999.

[40] T Whit Athey, Maria A Stuchly, and Stanislaw S Stuchly, "Measurement of radio frequency permittivity of biological tissues with an open-ended coaxial line: Part i," *IEEE Transactions on Microwave Theory and Techniques*, vol. 30, no. 1, pp. 82–86, 1982.

[41] Devendra Misra, Mohinder Chabbra, Benjamin R Epstein, M Microtznik, and Kenneth R Foster, "Noninvasive electrical characterization of materials at microwave frequencies using an open-ended coaxial line: Test of an improved calibration technique," *IEEE transactions on microwave theory and techniques*, vol. 38, no. 1, pp. 8–14, 1990.

[42] Maria A Stuchly, Michael M Brady, Stanislaw S Stuchly, and Gregory Gajda, "Equivalent circuit of an open-ended coaxial line in a lossy dielectric," *IEEE Transactions on instrumentation and Measurement*, vol. 1001, no. 2, pp. 116–119, 1982.

[43] Gangwu Chen, Kang Li, and Zhong Ji, "Bilayered dielectric measurement with an open-ended coaxial probe," *IEEE transactions on microwave theory and techniques*, vol. 42, no. 6, pp. 966–971, 1994.

[44] Devendra K Misra, "A quasi-static analysis of open-ended coaxial lines (short paper)," *IEEE Transactions on Microwave Theory and Techniques*, vol. 35, no. 10, pp. 925–928, 1987.

[45] Siqi Fan, Katie Staebell, and Devendrá Misra, "Static analysis of an open-ended coaxial line terminated by layered media," *IEEE transactions on instrumentation and measurement*, vol. 39, no. 2, pp. 435–437, 1990.

[46] Harold Levine and Charles H Papas, "Theory of the circular diffraction antenna," *Journal of applied physics*, vol. 22, no. 1, pp. 29–43, 1951.

[47] James Baker-Jarvis, Michael D Janezic, Paul D Domich, and Richard G Geyer, "Analysis of an open-ended coaxial probe with lift-off for nondestructive testing," *IEEE Transactions on Instrumentation and Measurement*, vol. 43, no. 5, pp. 711–718, 1994.

[48] Pascal De Langhe, Krist Blomme, Luc Martens, and Daniël De Zutter, "Measurement of low-permittivity materials based on a spectral-domain analysis for the open-ended coaxial probe," *IEEE transactions on instrumentation and measurement*, vol. 42, no. 5, pp. 879–886, 1993.

[49] Sasan Bakhtiari, Stoyan I Ganchev, and Reza Zoughi, "Analysis of radiation from an open-ended coaxial line into stratified dielectrics," *IEEE Transactions on Microwave Theory and Techniques*, vol. 42, no. 7, pp. 1261–1267, 1994.

[50] N. Llombart Juan, *Development of Integrated Printed Array Antennas Using EBG Substrates*, Ph.D. thesis, Polytechnic University of Valencia, 2006.

[51] Daniele Cavallo and Andrea Neto, "A connected array of slots supporting broadband leaky waves," *IEEE Transactions on Antennas and Propagation*, vol. 61, no. 4, pp. 1986–1994, 2013.

[52] Nathan Marcuvitz, *Waveguide handbook*, Number 21. Iet, 1951.

[53] S. A. Komarov, A. S. Komarov, D. G. Barber, M. J. L. Lemes, and S. Rysgaard, "Open-ended coaxial probe technique for dielectric spectroscopy of artificially grown sea ice," *IEEE Transactions on Geoscience and Remote Sensing*, vol. 54, no. 8, pp. 4941–4951, Aug 2016.

[54] M. Nakamura, T. Tajima, K. Ajito, and H. Koizumi, "Selectivity-enhanced glucose measurement in multicomponent aqueous solution by broadband dielectric spectroscopy," in *2016 IEEE MTT-S International Microwave Symposium (IMS)*, May 2016, pp. 1–3.

[55] Niwat Angkawisittpan and T Manasri, "Determination of sugar content in sugar solutions using interdigital capacitor sensor," *Measurement Science Review*, vol. 12, pp. 8–13, 03 2012.

[56] J. M. Anderson, C. L. Sibbald, and S. S. Stuchly, "Dielectric measurements using a rational function model," *IEEE Transactions on Microwave Theory and Techniques*, vol. 42, no. 2, pp. 199–204, Feb 1994.

[57] Andrew Gregory and R. Clarke, "Tables of the complex permittivity of dielectric reference liquids at frequencies up to 5 ghz," 01 2012.

[58] M. Spirito, *Enhanced Techniques for the Design and Characterization of RF Power Amplifiers*, Ph.D. thesis, Delft University of Technology, 2005.

[59] S. Pinhas, S. Shtrikman, and D. Treves, "Moment-method solution of the center-fed microstrip disk antenna invoking feed and edge current singularities," *IEEE Transactions on Antennas and Propagation*, vol. 37, no. 12, pp. 1516–1522, 1989.

[60] K. A. Michalski and J. R. Mosig, "Discrete complex image mpie analysis of coax-fed coupled vertical monopoles in grounded dielectric substrate: two formulations," *IEE Proceedings - Microwaves, Antennas and Propagation*, vol. 142, no. 3, pp. 269–274, June 1995.

[61] K. A. Michalski and D. Zheng, "Electromagnetic scattering and radiation by surfaces of arbitrary shape in layered media. i. theory," *IEEE Transactions on Antennas and Propagation*, vol. 38, no. 3, pp. 335–344, March 1990.

[62] K. A. Michalski and J. R. Mosig, "Multilayered media green's functions in integral equation formulations," *IEEE Transactions on Antennas and Propagation*, vol. 45, no. 3, pp. 508–519, March 1997.

[63] Cha-Mei Tang, "Electromagnetic fields due to dipole antennas embedded in stratified anisotropic media," *IEEE Transactions on Antennas and Propagation*, vol. 27, no. 5, pp. 665–670, Sep. 1979.

[64] Arnold Sommerfeld, *Partial differential equations in physics*, vol. 1, Academic press, 1949.

[65] Weng Cho Chew, *Waves and fields in inhomogeneous media*, IEEE press, 1995.

[66] A. Bhattacharyya, O. Fordham, and Yaozhong Liu, "Analysis of stripline-fed slot-coupled patch antennas with vias for parallel-plate mode suppression," *IEEE Transactions on Antennas and Propagation*, vol. 46, no. 4, pp. 538–545, April 1998.

[67] S. Maci, G. Avitabile, L. Borselli, G. Biifi-Gentili, and R. Tiberio, "Analysis of aperture-coupled patch antennas for cad applications," in *1993 Eighth International Conference on Antennas and Propagation*, March 1993, pp. 719–723 vol.2.

[68] G. A. E. Vandenbosch and A. R. Van De Capelle, "Reduction of coaxial feed between two parallel conductors into finite number of voltage sources," *Electronics Letters*, vol. 27, no. 25, pp. 2387–2389, Dec 1991.

[69] G. A. E. Vandenbosch, "Network model for capacitively fed microstrip element," *Electronics Letters*, vol. 35, no. 19, pp. 1597–1599, Sep. 1999.

[70] G. A. E. Vandenbosch and A. R. Van de Capelle, "Admittance of coaxial feed between two finite parallel conductors," *Electronics Letters*, vol. 28, no. 19, pp. 1780–1781, Sep. 1992.

[71] G. A. E. Vandenbosch, "Capacitive matching of microstrip antennas," *Electronics Letters*, vol. 31, no. 18, pp. 1535–1536, Aug 1995.

[72] Zhebin Hu, Gerasimos Vlachogiannakis, Michiel A. P. Pertijs, Leo C. N. de Vreede, and Marco Spirito, "A 5x5 microwave permittivity sensor matrix in 0.14-m cmos," *2018 IEEE/MTT-S International Microwave Symposium - IMS*, pp. 1160–1163, 2018.

[73] D.G. Dudley, IEEE Antennas, and Propagation Society, *Mathematical Foundations for Electromagnetic Theory*, IEEE Electromagnetic waves series. IEEE Press, 1994.

[74] D. N. Basov, Richard D. Averitt, Dirk van der Marel, Martin Dressel, and Kristjan Haule, "Electrodynamics of correlated electron materials," *Rev. Mod. Phys.*, vol. 83, pp. 471–541, Jun 2011.

[75] Mengkun Liu, Aaron J Sternbach, and D N Basov, "Nanoscale electrodynamics of strongly correlated quantum materials," *Reports on Progress in Physics*, vol. 80, no. 1, pp. 014501, nov 2016.

[76] Clemens Liewald, Stefan Mastel, Jeffrey Hesler, Andreas J. Huber, Rainer Hillenbrand, and Fritz Keilmann, "All-electronic terahertz nanoscopy," *Optica*, vol. 5, no. 2, pp. 159–163, Feb 2018.

[77] Matvey Finkel, Holger Thierschmann, Allard J Katan, Marc P Westig, Marco Spirito, and Teun M Klapwijk, "Shielded cantilever with on-chip interferometer circuit for thz scanning probe impedance microscopy," *Review of Scientific Instruments*, vol. 90, no. 11, pp. 113701, 2019.

[78] Leopold B Felsen and Nathan Marcuvitz, *Radiation and scattering of waves*, vol. 31, John Wiley & Sons, 1994.

[79] Constantine A Balanis, *Antenna theory: analysis and design*, John wiley & sons, 2016.

[80] Friederike Erdmann, Joannie Lortet-Tieulent, Joachim Schüz, Hajo Zeeb, Rüdiger Greinert, Eckhard W Breitbart, and Freddie Bray, "International trends in the incidence of malignant melanoma 1953–2008—are recent generations at higher or lower risk?," *International journal of cancer*, vol. 132, no. 2, pp. 385–400, 2013.

[81] A Lomas, J Leonardi-Bee, and F Bath-Hextall, "A systematic review of worldwide incidence of nonmelanoma skin cancer," *British Journal of Dermatology*, vol. 166, no. 5, pp. 1069–1080, 2012.

[82] Thomas W McGovern and David J Leffell, "Mohs surgery: the informed view," *Archives of dermatology*, vol. 135, no. 10, pp. 1255–1259, 1999.

List of Publications

Journal Papers

J1. H. T. Shivamurthy, Z. Hu, G. Vlachogiannakis, M. Spirito and A. Neto, "Equivalent Circuit Modelling of a Single-ended Patch Sensing element in Integrated Technology," *IEEE Transactions on Microwave Theory and Techniques*, vol. 68, no. 1, pp. 17-26, Jan 2020.

J2. H. T. Shivamurthy, M. Spirito and A. Neto, "Design and Analysis of Single-ended coax fed Permittivity Sensors in Planar Technology," *IEEE Transactions on Microwave Theory and Techniques*, accepted for publication.

J3. G. Vlachogiannakis, Z. Hu, H. T. Shivamurthy, A. Neto, M. A. P. Pertijis, L. C. N. de Vreede and M. Spirito, "Miniaturized Broadband Microwave Permittivity Sensing for Biomedical Applications," *IEEE Journal of Electromagnetics, RF and Microwaves in Medicine and Biology*, vol. 3, no. 1, pp. 48-55, March 2019.

Conference Papers

C1. H. T. Shivamurthy, I. Matacena and M. Spirito, "Dielectric Measurements of Mangoes from 0.5GHz to 20GHz using a custom open-ended coaxial probe," *47th European Microwave Conference*, Nuremberg, Germany, 2017.

C2. H. T. Shivamurthy, A. Neto and M. Spirito, "Permittivity Sensors in CMOS Technology," *12th European Conference on Antennas and Propagation*, London, UK, April 9-13, 2018.

C3. H. T. Shivamurthy and A. Neto, "Equivalent Circuit Model for Patch Loaded Coaxial Sensors in CMOS Technology," *12th European Conference on Antennas and Propagation*, London, UK, April 9-13, 2018.

C4. H. T. Shivamurthy, A. Neto and M. Spirito, "Sensitivity Analysis of Integrated Capacitive Sensors," *11th IEEE AP-S Symposium on Antennas and Propagation and USNC-URSI Radio Science Meeting*, Boston, Massachusetts, July 8-13, 2018.

C5. H. T. Shivamurthy, V. Mascolo, R. Romano, A. Neto and M. Spirito, "Complex Permittivity Extraction of Layered Biological Samples," *2018 IEEE/MTT-S International Microwave Symposium - IMS*, Philadelphia, PA, 2018, pp. 1573-1576.

C6. H. T. Shivamurthy, M. Spirito and A. Neto, "Rigorous Equivalent Circuit of a Patch Loaded Coaxial Permittivity Sensors," *13th European Conference on Antennas and Propagation*, Krakow, Poland, March 31-April 5, 2019.

C7. H. T. Shivamurthy and A. Neto, "A Method of Moments for Vertical Currents in Stratified Media with Reaction Integrals Directly in the Spectral Domain," *13th European Conference on Antennas and Propagation*, Krakow, Poland, March 31-April 5, 2019.

Co-authorship

C8. G. Vlachogiannakis,H. T. Shivamurthy, M. A. D. Pino and M. Spirito, "An I/Q-mixer-steering interferometric technique for high-sensitivity measurement of extreme impedances," *2015 IEEE MTT-S International Microwave Symposium*, Phoenix, AZ, 2015, pp. 1-4.

C9. M. Alonso-delPino,H. T. Shivamurthy, D. Cavallo, L. Galatro and M. Spirito, "BiCMOS integrated waveguide with artificial dielectric at submillimeter wave frequencies," *2016 IEEE MTT-S International Microwave Symposium (IMS)*, San Francisco, CA, 2016, pp. 1-4.

C10. Z. Hu, M. Alonso-delPino, D. Cavallo, H. T. Shivamurthy and M. Spirito, "Integrated waveguide power combiners with artificial dielectrics for mm-wave systems," *2017 IEEE MTT-S International Microwave Symposium (IMS)*, Honololu, HI, 2017, pp. 646-649.

C11. G. Vlachogiannakis, Z. Hu, H. T. Shivamurthy, A. Neto, M. A. P. Pertijis, L. C. N. de Vreede and M. Spirito, "A Compact Energy Efficient CMOS Permittivity Sensor Based on Multiharmonic Downconversion and Tunable Impedance Bridge," *2018 IEEE International Microwave Biomedical Conference (IMBioC)*, Philadelphia, PA, 2018, pp. 1-3.

Thesis Co-Supervised

T1. I. Matacena, "Ultra-Wideband dielectric spectroscopy for complex permittivity measurements using an open-ended coaxial probe at Microwave Frequencies," M.Sc. thesis, Delft University of Technology, Delft, Netherlands, 2014.

Summary

On the Design and Analysis of Micro-metric Resolution Arrays in Integrated Technology for Near-Field Dielectric Spectroscopy

Medical procedures and treatments have a great impact on the quality of life as well as on the health care costs. Increasing number of cases pertaining to skin cancer have been documented by the International Agency for Research on Cancer (IARC) [80, 81] every year. The most commonly used surgical technique for the skin cancer treatment is the Mohs surgery, whereby thin layers of skin containing cancer tissue are removed until only cancer free tissue remains. Reducing the number of iterations and in turn the surgery time during a Mohs surgery [82] would reduce patient's discomfort and medical costs. Having a fast, accurate and non-invasive diagnostic tool for the detection of anomalies would provide an additional assistance during the Moh's surgery to assess the depth of the tissue removal resulting in few iterations.

On the other hand, horticulture sector represent a very large market in several parts of the world. Enabling techniques to better assess the quality of the product during the entire supply chain process would result in high quality deliverables. Moreover, characterization of materials/objects with high accuracy is applicable to other scenarios that can be addressed by dielectric spectroscopy (e.g., surface quality inspection), which plays a role in many fabrication processes.

To address these needs, this work targets at developing models based on spectral method of moments to characterize multilayered samples for two near-field systems, first that of an open-ended coaxial probe and second, a matrix of near-field permittivity sensors in integrated technology.

To perform preliminary characterization experiments on biological samples in-house, a setup comprising of an open-ended coaxial probe has been developed. An analytical model to evaluate the input admittance of the coaxial probe was derived in Ch. 2 resorting to spectral greens functions. Dielectric measurements on various samples of mangoes have been performed to primarily characterize the dielectric response of the fruit, followed by

mapping the ripening process over a span of few days and also detecting internal defects as shown in Ch. 3.

To enhance the detection depth capabilities of the sensor while still resorting to planar technology, a coaxial fed pin-patch structure was studied using spectral Green's function in Ch. 5 and Ch. 6. The motivation to move towards such a structure was derived by performing detection depth analysis using a coaxial of radii 0.523 mm and two pin-patch structures of radii 1.5 mm and 2.5 mm, fabricated in printed circuit board technology, for increasing height of the airgap between the sensor plane and the silicon wafer in Ch. 4. Calibration surfaces, to map the measured input admittance to a complex permittivity, were generated using the tool in Ch. 5 for patches of radii 1.5 mm, 2.5 mm and 5 mm and they were validated by performing dielectric measurements on ethanol whose frequency dependent dielectric response is well established in literature using cole-cole parameters.

An equivalent circuit based on radial transmission line theory is derived for the single-ended patch sensing element to better represent the different physical mechanisms that occur in the sensor In Ch. 7. The reactive energy associated to the transition from pin to patch is presented by a transformer. A parallel plate waveguide formed between the patch and the ground plane is represented by a radial transmission line of length equal to radius of the metallic patch. Finally an end point load associated to the material under test and the thickness of the patch metallization is evaluated resorting to an in-house tool based on a method of moments procedure derived in Ch. 6. The tool provides an accurate impedance, current distributions and voltages over the entire structure with accuracies equivalent to full wave 3D tool, with much lower computational cost, but much higher physical insight.

Samenvatting

Over het ontwerp en de analyse van micrometrische resolutie stelsels in geïntegreerde technologie voor nabije-veld diëlektrische spectroscopie

Medische procedures en behandelingen hebben een grote invloed op de kwaliteit van leven en op de kosten van de gezondheidszorg. Een toenemend aantal gevallen van huidkanker wordt ieder jaar gedocumenteerd door het Internationaal Agentschap voor Kankeronderzoek (IARC) [30] [31]. De meest gebruikte chirurgische ingreep voor de behandeling van huidkanker is de Moh's operatie [32], waarbij dunne laagjes huid met kankercellen worden verwijderd totdat slechts kankervrije huid overblijft. Het verminderen van het aantal iteraties tijdens een Moh's operatie, en daarbij de operatietijd, vermindert het ongemak voor de patiënt en de medische kosten. Het hebben van een snel, nauwkeurig en niet-invasief diagnostisch hulpmiddel voor het detecteren van afwijkingen zou een extra hulp bieden tijdens de Moh's operatie om de diepte van de weefselverwijdering te bepalen, wat resulteert in minder iteraties. Daarnaast vertegenwoordigt de tuinbouw een zeer grote markt in verschillende delen van de wereld. Door technieken mogelijk te maken om de kwaliteit van het product gedurende het gehele productieproces beter te monitoren, zouden de uiteindelijke producten van hoge kwaliteit zijn. Bovendien is het karakteriseren van materialen / objecten met hoge nauwkeurigheid van toepassing op andere scenario's welke kunnen worden aangepakt door diëlektrische spectroscopie (bijv. inspectie van de oppervlaktekwaliteit), die een rol speelt in veel fabricageprocessen.

Om aan deze behoeften te voldoen, richt dit werk zich op het ontwikkelen van modellen op basis van de spectrale methode van momenten om meerlagige monsters te karakteriseren, voor twee nabije-veldsystemen, eerst die van een coaxiale sonde met open uiteinde en ten tweede een matrix van nabije-veld permittiviteitssensoren in geïntegreerde technologie.

Om interne karakterisatie-experimenten op biologische monsters in het lab uit te voeren, is een opstelling bestaande uit een coaxiale sonde met open uiteinden ontwikkeld. Een analytisch model om de ingangsadmittantie van de coaxiale sonde te berekenen, werd afgeleid in hfst. 2 gebruik makend van spectrale Green's-functies. Diëlektrische metingen aan ver-

schillende monsters van mango's zijn uitgevoerd om de diëlektrische respons van het fruit te karakteriseren, gevolgd door het in kaart brengen van het rijpingsproces over een periode van enkele dagen en ook interne defecten te detecteren zoals getoond in hfst. 3
. Om de detectiediepte van de sensor te verbeteren en toch gebruik te maken van planaire technologie, werd een coaxiaal gevoede pin-plaat-structuur bestudeerd met behulp van spectrale Green's functies in hfst. 5 en hfst. 6. De motivatie om naar een dergelijke structuur toe te gaan werd gebaseerd op een detectiediepte-analyse voor het vergroten van de hoogte van de luchtopening tussen het sensorvlak en de siliciumwafer met behulp van een coaxiale sonde van radius 0,523 mm en twee pin-plaat-structuren van radii 1,5 mm en 2,5 mm, vervaardigd in printplaattechnologie, in hfst. 4. Kalibratieoppervlakken, om de gemeten ingangsadmittantie te vertalen tot een complexe permittiviteit, werden gegenereerd met behulp van het model in hfst. 5 voor platen met radii 1,5 mm, 2,5 mm en 5 mm en werden gevalideerd door diëlektrische metingen uit te voeren op ethanol, waarvan de frequentie-afhankelijke diëlektrische respons goed is vastgelegd in de literatuur met behulp van cole-cole-parameters.
Een equivalent circuit op basis van radiale transmissielijntheorie is afgeleid voor het enkeleindige plaatdetectie-element om de verschillende fysieke mechanismen die in de sensor voorkomen te representeren in hfst. 7. De reactieve energie geassocieerd met de overgang van pin naar plaat wordt gerepresenteerd met een transformator. Een parallelle-plaatgolfgeleider gevormd tussen de plaat en het grondvlak wordt weergegeven door een radiale transmissielijn met lengte gelijk aan de straal van de metalen plaat. Tenslotte wordt een eindpuntbelasting, geassocieerd met het te testen materiaal en de dikte van de metallisatie van de plaat, berekend, gebruikmakend van een intern model op basis van een methode van momentenprocedure afgeleid in hfst. 6. Het model biedt ingangsimpedantie en stroom- en spanningverdelingen over de gehele structuur met een nauwkeurigheid equivalent aan comerciële software, maar met veel lagere rekenkosten en veel meer fysiek inzicht.

About the Author

Harshitha Thippur Shivamurthy was born on April 4, 1990 in Bangalore, India. She received her B.Sc. degree in Electronics and Communication Engineering from Nitte Meenakshi Institute of Technology (NMIT), Bangalore, India in June 2012. Subsequently, she received her M.Sc. degree in Electrical Engineering, Telecommunication Track from Delft University of Technology, Delft, The Netherlands in October 2014. Her M.Sc. internship was carried out at TomTom, Eindhoven from July to October 2013. The project dealt with GPRS Data Loss and End-to-End Testing. Her M.Sc thesis was carried out at Tera-Hertz Sensing Group from November 2013 to September 2014 . The thesis dealt with the analysis and design of Wideband, wide-Scan Planar Connected Slot Array Enhanced with Artificial Dielectrics, under the supervision of Prof. A. Neto.

In October 2014 she started working towards the Ph.D. degree in the Tera-Hertz Sensing group, Delft University of Technology, Delft, Netherlands. Here, she worked on the analysis and design of near-field dielectric spectroscopy in planar technology. This research has been carried out under the supervision of prof. dr. ir. A. Neto and co-supervised by dr. M. Spirito. This work resulted in one manufactured prototype demonstrator, 2 journal publications and 12 conference papers.

During her Ph.D, she has co-supervised one M.Sc. student, I. Matacena (TU-Delft).

Acknowledgements

This thesis work would not have been accomplished without the help, support and guidance of many people.

First and foremost, I would like to thank my promotor Prof. Andrea Neto for his guidance and supervision throughout my PhD. He is an inspiring mentor and an exceptional teacher. He was kind enough to spend a lot of his time, during the third and final year of my PhD, teaching me several electromagnetic concepts. His attitude and dedication towards work has taught me to always strive for the best. I specially want to thank Berenice and Andrea for their hospitality and looking out for me during tough times.

The second person who made this thesis work possible is my co-promotor dr. Marco Spirito. I would like to thank him for giving me the opportunity to work on this project. He has been a great mentor and an extremely patient supervisor.

I would like to thank my PhD defense committee members for taking out their valuable time and accepting to be a part of the PhD commission.

I would like to thank the rest of the THz Sensing Group: Cristina, Sven, Shahab, Alejandro, Marta, Ralph, Arturo, Huasheng, Bart, dr. Daniele, Prof. Nuria Llombart, dr. Juan Bueno, Prof. Jochem Baselmans and Everdine.

Cristina, thank you for being a great friend and a great support in the true sense of the word. The time spent every morning getting a coffee with you will be truly missed.

Sven, I cannot imagine TU Delft office without you in it. You were their when I entered and when I left every single day. Your positivity is very endearing.

Shahab and Alejandro, the conversations and laughter during my small visits to your office will be truly missed.

You guys made my stay at THz Sensing Group truly memorable. I wouldn't have it any other way.

I am grateful for my new colleagues at NXP, especially Waqas and Georgia who are very helpful and supportive.

Arun, Vishu, Adi, Abhi, Sumedh, Vikku, Pinky, Suma, Ketki, Vidya and Sneha, thank

you for all the happy times in Netherlands thus far. Arun, you are my big brother and our (phani and I) great support, we truly love you.
Mr. Phani Kiran Padmanabharao, my new found husband, you are my greatest strength. I have tears writing this, but I am saying it again "I love you with all my heart." Thank you for bringing Baba, Amma, Pawan and Pooja into my life. Their support and encouragement has been heartening.
Finally, I dedicate this thesis to my FAMILY: Amma, Appa and Hitu. You cannot imagine how much I miss you all here. You have put me before everything, supported me through all my decisions and stood by me in all my choices. I know I have been distant the past couple of years, I promise to be more present from now on. I love you guys.